PADERBORN UNIVERSITY

DOCTORAL THESIS

Dynamics of Natural and Artificial Biological Systems at Solid-Liquid Interfaces

Author:
Bhanu Kiran Pothineni

Supervisor:
PD Dr. Adrian Keller

A thesis submitted in fulfillment of the

requirements for the degree of Dr. rer. nat to the

Faculty of Science of Paderborn University

First Reviewer:	PD Dr. Adrian Keller
Second Reviewer:	Prof. Dr. Ilko Bald
Third Reviewer:	Prof. Dr. Guido Grundmeier

Acknowledgement

The journey of completing this PhD has been an incredible experience, one that would not have been possible without the guidance, support, and encouragement of many people to whom I am deeply grateful.

First and foremost, I would like to express my sincere gratitude to my advisor, **PD Dr. Adrian Keller**, for his invaluable guidance, constant encouragement, and unwavering support throughout this research. His insights and expertise have shaped my academic growth, while his kindness and patience have made this journey not just an intellectual pursuit but a truly enriching experience. More than just a mentor, he has been a friend, offering both professional advice and personal encouragement when I needed it most.

I extend my heartfelt thanks to **Prof. Dr. Guido Grundmeier** for providing me with the necessary lab space, resources, and a nurturing research environment that allowed me to carry out my work smoothly. His support has played a crucial role in facilitating my research, and I deeply appreciate the opportunities provided.

I express my sincere gratitude to **Prof. Dr. Ilko Bald** for kindly accepting the role of external reviewer for my PhD thesis and defense. It is truly an honor to have his valuable perspective and expertise during this crucial stage of my doctoral journey.

To my colleagues and friends, this PhD journey would not have been the same without your companionship, discussions, and unwavering support. The shared struggles, countless brainstorming sessions, and the moments of joy we celebrated together made this experience even more memorable. Thank you for standing by me through the highs and lows, for motivating me when things seemed tough, and for being an integral part of this journey.

Finally, I am profoundly grateful to my family for their unconditional love, patience, and sacrifices. Your belief in me, even when I doubted myself, has been the cornerstone of my perseverance. Words cannot express how much your encouragement and support have meant to me throughout these years. This achievement is as much yours as it is mine.

To all of you, thank you for being part of this journey. This thesis stands as a testament to the collective support and encouragement I have received, and I dedicate this milestone to each of you.

Table of Contents

Abstract

This thesis presents in-depth investigation into the dynamic interactions of biological entities at solid-liquid interfaces, integrating insights from DNA nanotechnology, microbiology and virology. Beginning with the self-assembly of hexagonal DNA origami lattices on mica substrates, proceeding to cation dependent assembly on SiO_2 surfaces, and extending to a comparative influence of various oxide deposition techniques and their influence in lattice formation has been studied and researched. In parallel, the work also explores bacterial adhesion and bacteriophage infection process and examines the impact of viral inactivation methods on surface interactions of viral particles.

The initial stage of the research focuses on the formation of DNA origami lattices on mica. High-speed Atomic Force Microscopy was utilized to monitor the real-time dynamics of lattice formation by varying the concentration of DNA origami. At lower concentration, incomplete monolayer was observed within the experimental time frame, whereas higher concentrations led to rapid formation of a complete monolayer within 2 minutes, followed by defect correction over the next 10 minutes.

Subsequently, the cation dependent assembly of hexagonal DNA origami lattices on SiO_2 was investigated. Divalent cations, specifically Mg^{2+} and Ca^{2+} were employed to modulate the electrostatic interactions critical for the adsorption, diffusion, and stable ordering of the DNA origami on the surface along with Na^+ as a monovalent ion at varying concentrations. Further comparative studies on various silicon oxide (SiOx) surfaces demonstrated that the oxide density and surface roughness significantly influence the DNA origami lattice formation on the surface.

In addition to DNA origami lattice studies, microbial interaction at solid-liquid interfaces was explored. Bacterial adhesion on gold surface and subsequent infection by a lytic *Escherichia coli* phage T7 was monitored using Quartz-Crystal Microbalance with Dissipation (QCM-D). The results indicated that change in dissipation (ΔD) provided a robust parameter for tracking the infection process rather than frequency (Δ*f*). Furthermore, another component of this thesis was to investigate the effect of the inactivation procedures using BPL and H_2O_2 on Zika virus (ZIKV) interaction with various model surfaces. Results reveal that H_2O_2 inactivation and active virus maintained similar adsorption values. In contrast, BPL inactivation significantly altered the viral surface interactions resulting in different adsorption values in comparison to H_2O_2 inactivated and active virus.

Overall, this interdisciplinary work bridges the fields of nanotechnology, and microbiology to provide a comprehensive understanding of biological interactions at solid-liquid interfaces.

List of Publications

Some sections of this thesis are based on the following published works:

1. **Pothineni, Bhanu Kiran**; Grundmeier, Guido; Keller, Adrian: Cation-dependent assembly of hexagonal DNA origami lattices on SiO_2 surfaces. *Nanoscale,* **2023,** *15* (31), 12894–12906. DOI: 10.1039/D3NR02926C.
2. **Pothineni, Bhanu Kiran**; Theile-Rasche, Chantal; Müller, Hendrik; Grundmeier, Guido; Los Arcos, Teresa de; Keller, Adrian: DNA Origami Adsorption and Lattice Formation on Different SiOx Surfaces. *Chemistry- A European Journal,* **2025,** *31*(12), e202404108. DOI: 10.1002/chem.202404108.
3. **Pothineni, Bhanu Kiran;** Probst, René; Kiefer, Dorothee; Dobretzberger, Verena; Barišić, Ivan; Grundmeier, Guido; Keller, Adrian: Monitoring phage infection and lysis of surface-immobilized bacteria by QCM-D. *Analytical and Bioanalytical Chemistry,* **2025.** DOI: 10.1007/s00216-025-05803-5.
4. **Pothineni, Bhanu Kiran;** Barner, Jörg; Contreras, David; Castra, Mario; Grundmeier, Guido; Keller, Adrian: Rapid assembly of highly ordered DNA origami lattices at mica surfaces. *Discover Nano*, **2025**. (Accepted).

Other Publications not included in this thesis

1. **Pothineni, Bhanu Kiran**; Keller, Adrian (2023): Nanoparticle-Based Formulations of Glycopeptide Antibiotics: A Means for Overcoming Vancomycin Resistance in Bacterial Pathogens? *Advanced NanoBiomed Research* **2023,** *3*(4), 2200134. DOI: 10.1002/anbr.202200134.
2. **Pothineni, Bhanu Kiran**; Kollmann, Sabrina; Li, Xinyang; Grundmeier, Guido; Erb, Denise J.; Keller, Adrian (2023): Adsorption of Ferritin at Nanofaceted Al_2O_3 Surfaces. *International Journal of Molecular Sciences* **2023,** *24* (16), 12808. DOI: 10.3390/ijms241612808.

List of Abbreviations

DNA:	Deoxyribonucleic acid
AFM:	Atomic force microscopy
HS-AFM:	High Speed- atomic force microscopy
QCM-D:	Quartz crystal microbalance with dissipation
XPS:	X-ray photon spectroscopy
SEM:	Scanning electron microscopy
SPR:	Surface plasmon resonance
ssDNA:	Single stranded DNA
kb:	Kilo bases
AuNPs:	Gold nanoparticles
2D and 3D:	2-Dimesional and 3-Dimensional
E. coli:	*Escherichia coli*
B. subtilis:	*Bacillus subtilis*
P. aeruginosa:	*Pseudomonas aeruginosa*
SAMs:	Self assembled monolayers
AC:	Alternating current
TAE:	Tetra acetate ethylenediaminetetraacetic acid
$MgCl_2$:	Magnesium chloride
$CaCl_2$:	Calcium chloride
NaCl:	Sodium chloride
SiO_2:	Silicon oxide
ML:	Monolayer
FFT:	Fast fourier transform
Fwhm:	Full-width at half maximum
MSD:	Magnetron sputter deposition
PE-CVD:	Plasma-enhanced chemical vapor deposition
ZIKV:	Zika virus
BPL:	Beta-propiolactone
H_2O_2:	Hydrogen peroxide
NH_4OH:	Ammonium hydroxide

List of Tables

List of Figures

Chapter 1: Fundamentals

1.1 Structural and Biochemical Insights into DNA

Deoxyribonucleic acid (DNA) is a fundamental biomolecule that carries all the genetic information for development, functioning and survival of all the organisms on earth. It is made up of two strands which coil around each other forming a helical structure. The strands are made of nucleotides (see Figure 2) which are made of nitrogenous bases called Adenine (A), Thymine (T), Cytosine (C), Guanine (G) and consist of deoxyribose sugars along with phosphate groups. In a single strand, the nucleotides are connected at their backbone through covalent bonds (phosphodiester bonds). As G pairs with C via three hydrogen bonds and T pairs with A via two hydrogen bonds (see Figure 3), the nucleotides in two complementary single strands can bind to each other.(*1*) Adenine and Guanine are classified as purines and cytosine and thymine as pyrimidines. DNA can form three helical conformations, which are B-, A- and Z-form (see Figure 1). B-form DNA is a right-handed helix that is typically found in genomes where it has 10.5 bp/turn with a space of 3.4 Å between the stacked bases and a backbone sugar phosphate bond rotation of 34.3° allowing base stacking with a total diameter of 20 Å. The A- and Z-forms exist less commonly in biological conditions and have different characteristic parameters.(*2*) The A-form is also a right-handed helix with 11 bp/turn with a space of 2.6 Å between the stacked bases with a diameter of 23 Å and predominantly forms only under severe dehydrating conditions, high salt, or in DNA-RNA hybrids.(*3*) The Z-form is a left-handed helix with 12 bp/turn with a space of 3.7 Å between the stacked bases with a diameter of 18 Å and predominantly forms only under GC-rich regions and under negative supercoiling conditions.(*4, 5*) Focusing on the B-form of DNA, the nucleic acid strands have an end to end chemical orientation (see Figure 3) i.e., the 5' end has a phosphate group and 3' end carbons have a free hydroxyl group. On the outside of B-form DNA, the spaces between the intertwined strands form two helical grooves of unequal widths described as the major groove and the minor groove.(*6*)

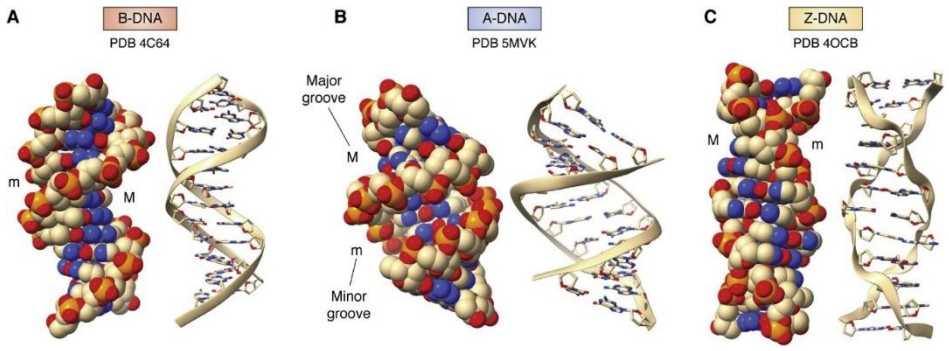

Figure 1: All DNA structures are space filling and cartoon representations. A, B and C. B, A and Z-DNA crystal structure with representative major and minor grooves. [Reprinted by Permission from: (7)]

The DNA generally as explained above takes up a helical structure and the reason for this is that the sugar phosphate backbone has a fixed spacing of 6 Å and each DNA base has a flat thickness of 3.3 Å, creating gaps of 2.7 Å between them and these gaps are energetically unfavorable as this would allow the entry of water molecules into the base stack. To resolve the gaps between the bases and to close the spaces between them a model of DNA was discussed called skewed ladder model to understand the helix model of DNA. Here, the sugar phosphate backbone was tilted or skewed at an angle of 30° (given the flexible properties of the rotatable bonds) from the horizontal where a constant distance of 6 Å is maintained between the sugars and where the bases are closely stacked (thermodynamically favorable because of the hydrophobic effect and van der Waals interaction between the stacked bases). But this model couldn't accommodate the three-dimensional constraints of DNA and further the atomic clashes between the different molecules. Furthermore, this model doesn't match the natural form of DNA found in nature. So, further a helical twist model was considered where the skewed geometry remained intact but wrapped around a cylindrical axis and this twist reduced the atomic clash between various atoms,(*8*) with the diameter of the double helix being around 20 Å.

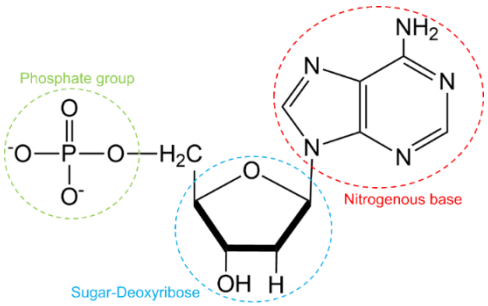

Figure 2: Chemical structure of Deoxyadenosine monophosphate with representation of individual components with adenosine as nitrogenous base (red), deoxyribose sugar (blue) and monophosphate (green).

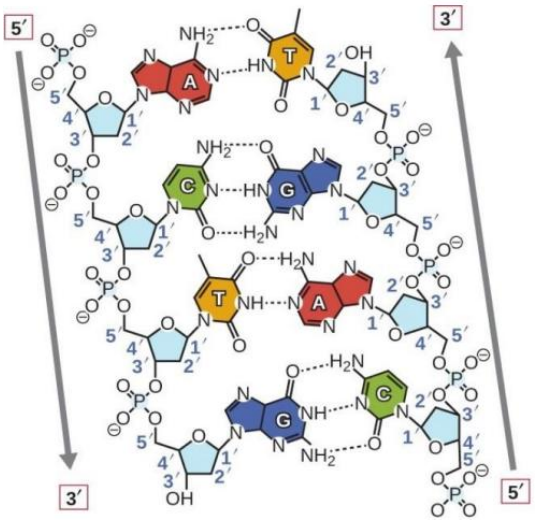

Figure 3: Chemical structure of DNA with A-T base pairing and G-C base pairing with representative 5' and 3' end of the antiparallel strands. [Reprinted by Permission from: (9)]

The phosphate groups in the DNA backbone have a pK_a of approximately 2. At physiological pH they are deprotonated and thus carry a negative charge. This negative charge of the phosphate group facilitates the interaction with positively charged ions (e.g., magnesium or sodium) or proteins within a solution leading to the stability of the double helix and serving in its formation. The major and minor grooves are formed based on the angle of glycosidic bonds at which the two sugars protrude out from the base pairs, which are about 120° for minor grooves and 240° for the major groove. The edge of an A-T base pair in the major groove has a hydrogen bond acceptor at N7 position of adenine (A), hydrogen bond donor at exocyclic amino group on C6 position of adenine (A), a hydrogen bond acceptor at carbonyl group on C4 of thymine and a hydrophobic group CH_3 on C5 of thymine. In the minor groove there is an acceptor, hydrogen and another acceptor. Further, in a similar pattern major grooves of G-C pair have an acceptor, acceptor, donor and a hydrogen group and the minor groove having an acceptor, donor and an acceptor. This signifies that the major groove has abundant chemical information in comparison to minor groove. This chemical information allows the various proteins to recognize DNA sequence without having to opening the double helix.(*10, 11*)

As discussed above, double helix is the most predominantly found structure in nature, but other than double helix there are other secondary structures found in nature, for example cruciform structures, triplex structure, G-tetraplex, and Holliday junctions.(*11*) Cruciform structures (see Figure 4a) are formed as a result of inverted repeats of a same sequence which are self-complementary to each other. When these repeated sequences are present in the same strand, they are called hairpin structures and when the repeated sequences are present in the opposite strands which are complementary to each other they are called cruciform structures. Other structures such as triplex structures and G-tetraplexes are formed when the nucleotides participating in the Watson-Crick base pairing can form additional hydrogen bonds with the chemical groups in the major groove of DNA double helix. When a cystine is protonated (at a lower pH) it can pair with a Guanidine in a G-C pair and in a similar way thymidine can pair with adenosine in a A-T pair, this type of unusual pairing is called Hoogsten pairing found by Karst Hoogsten in 1963.

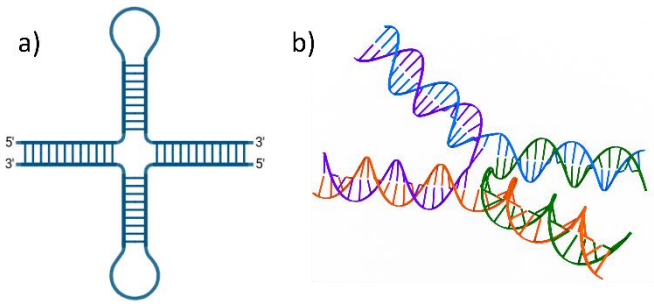

Figure 4: a) Schematic representation of a cruciform DNA secondary structure, b) Schematic representation of DNA Holliday junction.

Holliday junctions (see Figure 4b) are four-stranded, cross shaped structures (two intersecting double helices) that form during homologous recombination of DNA. Initially proposed by Robin Holliday in 1964, it serves as an intermediate that enables genetic diversity through DNA strand exchange during recombination events.(*12*) Furthermore, Holliday junctions serve as fundamental building blocks for creating complex, programmable artificial nanostructures. The stability and structural versatility of these four-way DNA junctions make them particularly valuable for engineered nanostructures. These junctions can adopt either rigid or flexible (wavy) configurations, depending on the DNA sequence selected. When Holliday junctions assume rigid conformations, they serve as stable structural motifs suitable for constructing larger, well-defined DNA nanostructures.

1.2 DNA Nanotechnology

1.2.1 Fundamentals of Structural DNA Nanotechnology

In 1982, Nadrian C. Seeman pioneered the discovery of design and assembly of DNA immobile Holliday junctions and their use in creating periodic two-dimensional DNA networks using the "sticky-end" ligation technique establishing the foundation for DNA Nanotechnology.(*13*) Later in the year 1983, Kallenbach et al., expanded this research to further explore immobile DNA junctions, initially envisioning their potential to organize proteins and other materials into precise lattice structures. Since then, the field of DNA nanotechnology developed enormously and led to the creation of variety of different DNA structures with various applications.(*14*)

The development of DNA origami (see Figure 5) was pioneered by Paul W.K. Rothemund in 2006, representing a paradigm-shifting discovery in the field of DNA nanotechnology.(*15*) The technique involves a long single stranded DNA scaffold, derived from M13mp18 bacteriophage, which is folded into complicated two-dimensional shapes using hundreds of complementary short DNA sequences called staple strands.(*15*) The scaffold is 7249 nucleotides long and only 7176 nucleotides are available for folding as the sequence consists of a hairpin structure which is 20 nucleotides long and staples binding to a hairpin region was unknown so a 73 nucleotides region was excluded for folding of origami. Furthermore, the folding process is a one pot reaction, employing a high molar excess of staple strands to scaffold (typically ranging from 5-100 fold molar excess, with ~10-fold being common practice).(*16, 15, 17*) The excess of staples guarantees that every scaffold segment rapidly encounters complementary staple sequences, leading to thermodynamic equilibrium towards fully folded DNA origami structures, furthermore also displacing unwanted secondary structures which can be caused by incorrect binding of staple sequences.(*15, 18*) These shapes are roughly 100 nm in diameter and have a spatial resolution (smallest precisely defined distance at which individual structural features can be positioned and distinguished within the DNA nanostructure) of 6 nm. The origami consists of

sequentially or adjacently arranged parallel double helices which are cut in one strand to be constrained by an integer number of turns in length. To hold these helices together and to avoid them falling apart the adjacent double helices are connected through periodic crossovers running from one helix to the another and so on in an antiparallel fashion. These periodic crossovers occur every 1.5 turns (16 bases) along the alternating side of the helix to minimize the interhelical gap to be 1 nm and 2.5 turns for a helical gap of 1.5 nm and so on for a single layer of origami.(*16*)

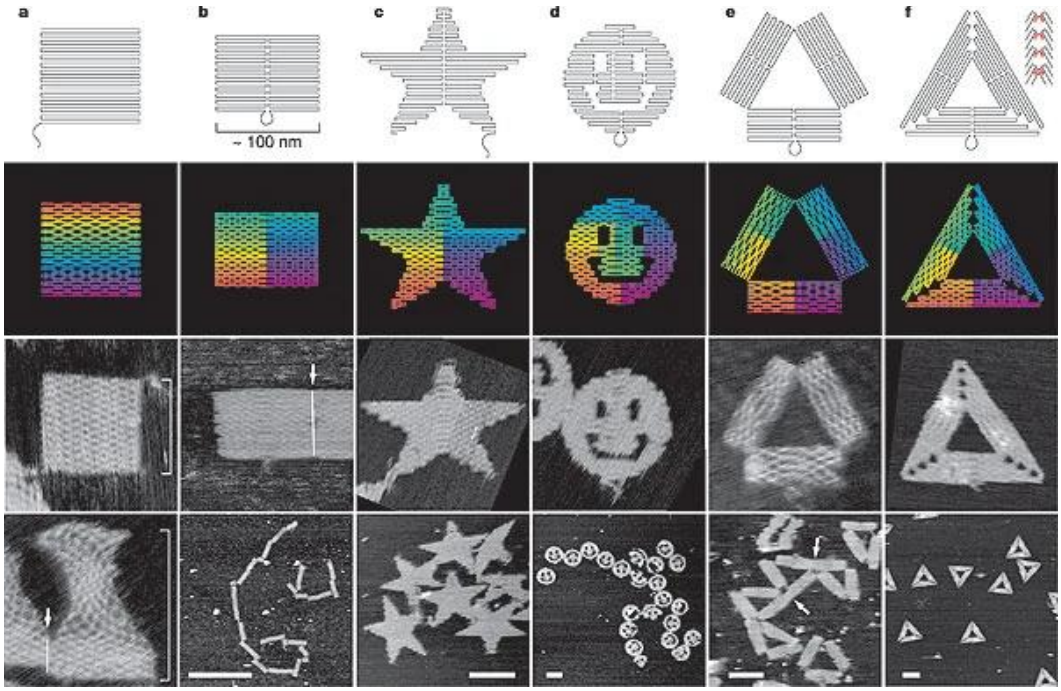

Figure 5: Different DNA origamis designed by Rothemund, a) Square with a linear scaffold, b) Rectangle with a circular scaffold, c) Star with a linear scaffold, d) Smiley with circular scaffold, e) Triangle with a circular scaffold and rectangular domain, f) Triangle with a circular scaffold and trapezoidal domains. [Reprinted by Permission from: (15)]

In general, the crossovers in an origami can be classified into three types namely scaffold crossovers, periodic crossovers with minor grooves facing up and periodic crossovers with minor grooves facing down or so-called glide symmetry. The scaffold crossovers are formed where the DNA twist places it at a tangent point between helices. Based on all the crossovers the packaging of helices in precise spatial constraints the arrangement of helices in origami is divided into honeycomb lattice or square lattice (see Table 1) . In honeycomb lattice the crossovers are situated at every 7 bp along the helical axis or in other terms each strand in the double helical domain is rotated by 240° at which the crossovers are placed (10.5 bp= 360°-for B-form DNA). Thus, a helical domain can have only 3 possible neighboring helical domains (see Figure 6). Whereas in a square lattice, the crossover are places at intervals of 16 bp (2D) or 8 bp (3D) deviating from the natural twist of DNA (10.5 bp per turn) causing slight underwinding (10.67 bp per turn leading to 8 bp crossover) or overwinding (10.4 bp per turn) in the double helices and having a maximum 4 possible neighbors. In case of underwinding the backbone

of the double helices rotates to an angle of 270° at every 8 bp crossover leading to twisting torques which can cause a global twist deformation of the entire origami. In case of overwinding the global twist, deformation can be avoided assuming the near natural twist of DNA (see Figure 6).

Honeycomb Lattice	Square Lattice
Porous Structure	Dense Structure
Hexagonal symmetry	Rectangular symmetry
Every 7 bp crossovers	Every 16-8 bp crossovers
3 neighbors per helix	4 neighbors per helix

Table 1: Difference between Honeycomb and Square Lattice.

The staples not only help in the formation of DNA origami, but also in its decoration with various entities such as proteins, peptides, drug molecules, antibodies and fluorophores with increasing diverse applications such as biomedicine,(*19, 20*) nanophotonics,(*21, 22*) lithography masks,(*23*) drug delivery,(*24, 25*) and biosensing.(*26, 27*) Furthermore, all these applications have led to a significant increase in the growth of the whole DNA nanotechnology field and expanding its horizons.

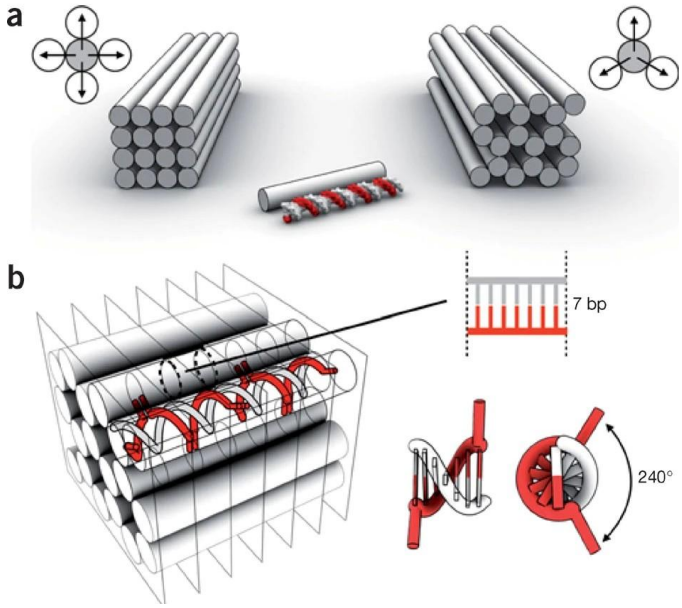

Figure 6: a) Cross sectional view of 3D DNA origami in square lattice (left) and honecomb lattice (right) packing. b) Cross overs arrangement in a hexagonal lattice at 7 bp with an average backbone rotation of 240°. [Reprinted by permission from: (16)]

1.2.2 DNA Origami Lattices

The technique of DNA origami provides a robust framework for the creation of modular DNA structures called DNA origami lattices, which can be employed in numerous nanopatterning tasks as well as in the construction of higher-order self-assembly systems. The first hierarchical assembly of programmable DNA was demonstrated by Seeman et.al., using Holliday junctions,(*28*) and three space

spanning DNA motifs.(*29*) These early breakthroughs illustrated the potential of DNA based structures to form well defined, addressable patterns and laid the groundwork for the rapid evolution of nano-patterning of different surfaces using DNA origami. The dynamics of these assembled nano-patterns remain only partially understood. Various efforts have focused on elucidating the mechanism of assembly based on various conditions such as surface assisted assembly and bulk-solution assembly with the aim of achieving greater control over lattice quality and order.

In terms of different approaches, the bulk solution assembly(*30, 31*) depends on the DNA origami structure interaction through attractive forces acting intermolecularly, such as sticky end hybridization (extended sequences of one structure that hybridize with complementary sequence of other structure) and blunt-end stacking (base stacking of truncated duplex ends). With respect to surface assisted assembly the origami structure adsorb onto solid-liquid (e.g., mica, silicon),(*32–34*) lipid-liquid (e.g., lipid bilayer) (*35, 36*) or air-liquid interface.(*37*) These interfaces confine the structure to a 2D plane, enabling lateral diffusion and order lattice formation provided there is sufficient concentration of monomers of the DNA origami.

The assembly dynamics on mica surface as a substrate for adsorption of DNA origami is very well studied. Mica is a negatively charged surface and DNA also being a negatively charged molecule there is repulsive force acting between them leading to no adsorption of origami on the surface. But divalent ions like Mg^{2+} forms salt bridges between the origami and mica surface enabling the adsorption of origami. With the addition of monovalent ions like Na^{+} there is reduced attraction and displacement of Mg^{2+} on the surface and origami leading to mobility of the origami on the surface enabling the dynamic defect correction, where smaller defects are annealed through replacement with other origami in the solution. Depending on the cation and monovalent ion and their respective concentrations in the solution the interaction and mobility dynamics of the origami on the surface changes leading to either a more ordered lattice or disordered one. For example, Kielar et.al., found that 75 mM Na^{+} and 10 mM Mg^{2+} yielded the most ordered DNA origami lattices without any blunt or sticky ends.(*38*) Whereas in a following study, Yang et.al., replaced the Mg^{2+} with Ca^{2+} leading to a much higher ordered lattice.(*34*)

Supported lipid bilayers, mimicking biological membranes, serve as dynamic substrates for DNA origami assembly (see Figure 7). Electrostatic and hydrophobic interactions facilitate adsorption, allowing structures to diffuse and form ordered lattices. DNA origami can be functionalized with hydrophobic moieties like cholesterol to enhance substrate interactions and control orientation.(*39*)

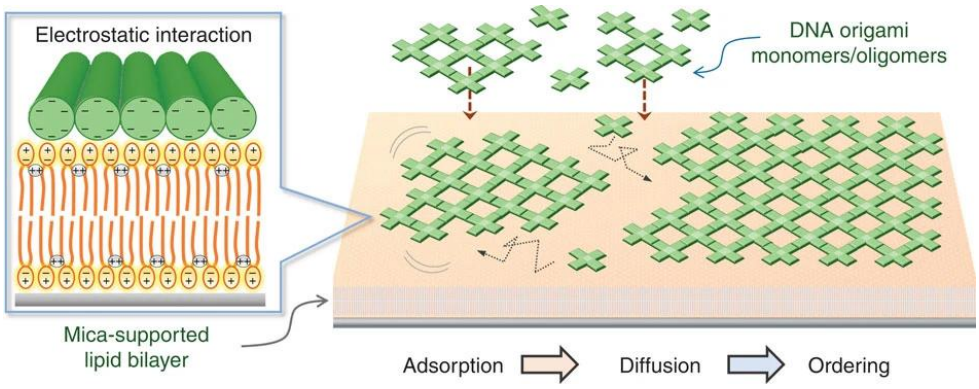

Figure 7: Schematic representation of Lipid Bilayer assisted DNA origami lattice formation. [Reprinted by permission from: (36)]

Furthermore, the dynamics of lattice formation can be controlled by external stimuli like temperature, pH, light and ionic strength. By incorporating specific triggers into DNA origami structure, these lattices can reversibly assemble, disassemble or reconfigure enabling their use in a wide range of applications like sensing and diagnostics. Temperature is a critical factor as sticky end hybridization and base stacking are sensitive to temperature. Increasing the temperature weakens this interaction leading to lattice disassembly. For instance, Zhang et al., employed shape complementary blunt end stacking to assemble 3D rhombohedral lattices from "tensegrity triangles" that disintegrated upon heating to a specific threshold (50 °C).(*40*) Whereas, pH-sensitive motifs, such as i-motifs and triplex DNA structures, enable DNA origami lattices to respond to change in pH. These motifs undergo structural transformations based on surrounding pH, allowing controlled assembly and disassembly. For example, Wang et al. employed a flexible and pH sensitive i-motif sequence that could form a C-quadruplex at low pH leading to decrease in distance between adjacent origami units, the C-quadruplex when increased the pH could turn back into ssDNA. Based on this arrangement of i-motif the lattice orientation changed based on the pH into a simple cubic and simple tetragonal lattice.(*41*) Furthermore, light-responsive systems have emerged for controlling DNA origami lattices. Photoresponsive molecules, such as azobenzene and arylazopyrazole can be incorporated into DNA strands to enable light induced conformational changes. These molecules transition between cis and trans configuration upon exposure to UV or visible light, altering the hybridization properties of DNA strands. For instance, Yang et al. used azobenzene modified DNA to assemble and disassemble hexagonal DNA origami units into 1D chains by alternating UV and visible light exposure.(*42*)

DNA origami lattices have been employed in diverse applications, including protein patterning, nanoparticle assembly, vesicle manipulation.(*43*) Ramakrishnan et al. demonstrated their use as lithographic masks for directing non-specific protein absorption, enabling precise patterning of proteins like BSA and Redβ.(*44*) Similarly, AuNPs and AuNRs have been integrated into 2D and 3D DNA

lattices via electrostatic interactions or hybridization, facilitating the creation of photonic crystals and functional nanostructures.(*45, 46*)

1.3 Bacteria

1.3.1 Structure and Classification

Bacteria are single-cell organisms that are abundantly found in nature. They lack a nuclear membrane (prokaryotic) and divide by binary fission. They exist both in parasitic form and free-living form, they have incredible capacity to adapt to environmental changes around or in other terms evolve by spontaneous mutations required for their survival. These organisms are exceptionally small, measuring just a few microns in size, although there are some exceptions in nature. For instance, the bacterium *Thiomargartia magnifica* can reach an extraordinary size up to an average of 10 millimeters.(*47*)

Bacteria range in different shapes namely cocci (round or ellipsoidal cells), rods (elongated cells), spiral, comma shaped and filamentous branched cells. Further bacteria can be classified as motile and non-motile based on the surface appendage for locomotion called flagella (typically 5-20 µm long, 10-20 nm in diameter).(*48, 49*) These flagella appendages are dominantly found on bacilli bacteria but rarely on cocci.(*50*) Furthermore, two other commonly found surface appendages on bacteria are pili and fimbriae. Pili are long, flexible, filamentous appendages composed mainly of protein pilin. There are generally used in bacterial conjugation (transfer of DNA between bacterial cells), motility, and adhesion and colonization based on the type of pili protruding from the bacteria. (*51*) Whereas, fimbriae are short, rigid, hair-like structures composed predominantly of the protein fimbrillin and are typically found more numerous than pili as surface appendages. There primary role involves adhesion and biofilm formation, which is crucial for colonization of bacteria.(*51*) The term pili and fimbriae are used interchangeably by people.

Furthermore, Gram-staining a differential staining technique that could differentiate bacteria based on their staining properties of cell wall as Gram-positive and Gram-negative was developed by a Danish bacteriologist Hans Christian Gram in 1884.(*52*) These difference in staining properties can be attributed to the drastic differences in the organization of cell envelope or cell wall. Gram-positive bacteria have a thick and continuous peptidoglycan layer of 20-80 nm (see Figure 8) also called sacculus. The thick peptidoglycan layer consists of teichoic acid, peptidoglycolipids and β-1,4 linked N-acetylglucosamine and N-acetylmuramic acid disaccharide units which are cross linked by short peptides and followed by a layer of membrane.(*53*) In the Gram-negative bacteria the peptidoglycan layer (7.5-10 nm) is thin and probably only a monolayer thick. Outside the peptidoglycan layer is an

outer membrane layer (lipopolysaccharides, porins) which is noncovalently bound to Braun's lipoproteins, and which are in turn covalently bound to peptidoglycan layer.

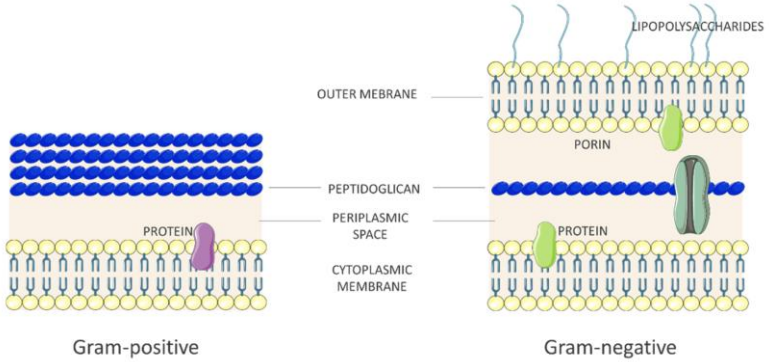

Figure 8: Gram positive cell with a thick peptidoglycan layer followed by periplasmic space and inner membrane, Gram negative cell with an outer membrane followed by a thin peptidoglycan layer, periplasmic space and an inner membrane.[Reprinted by permission from: (54)]

Followed by this is periplasmic space which is the region between the outer surface of the inner membrane (protoplast) and inner surface of the outer plasma membrane. This region consists of hydrolytic, aminoglycoside-modifying and plasmid encoded lactamases enzymes, binding proteins for transport of sugars and amino acids to inner membrane. Following this layer is the inner membrane which consists of phospholipids and proteins in a ratio of 1:3 respectively. The main function of the inner layer which is present in both Gram-positive and Gram-negative is basically active transport of molecules, energy transducing systems and biosynthesis of peptidoglycan and capsular polysaccharides.(*55, 56*)

1.3.1 Biofilm Formation and Factors Influencing the Formation

Bacterial biofilms are structured communities of bacteria encapsulated within a self-produced hydrated polymeric extracellular matrix (EPS), composed primarily of polysaccharides, proteins, extracellular DNA (eDNA), lipids and humic acid substances. These biofilms adhere firmly to surfaces and interfaces (biotic or abiotic), providing bacteria enhanced resistance to environmental stress, antimicrobial agents and host immune response.(*57–59*)

There are several stages of biofilm formation (see Figure 9), and it follows a sequential process:

1. Initial attachment: Planktonic bacterial cells attach reversibly to a surface via weak physiochemical interactions.
2. Irreversible attachment and microcolony formation: Bacteria begin secreting EPS, reinforcing their adherence and transitioning to irreversible attachment.

3. Maturation and growth: Microcolonies expand into structured biofilms, developing characteristic architecture with nutrient channels facilitating efficient nutrient distribution and waste removal.
4. Dispersion: Mature biofilms release cells, returning some bacteria to planktonic state to colonize new surfaces. (*60–62*)

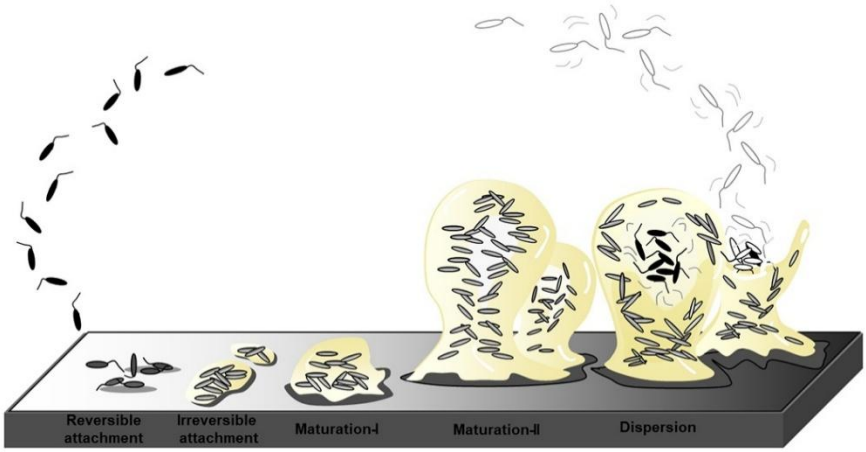

Figure 9: Schematic representation of stages of biofilm formation. [Reprinted by permission from: (63)]

Furthermore, there are several factors influencing biofilm growth and subsequent structural characteristics:

1. Surface properties: Surface roughness, chemistry, hydrophobicity and electrostatic interactions.(*64*)
2. Nutrient availability: Nutrient concentration and type profoundly affect biofilm density, thickness, and structural complexity. Limited nutrients can lead to thinner biofilms, whereas abundant nutrients typically thicker biofilms.(*65*)
3. Hydrodynamic conditions: Shear forces generated by fluid flow directly influence biofilm morphology and strength. A higher shear flow typically produces compact and stable biofilm with increased EPS production and signaling molecules and vice versa for a low shear conditions.(*64*)
4. Quorum sensing (QS): QS is a cell-to-cell communication mechanism where bacteria coordinate gene expression based on population density and survival needs for biofilm differentiation. (*66, 67*)
5. Presence of antimicrobials and stress conditions: Sub-inhibitory concentrations of antibiotics or antimicrobials compounds can stimulate biofilm formation as a bacterial defense mechanism. (*68*)

Furthermore, there are several studies indicating that various conditions and bacterial properties affect bacterial adhesion and subsequent biofilm formation in different ways, but these conclusions are always limited to certain types of bacterial species and not all bacteria can be treated in the same way to observe similar effects as the EPS composition and QS molecules will differ between different species.

1.4 Structure, Classification and Characteristics of Viruses

Viruses are microscopic entities significantly smaller than bacteria and eukaryotic cells. The first virus ever discovered was in the 19th century (1892) by Russian Microbiologist Dmitry I. Ivanovsky while studying a diseased tobacco plant and the virus found was a tobacco mosaic virus.(*69*) Their size ranges from 20-200 nm, though some can exceed 1000 nm (e.g., Pithovirus and Pandora virus). Viruses rely entirely on host cells for replication, assembling new virions de novo rather than dividing cells.(*70*) The structure of viral particle consists of :

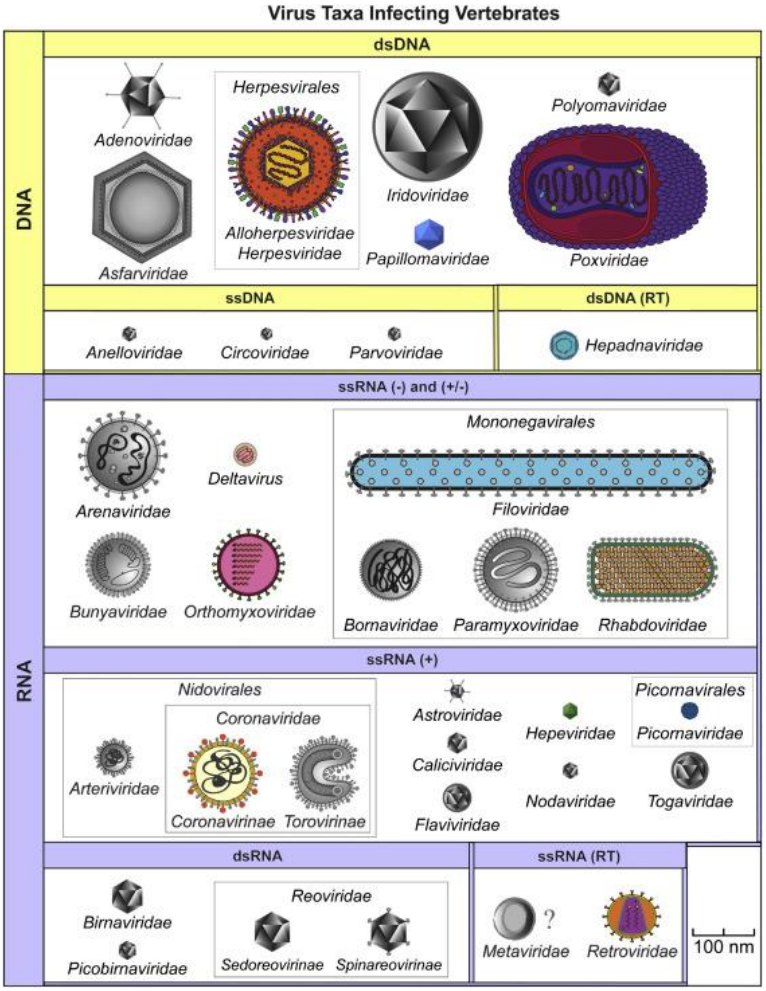

Figure 10: Classification of viruses based on their nucleic acid content and classified based on distinguishing characteristics. [Reprinted by permission from: (71)]

1. Capsid: A protein shell surrounding the genetic material, the capsid comes in two predominant shapes i.e., helical and icosahedral. Although, some viruses exhibit unique architecture that deviates from helical or icosahedra patterns.
2. Envelope: Some viruses are enveloped with lipid membrane derived from the host cells, which others are naked (non-enveloped).

Each virus also possesses a virus attachment protein embedded in its outermost layer i.e., capsid in the case of naked viruses and the envelope in the case of enveloped viruses. These proteins facilitate the docking of virus to the plasma membrane of the host cell.

Classification systems like the Baltimore scheme categorize viruses into seven classes based on their genome type (Either DNA or RNA) and replication strategy (see Figure 10), while the ICTV system uses a taxonomic hierarchy (order, family, genus and species).(*70, 71*)

1.4.1 Zika Virus

Zika virus (ZIKV) is a mosquito-borne pathogen first identified in Uganda and isolated from a sentinel rhesus monkey in year 1947. It belongs to Flavivirus genus with the Flaviviridae family, sharing lineage with other viruses such as dengue, yellow fever and West Nile. Flavivirus are transmitted via hematophagous arthropods such as ticks or mosquitoes (belonging to genus *Aedes*). Flaviviruses are small, lipid enveloped, and the genome consists of a positive polarity single stranded RNA. ZIKV is an icosahedral viral particle approximately 40 nm in diameter, characterized by a smooth surface and an RNA genome of about 10.8 kilobases (kb).(*72, 73*) The viral membrane is derived from the host cell membrane and is embedded with envelope glycoproteins (E) and membrane proteins (M) (180 copies each of E and M protein). The E protein forms a smooth, herringbone-like pattern on the surface and is generally in dimer form (see Figure 11). Upon entering the human body ZIKV targets epidermal keratinocytes, skin fibroblasts and langerhans cells.(*73*)

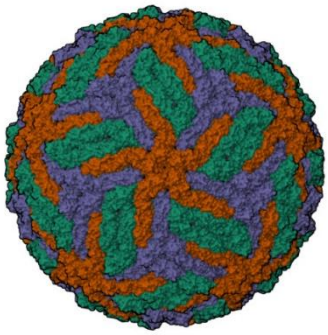

Figure 11: Structure of Zika virus at a resolution of 3.1 Angstrom. Orange-one subunit of the dimer, green-complementary subunit of the E-protein dimer, purple- M protein beneath the E-protein layer involved in viral assembly and maturation) and organized into rafts.(74) [PDB ID: 6CO8]

While many ZIKV infections are asymptomatic, symptomatic cases often present with mild fever, rash, conjunctivitis, muscle and joint pain, and headache. However, ZIKV has been linked to severe neurological complications.(*75, 76*)

1.4.2 Bacteriophages: Diversity, Classification, and Life Cycle in the Prokaryotic Virosphere

Bacteriophages belong to the prokaryotic virosphere and are exceptionally diverse. They differ widely in their shape, size and genome (3.4 - 500 kb). They were first discovered in 1915 by William Twort and in 1917 that they had the potential to kill bacteria. Phages have been classified based on their life cycle into two possible types called lytic and lysogenic cycles. The lytic cycle is where the phage infects the bacteria, multiplies itself by inserting its genome into the bacterial genome and then kills the host. In contrast to the lytic cycle, the lysogenic cycle involves phages integrating their genome into the bacterial host genome or existing independently as plasmids, allowing replication alongside the bacterial DNA for multiple bacterial generations without causing immediate bacterial death. Under specific environmental stresses or external triggers, these integrated phages can reactivate, initiating viral replication and transitioning to the lytic cycle. Phages exhibiting this conditional behavior are sometimes referred to as pseudolysogenic phages. The other characteristic of the lysogenic phages is their ability to convert their host phenotype by coding for new proteins or toxins.(*77*)

Based on their structure and genome (DNA and RNA-single or double stranded) (see Figure 12) phages are further classified as polyhedral (*Microviridae, Corticoviridae, Techtiviridae, Leviviridae and Cystoviridae*), filamentous (*Inoviridae*), pleomorphic (*Plasmaviridae*) or connected to a tail (*Caudovirales*).(*78*) In general the replication and lytic cycle of bacteriophages consists of 4 stages i.e., recognition of a suitable host, the transfer of genetic material to the host, take control of bacterial metabolic machinery for production of new phages and lastly to escape from the host by lysis.(*79, 78*)

The phages in general have a highly symmetrical capsid protein layer which envelops the DNA and acts as an external barrier for protection of its genetic material. In general, these capsids are icosahedral in shape but families like *Inoviridae* have a filamentous rod-shaped form of the same. Followed by the capsid is the head to tail interface or in simple terms connector which bridges the tail and head of the phages and serves like a valve for closing the head and keeping the genome inside the head under high pressure. Followed by this is the tail which can be contractile, non-contractile and short or long in its form based on the bacteriophage like for example *Podoviridae* have short tails and consist of adhesive devices for binding to host bacterium and *Myoviridae* have long contractile tails that consists of different proteins forming an inner rigid tube and an outer contractile sheath. Followed by the tail

is the Adsorption apparatus limited to some phages like that belong to *Siphoviridae* called distal tail proteins which help in recognizing and connecting bacteria.(*80, 79*)

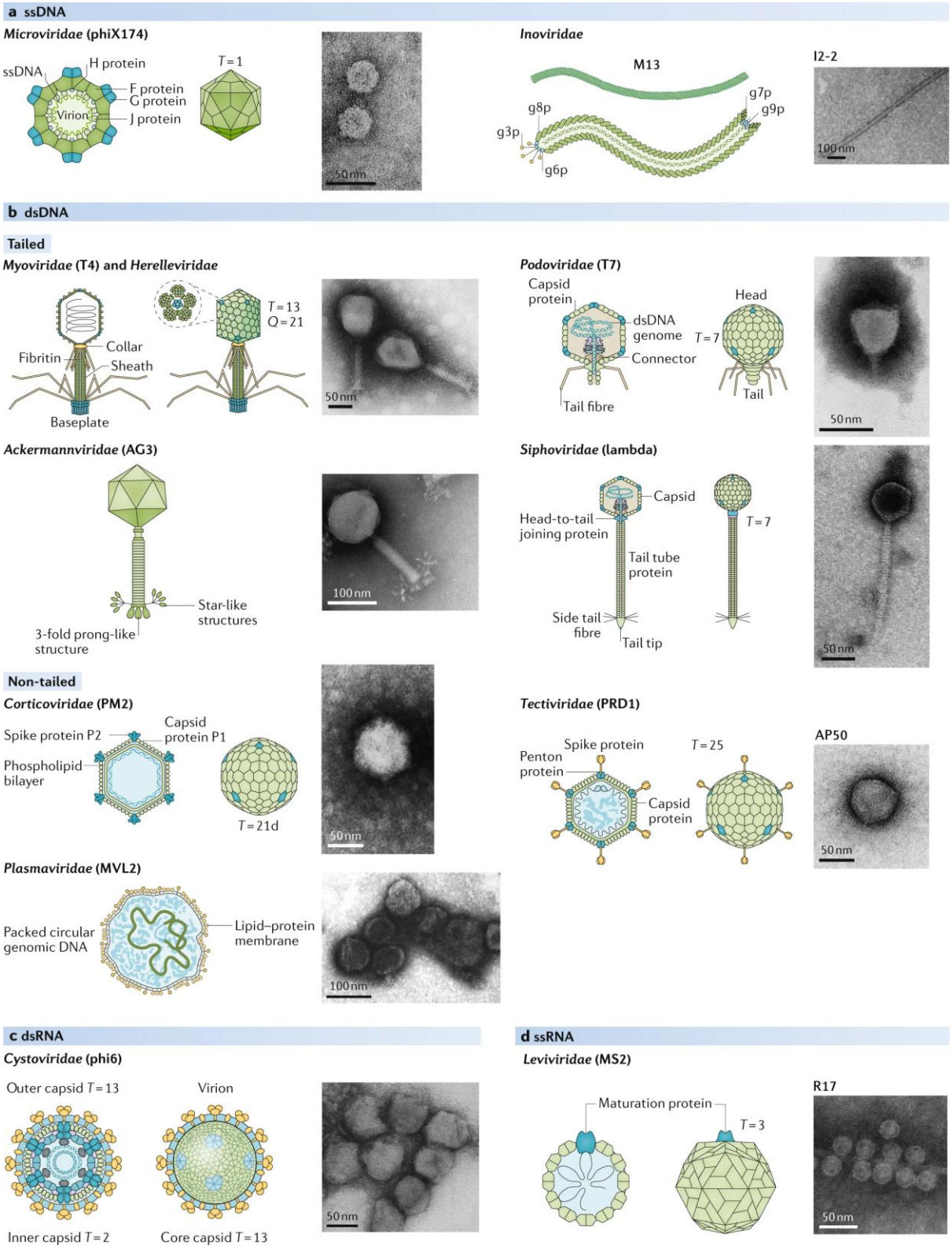

Figure 12: Phage classification based on morphology and genome type. [Reprinted by permission from: (78)]

1.5 Self-Assembled Monolayers

Self-assembled monolayers (SAMs) are ordered molecular assemblies that spontaneously form when thiols, silanes and phosphonic acid related compounds adsorb onto metal surfaces. SAMs are crucial in nanotechnology for tailoring interfacial behavior of metals like gold, silver and palladium. They represent an accessible, flexible system for modifying surface chemistry and linking molecular level structures to macroscopic interfacial phenomenon such as wetting and friction. Generally, they are prepared by immersing clean substrates in dilute thiol solutions for 12-18 h. The molecules chemisorb onto the metal surfaces via sulfur-metal bond, forming a densely ordered monolayer. The molecular organization in SAM is highly ordered arrangement of alkyl chains (see Figure 13) with the terminal functional groups defining the surface properties.(*81*) Some examples include:

1. **-CH_3**: Creates hydrophobic, non-polar surfaces.
   Charge state at neutral pH: Neutral (non-ionizable).
2. **-OH**: Increases hydrophilicity and allows hydrogen bonding.
   Charge state at neutral pH: Neutral (non-ionizable at physiological pH).
3. **-COOH**: Facilitates covalent binding to amines and biomolecules.
   Charge state at neutral pH: Negatively charged (COO^-), deprotonated at pH ~7.
4. **-NH_2**: Provides reactive sites for chemical modifications.
   Charge state at neutral pH: Positively charged (NH_3^+), protonated at pH ~7.
5. **-CF_3**: Adds fluorophilic properties and is used in anti-fouling applications.
   Charge state at neutral pH: Neutral (non-ionizable).

The structure and quality of SAM depends on factors such as solvent, temperature, immersion time and purity of the thiol compounds. Ethanol is one of the most used solvents for this purpose because of its ease of use.

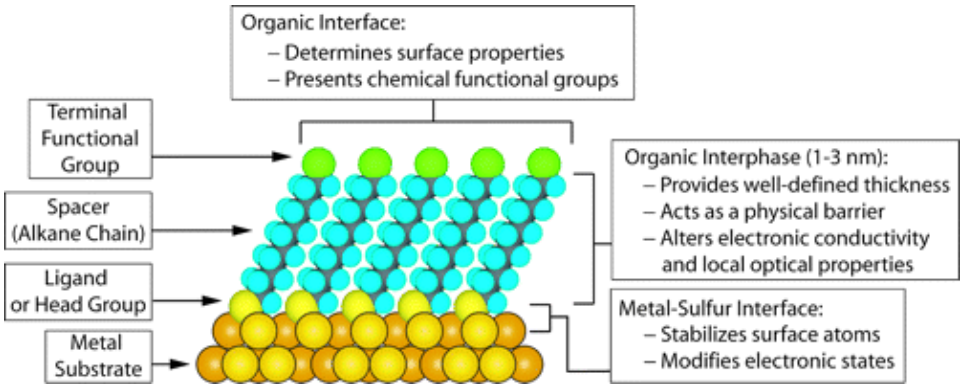

Figure 13: Schematic representation of a self-assembled monolayer (SAM) structure on a metal substrate. The three primary components represented here are: terminal functional group, the spacer (alkane chain) and the ligand or head group. [Reprinted by permission from: (81)]

Moreover, gold is widely studied and most used substrate for SAMs for its unique properties. It is chemically inert which prevents oxidation and reaction with most chemicals, allowing for handling under non-ideal conditions. Gold binds thiols strongly with forming substitutional sulfides and displaces surface contaminants effectively. Furthermore, gold is compatible with spectroscopic and analytical techniques like SPR, QCM and ellipsometry and it supports cell adhesion and function without toxicity.(*81*)

Chapter 2: Instrument Fundamentals

2.1 Quartz Crystal Microbalance with Dissipation (QCM-D): Principles and Applications

Quartz crystal microbalance with dissipation (QCM-D) is a technique to measure changes in mass and energy loss in a visco-elastic system based on the change in resonance frequency and dissipation of the sensor surface. propelled with a piezoelectric quartz wafer.

The phenomenon of piezoelectricity was initially discovered by the Curie brothers in the year 1880. In piezoelectric materials such as quartz, when stress is applied, an electric polarization is created (direct piezoelectricity), and in opposite to this when an external current is applied, there is an expansion or contraction of the crystal mechanically (inverse piezoelectricity).(*82*) This very property of inverse piezoelectricity is used in the QCM today, where a round chip of crystalline quartz is sandwiched between two metal electrodes and a sufficient AC voltage is applied close to the resonant frequency of the crystal (f_0), which is in turn an odd integer of the thickness of the crystal.(*83*)

The thickness of the crystal and the resonant frequency are inversely proportional to each other, indicating that the thinner the crystal, the higher the resonant frequency. The common resonant frequency is about 5 MHz for a AT cut crystal (see Figure 14A), representing a thickness of approximately 330 µm of the crystal and a density of approx. -17.7 Hz ng/cm^2.(*83*) The very basis of this property of quartz being commercially used in QCM is the linear relation between the frequency change and the mass adsorbed on the surface, which was first established by Sauerbrey in 1959.(*84*)

Sauerbrey equation:

$$\Delta m = -\frac{C}{n}\Delta f$$

C= constant (density of crystal at 5 MHz), *n*= harmonic number, Δf= change in frequency

This equation is valid, assuming that the adsorbed layer is rigid and that it is a monolayer covering the whole active surface. These assumptions are only valid for gaseous systems where there is no energy being lost or gained by the system. Whereas, in liquid systems, the viscoelastic nature of the adsorbed layer causes its frequency response of the sensor to vary, which is associated with energy dissipation. As a result, the fundamental assumptions of the Sauerbrey equation—namely, that the adsorbed layer is rigid and forms a uniform monolayer—are no longer valid.(*83*) This energy loss in the liquid system is related to the decay of crystal oscillation with the adsorption of a visco-elastic layer.

Moreover, the introduction of viscoelasticity as a new property in liquid studies brought about the concept of dissipation (D). The measurement of dissipation is determined by the decay in the oscillation of crystal near resonant frequency (see Figure 14C).(*85*) This unique property was successfully commercialized by Q-sense in 1996, along with enabling the examination of both *f* and D at various harmonics or overtones (n= 3, 5, 7, …..).

Furthermore, another particular advantage of QCM-D is that it is a non-destructive technique for the samples so it can be combined with other techniques such as Ellipsometry,(*86*) AFM, (*87*) SEM (*88*) and Fluorescence microscopy(*89*) to obtain further visual, dielectric, optical properties, and various other properties of the sample.

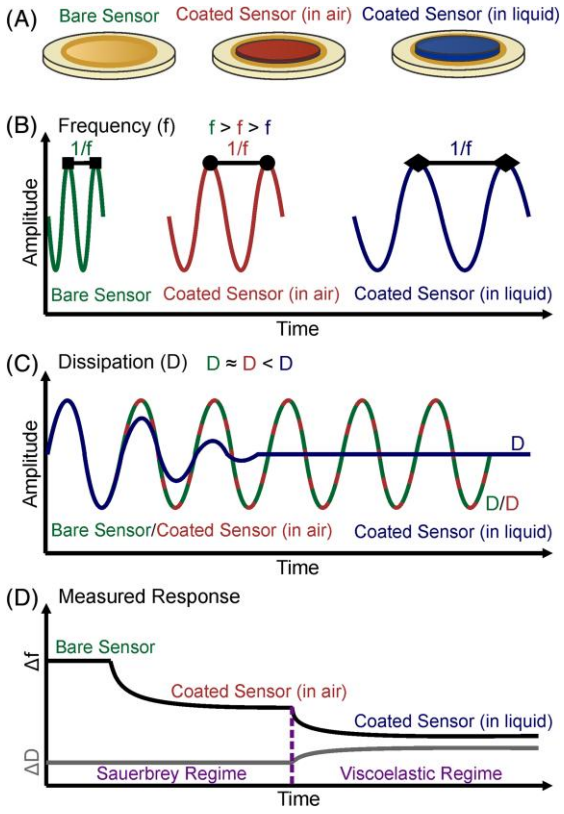

Figure 14: A) Illustrations showing a bare QCM-D sensor, sensor coated with a thin polymer film in air and the same polymer coated sensor swollen in liquid. B and C) Schematic representation of the qualitative changes in frequency and dissipation of the sensor oscillations, respectively caused by the polymer coating in air and its subsequent swelling in liquid. D) A conceptual QCM-D response curve showing the changes in frequency (Δf) and dissipation (ΔD) for a single overtone as the sensor is coated with polymer and later exposed to liquid, causing swelling. The Sauerbrey and viscoelastic model regimes are highlighted, with a decrease in frequency corresponding to an increase in the sensor's mass and an increase in dissipation reflecting the softening of the polymer film. [Reprinted by permission from: (90)]

Moreover, the utilization of liquid applications has significantly expanded the scope of possible investigations. Intermediate systems like protein can be studied for their interaction with other materials for development of biomaterials,(*91, 92*) to evaluate biocompatibility,(*93*) and to study the effect of surface polarity and protein concentration on the adsorption kinetics(*94, 95*) based on both

f and *D* and can be fit to Sauerbrey relation. But, in complex systems such as cells the shear wave of oscillating quartz is dampened out before even reaching the middle of the cell. The diameter of a typical cell is approximately 10 µm, which is significantly larger than the decay length of the shear wave in water excited by a 5 MHz AT-cut QCM (which is about 250 nm). For instance, Leino et al. elucidated a noteworthy behavior within this intricate mechanism, where the frequency behavior does not correspond with the number of bacterial cells adsorbed on to the surface.(*96*) Thus, the relationship between frequency shift (Δf) and mass described by the Sauerbrey equation tends to underestimate the actual mass adsorbed on the surface. This is because, when the adsorbed layer is viscous, internal friction arises due to deformation within the adlayer. Additionally, changes in energy dissipation (ΔD) become significant, as the adsorbed mass often includes associated water. The more viscous the adsorbate, the greater the deformation is induced by the sensor's oscillations.

One significant phenomenon observed in QCM-D measurements is the “missing mass effect”, where the apparent mass derived from the frequency shifts is less than the actual mass adhered to the sensor surface. This effect arises from the visco-elastic properties of the film, as well as interaction with the surrounding medium. For instance, Voinova et al. demonstrated that viscoelastic films exhibit dynamic motion under acoustic waves, which reduce the effective mass contributing to the frequency shift.(*97*) Furthermore, in liquid-phase applications, the density and viscosity of the surrounding liquid interacts with the film, further attenuating the sensors response.(*98, 99*)

Another intriguing aspect of QCM-D is the observation of positive frequency shifts despite mass being adsorbed on the surface. Where this phenomenon can be attributed again to the viscoelastic properties of the film. For example, stiffening of a layer due to drying, cross-linking or conformational changes can increase the resonance frequency, as the elastic contribution dominates over the mass loading effect.(*100*) Weak adhesion or partial decoupling of the film from the surface can also reduce acoustic loading, resulting in positive shift. Additionally, a decrease in dissipation (*D*) caused by increased rigidity of the layer may accompany such shifts, as observed in protein and cell adsorption studies.(*101*)

2.2 Scanning Probe Microscopy

Scanning probe Microscopy (SPM) is a technique where a sharp tip is physically used to scan a sample and collect information like magnetic, electronic, and adhesive properties of the sample.(*102*) The technique was invented in 1985 by Binning et al.,.(*103*) SPM has been classified into two further types called Scanning tunneling microscopy (STM)(*104*) and atomic force microscopy (AFM). Scanning tunneling microscopy is limited to conductive samples, and smaller scan area for its operation,(*105*) but AFM can physically scan both conductive and non- conductive samples, larger scan areas and

without any vacuum.(*106*) The extent of knowledge or information that can be obtained from both the systems is immense, depending upon the measurement being carried out. In relation to this thesis, attention is exclusively directed towards AFM.

2.2.1 Atomic Force Microscopy (AFM): Principles and Components

Atomic force microscopy is a powerful tool for exploring surface topography at nanoscale without need of complicated sample preparation procedures. In addition to mapping topography, the AFM system is capable of obtaining surface properties such as stiffness, adhesiveness, hydrophobicity, hydrophilicity, conductivity, visco-elasticity and surface potential.(*106, 107*) These attributes are applicable not only to non-biological materials but also biological specimens. Moreover, a significant advantage of this technology is its versatility, allowing measurements to be conducted in diverse conditions at solid-air, solid-liquid and lipid-liquid interface. (*108, 109*)

The key components of the AFM system include an AFM probe (cantilever), laser, Z-scanner (piezo) and a photodiode (see Figure 15).

1. Cantilever: The cantilever is a small, flexible beam with a sharp tip at its end with the other side coated with a reflective metal for the reflection of the laser. The flexible beam bends in response to the molecular forces on the sample surface.
2. Laser system: The laser used in the AFM system is typically in the visible or near- infrared spectrum. The laser is directed on the backside of the cantilever which is further reflected and is monitored with a photodiode.(*110*) The laser spot is kept small to accurately monitor the cantilever deflections and to ensure minimal interference.
3. Photodiode: A photodiode is a position sensitive detector of laser beam from cantilever. It is a quadrant cell consisting of 4 photoactive segments (anodes) each separated by 10 µm with a common cathode.(*110*) When the cantilever oscillates over the sample surface and because of the forces between the tip and the sample surface, the reflected laser spot moves on the photodiode. Further, this movement of laser on the photodiode is a measure of both lateral and vertical deflection of the cantilever helping in generating the topography of the surface. The vertical and lateral movement are calculated by taking difference in the signal levels measured in each quadrant.(*111*)

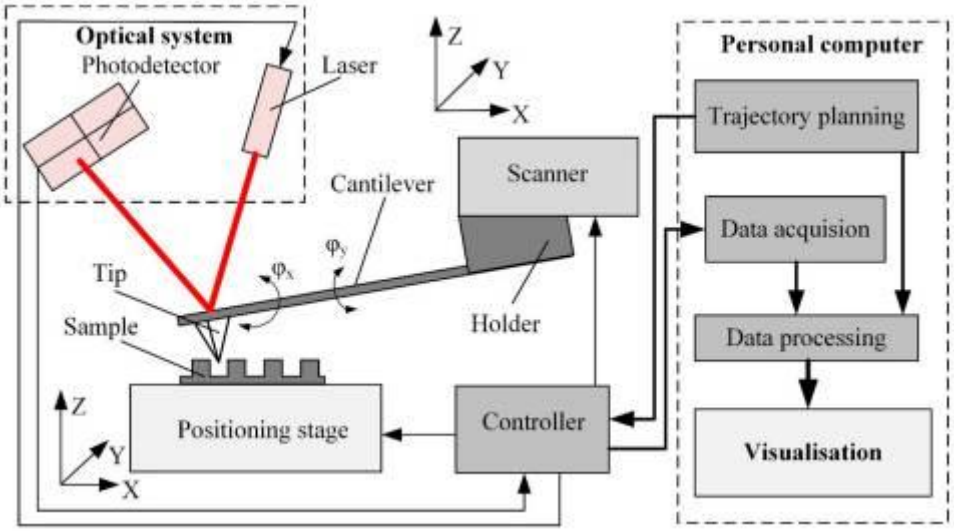

Figure 15:Schematics of an AFM system with the tip mounted on a piezoelectric scanner, further also representing how the controller acts on the system to control the imaging process. [Reprinted by permission from: (112)]

2.2.1.1. Tip-Sample Interactions in Atomic Force Microscopy

As the tip approaches the sample the distance between the tip and sample becomes so small that the resonance frequency of the cantilever starts shifting because of the interaction between the tip and sample. When the forces are attractive the shift in resonance is more towards a negative regime or in other terms its reduced and when its repulsive forces acting the shift is more towards the positive regime or in other terms the resonance increases.(*113*) Further, the attractive forces are also termed as short-range forces which develops from the chemical bonding of tip and sample, also including Pauli's repulsion due to the overlap of electron clouds of the tip and sample atoms. The long-range forces similarly include the van der Waals forces and electrostatic forces.(*114*)

2.2.1.2 Operational Modes of Atomic Force Microscopy

Atomic Force Microscopy (AFM) operates in various modes that are contingent upon the characteristics of the sample surface and the specific measurements required. Consequently, the operational modes must be adjusted accordingly.

1. Contact Mode: In contact mode, static mode or repulsive mode, the cantilevers tip scans the sample surface while being in direct contact (see Figure 16b) with the surface where it operates in the repulsive force regime (indicated in panel of Figure 16a). During the scans the laser is deflected in z-direction according to height changes of the sample surface and changes in the z-direction of the laser are recorded on the photodiode. The primary interactions between the probe tip and the sample surface initially involve van der Waals attraction, which becomes increasingly significant as the tip approaches the surface. Upon further approach, electron clouds of the tip and sample overlap, causing the attractive forces to diminish and

repulsive Pauli exclusion forces to dominate and compensate the attractive forces. This repulsive interaction along with applied external force by the cantilever leads to measurable deflection of the cantilever.(*115, 116*)

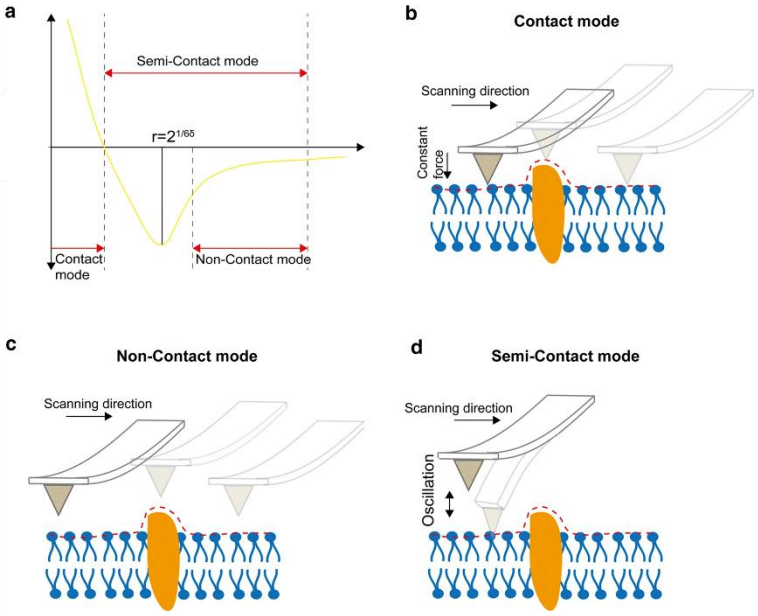

Figure 16: a) Interatomic force vs. distance curve. b)Contact mode: the probe lightly contacts the sample with constant force. c) Non-contact mode: the tip oscillates above the surface, detecting long-range forces without contact. d) Tapping mode: the cantilever oscillates near resonance, intermittently contacting the sample. [Reprinted by permission from: (117)]

2. Non-contact mode: In non-contact mode, the tip oscillates with a small amplitude (< 5 nm) near the sample surface (see Figure 16c), without touching it, at or slightly above the resonance frequency of the cantilever. Generally, the forces between the tip and sample are van der Waals forces and these forces cause a shift in the resonance frequency of the cantilever in the attractive regime. This shift in frequency is measured and used to generate an topographical image of the surface.(*114, 118*)
3. Tapping Mode: In tapping mode, the cantilever oscillates near its resonant frequency, and the tip intermittently contacts (see Figure 16d) the sample surface. There are reduced lateral forces compared to contact mode, which reduces the sample damage caused by the tip and further provides high resolution topographical data. Further, the system also captures the compositional contrast in heterogenous samples by recording the difference between external excitation and tip motion which is also known as phase imaging. This cantilever oscillates between both attractive and repulsive regime.(*119, 118*)

2.2.1.3 Setpoint and PID Feedback System and their Role in Atomic Force Microscopy

In AFM, the setpoint is a pre-defined value of cantilever deflection (in contact mode) or amplitude reduction (in tapping/non-contact mode) used as a feedback reference during scanning. It determines

the strength of interaction between the AFM tip and the sample surface.(*113*) During scanning the feedback system (explained below) constantly adjusts z-height to keep the deflection of oscillation amplitude equal to the setpoint. These vertical (z-axis) adjustments are recorded at each (x, y) position on the surface and the resulting topographical AFM image represents the variation in height required to maintain the specific interaction strength (setpoint) between the tip and sample. Too high setpoint may damage the sample, deform the surface or prematurely wear down the tip and to low setpoint may result in weak contrast of the resulting image and insufficient resolution.

The proportional-integral-derivative controller is a main component of the AFM which helps in maintaining appropriate distance of the probe(*120*) from the sample or in other terms a quick reaction system for detecting height changes (z-direction) on the surface based on the changes in the deflection or amplitude of the laser on the photodiode from the cantilever beam and further maintaining the constant interaction forces between the tip and sample. Typically, in terms of AFM software the values of the controller are associated with simple terms, namely gain. Higher gains lead to quicker response of the system resulting in a noisy image. Whereas lower gain leads to a slower response of the system resulting in a blurry image caused by increased dwell times.

The proportional component of the PID controller applies a quick response correction that is proportional to the error (the difference between the measured values and the setpoint). The integral component integrates error overtime and applying corrections based on an accumulated error. The derivative component extrapolates error by calculating the rate of change of the error. All these components provide continuous feedback and increase the system's stability.

2.2.2 High Speed Atomic Force Microscopy (HS-AFM): Advancements for Real-Time Visualization of Biological Dynamics

High speed AFM was developed in 2001 by Toshio Ando for visualization of dynamics of biological molecules in action at sub-100 ms temporal resolution and 0.1 nm vertical resolution.(*121–123*) There are some major requirements for HS-AFM to work in comparison to normal AFM and the requirements are ultra short cantilevers in range of 6-10 µm long and 2 µm wide with comparison to normal cantilevers which typically have a length ranging 100-500 µm and width of 30-50 µm,(*112, 124*) a dynamic PID controller which has a faster response feedback capability and automatic gain tuning during imaging than a conventional PID(*125*), laser deflection detector optimized for smaller cantilevers, fast scanner and an active vibration damping technique.(*122*) Furthermore, AFM typically employs tapping mode to minimize frictional forces, avoid lateral drag, and reduce sample damage, especially when imaging delicate biological samples. However, the contact mode can also be

employed for high-speed AFM imaging, allowing rapid acquisition of topographical data from certain robust samples.(*126*)

An ultra short cantilever with high frequency (f_c) is required to enable high speed AFM. Tiny cantilevers such these have typically 1/3 of f_c^{water} compared to f_c^{air} and such that the cantilever response to the impulsive force becomes 0.72 µs. Further the cantilever on its reflective side is coated with gold which increases the f_c by 10-20 % as there is an increase in stiffness of the cantilever, further this layer of gold coating helps in better reflection of laser onto the photodiode in liquid medium.

Chapter 3: DNA Origami Lattice Formation at Different Surfaces

3.1 Rapid Assembly of Highly Ordered DNA origami Lattices at Mica Surfaces

3.1.1 Introduction

Surface-assisted macromolecular self-assembly(*127–132*) is a promising and widely investigated strategy for the fabrication of functional surfaces and materials with promising applications in biomedicine,(*133*) biosensing,(*134*) and molecular electronics.(*135*) It is based on the adsorption of macromolecular building blocks at a solid surfaces under conditions that allow them to maintain some 2D mobility. These building blocks then assembly into networks and lattices via specific non-covalent interactions among themselves and/or with the surface. Various macromolecular building blocks can be used in this approach, including small organic molecules,(*136*) peptides,(*137*) proteins,(*138*) and DNA.(*139*)

DNA has proven as a particularly versatile material in surface-assisted self-assembly,(*140, 141, 43*) as recent advances in DNA nanotechnology enable the controlled assembly of highly ordered lattices(*34, 33, 142*) with various symmetries and unit cells(*143–145, 142*) over macroscopic surface areas several cm^2 in size.(*146*) Such lattices are typically assembled at mica surfaces(*147, 34, 146, 143, 145, 38, 148, 144, 149, 32, 150, 142*) or supported lipid bilayers,(*151, 39, 36, 152–155*) but efficient lattice assembly has recently been demonstrated also at SiO_2 surfaces.(*33, 156, 157*) Nevertheless, mica is usually favored as a substrate because mica-assisted DNA lattice assembly it is not as sensitive to environmental parameters and thus more robust, so that lattices with an astonishing degree of order can be fabricated in a straightforward and reproducible manner.(*156, 34, 38, 33*) In comparison, solution-based self-assembly of DNA lattices relies solely on attractive interactions between DNA nanostructures and thus requires the precise fine-tuning of the connecting sticky or blunt ends (*141, 43*). Furthermore, deposition of 2D lattices assembled in solution on solid substrates usually leads to lattice distortions and sometimes even severe lattice damage (*158, 159, 15*) and the resulting surface coverage is usually much lower than in the case of surface-assisted assembly, through which homogeneous monolayer lattices have been fabricated over cm^2 surface areas. (*146*) The surface-assisted assembly of 2D DNA lattices thus is a robust method with various potential applications, ranging from the controlled arrangement of proteins (*143, 44*) and gold nanoparticles (*160, 150, 161*) to the fabrication of etch masks for molecular lithography patterning.(*157*)

Despite all those advantages, there are still some issues that need to be solved to enable the widespread application of DNA lattices assembled at solid surfaces. While the effects of several

experimental parameters on lattice assembly have already been investigated and optimized toward maximizing lattice order(*34, 38, 147*) and lattice size,(*146*) the timescales required for lattice assembly are still rather long. Depending on the monomer type and the environmental conditions, extended DNA lattices at mica and SiO_2 surfaces are typically assembled over timespans ranging from about one hour(*38*) to several days,(*145, 144*) with longer assembly times usually being favored as they result in higher lattice order(*38, 34, 147*) and larger surface coverage.(*143, 149*) For any real-world applications of DNA lattices, much shorter assembly times of the order of minutes would be highly desirable. However, previous studies already hinted at the possibility that increasing the monomer concentration may result in equivalent or even higher lattice order in shorter time.(*44, 34*) Therefore, in this work, we systematically investigate the effect of monomer concentration on the assembly and quality of hexagonal DNA origami lattices at mica surfaces by high-speed atomic force microscopy (HS-AFM). We find that at a rather moderate DNA origami monomer concentration of 6 nM, densely packed DNA origami monolayers (MLs) are observed already after about 2 min, compared to 10 min at 4 nM. Intriguingly, further increases in DNA origami concentration do not result in faster ML formation. At short length scales (≤ 1 µm), no differences between the DNA origami concentrations are observed once a ML has formed, which implies that high-quality DNA origami lattices can be assembled within 2 min at rather moderate DNA origami concentrations of 6 to 10 nM. Over larger length scales of a few microns, however, a DNA origami concentration of 10 nM results in slightly higher lattice order than other (higher or lower) DNA origami concentrations. We thus identified optimum conditions that enable the rapid assembly of highly ordered DNA origami lattices within few minutes, which represens a highly important step toward the industrial-scale application of DNA-based molecular lithography masks.

3.1.2 Results and Discussion

To assess the effect of monomer concentration on DNA origami lattice assembly, we used the Rothemund triangle(*15*) as the monomeric building block. For these DNA origami triangles, surface-assisted lattice assembly is a result of electrostatic interactions between the charged DNA origami nanostructures and the charged mica surface, with surface coverage being maximized by arranging the adsorbed triangles in a 2D hexagonal close packed lattice. This mechanism does not require any attractive interactions between DNA origami monomers and, therefore, can proceed without the formation of nucleation seeds.(*38*) For this system, lattice assembly kinetics and especially lattice order can be optimized by adjusting ionic composition of the medium, as the electrostatic interactions between the DNA origami nanostructures and

the mica surface depend on the species and concentrations of available monovalent and divalent cations.(*34, 38*) For the experiments, a buffer composition that was found in previous work to stimulate the assembly of highly ordered hexagonal lattices on mica surfaces, *i.e.*, 1xTAE supplemented with 10 mM $CaCl_2$ and 75 mM NaCl.(*34*) Under these conditions, a DNA origami concentration of 2 nM led to the formation of a densely packed ML in about 40 min.(*34*) This was verified in the HS-AFM images, which show only a slowly increasing surface coverage that does not yield a closed ML within 600 s of incubation. As can be seen in Figure 18, increasing the DNA origami concentration to 4 nM leads to notably faster assembly kinetics, with a densely packed ML being formed in about 600 s. Prolonged incubation beyond 600 s leads to rearrangements within the ML, which anneals lattice defects and continuously improves lattice order.(*34, 38*)

At a DNA origami concentration of 6 nM, lattice assembly is further accelerated, with a densely packed ML being observed already after 200 s (see Figure 18). Visual inspection does not reveal any major differences in lattice quality between the lattice obtained after 600 se at 4 nM and that obtained after 200 s at 6 nM. After prolonged incubation for 1000 s, both lattices still appear very similar. Even higher DNA origami concentrations up to 12 nM do not lead to faster lattice assembly.

To quantify these visual observations, a topological analysis was performed of all HS-AFM images recorded for each experiment. To this end, our previously developed software(*34, 146*) was adapted to enable batch processing of large HS-AFM image stacks. The web app (available at https://github.com/mariocastro73/avator) allows to import individual images and fine tune the software parameters to obtain a 100% accurate classification of the triangles (Developed and Analyzed by Mario Castro and David Contreras, Grupo Interdisciplinar de Sistemas Complejos and Instituto de Investigación Tecnológica, Universidad Pontificia Comillas de Madrid, Madrid, Spain). However, as the input images differ in coverage, it was necessary to calibrate different representative parameters for different time ranges. Then, information about the location of the triangles and the coverage can be exported, so that it can be processed with another software.

Figure 19a shows the DNA origami surface coverage as a function of incubation time for the different DNA origami concentrations. In agreement with the above qualitative assessment, surface coverage increases more slowly at a DNA origami concentration of 4 nM than at the higher concentrations, which all show a rather similar behavior. The time to ML formation as identified by the saturation of the surface coverage is given in Figure 19b for the different DNA origami concentrations. At a DNA origami concentration of 4 nM, ML formation occurs at about 600 s. At the higher concentrations, closed MLs are observed already after 100 to 150 s.

This increase in the lattice assembly rate may be related to the probability of the DNA origami triangles to form dimers in solution via blunt end stacking at their vertices. Higher monomer concentrations may lead to a larger fraction of DNA origami dimers adsorbing on the mica surface that can then act as additional nucleation seeds that stimulate lattice growth. There is no clear trend in the fraction of adsorbed dimers with monomer concentration. Therefore, it was assumed that the observed decrease in the time to form a closed ML is due to an increase in the arrival rate of the DNA origami triangles at the surface, even though the limited size of the HS-AFM images allows only a very small surface area to be analyzed. The observation that a further increase in DNA origami concentration does not result in faster ML formation indicates that the rate of DNA origami arriving at the mica surface is diffusion limited. To reach a target concentration of 10 nM in these experiments, a 500 µl sample of 20 nM DNA origami solution is manually injected into the liquid cell filled with 500 µl of DNA-free buffer. To reach the surface, the DNA origami nanostructures have to diffuse along the concentration gradient. Therefore, the local DNA origami concentration at the mica-liquid interface gradually increases until it reaches the nominal target value of 10 nM. To test this hypothesis, a control experiment was conducted, in which 28 µl of a highly concentrated DNA origami sample (360 nM) were injected into the liquid cell filled with 972 µl buffer to reach the same target concentration of 10 nM. Indeed, as can be seen in the AFM images shown in Figure 17, lattice assembly is severely delayed in this setting. Therefore, it was assumed that under conditions that are not limited by diffusion, lattice assembly will be even faster for DNA origami concentrations of 6 nM and more.

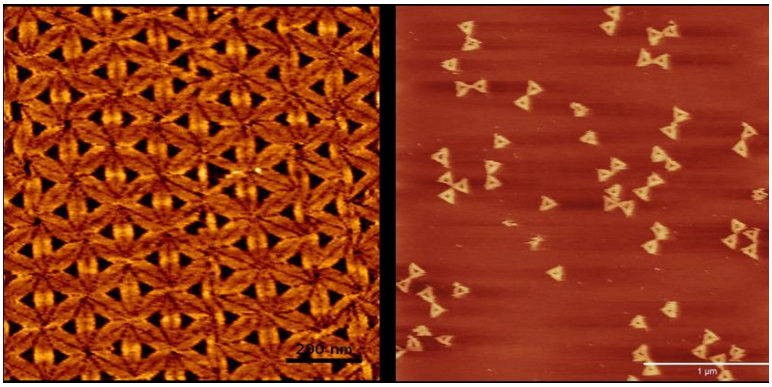

Figure 17: HS-AFM images of DNA origami triangles adsorbed on mica surfaces. Injection into the liquid cell was carried out at different sample-to-buffer volume ratios at a constant total concentration of 10 nM. Left: 500 µl sample (20 nM) injected into 500 µl DNA-free buffer. Image size 1 x 1 µm², incubation time 1242 s. Right: 28 µl sample (360 nM) into 972 µl buffer. Image size 3 x 3 µm², incubation time 2100 s.

To monitor the development of lattice order over time, a Delauney triangulation was computed (a dual geometric characterization of the Voronoi tessellation)(*34, 146*) and compute the distribution of triangle angles. For a perfectly packed DNA origami triangle lattice,

we would expect a peak distribution at 60°. Of course, randomness in the deposition, as well as tiny fluctuations in the automatic triangle discovery provided by our software, will broaden this distribution. However, we can expect that the order is related to the height of the histogram of angles around 60° (and using ± 5° bin width). Namely, it was denoted as the order parameter $n(\Theta_{60})$, *i.e.*, the number of angles around 60° per µm². This parameter is less sensitive toward boundary effects resulting from the finite size of the AFM images than parameters based on the nearest-neighbor distribution that were used previously to quantify lattice order.(*34, 146*)

Figure 19c show the evloution of $n(\Theta_{60})$ over time for the different DNA origami concentrations. Interestingly, the order parameter follows the same trend as the surface coverage. For all concentrations, it increases at early assembly times but saturates upon formation of a closed ML. After this point, it remains largely constant and does not exhibit any notable differences between DNA origami concentrations. This demonstrates that increasing the DNA origami concentration results in faster ML formation but does not affect the quality of the assembled lattices. Therefore, high-quality DNA origami lattices can be assembled within 2 min at rather moderate DNA origami concentrations of 6 to 10 nM.

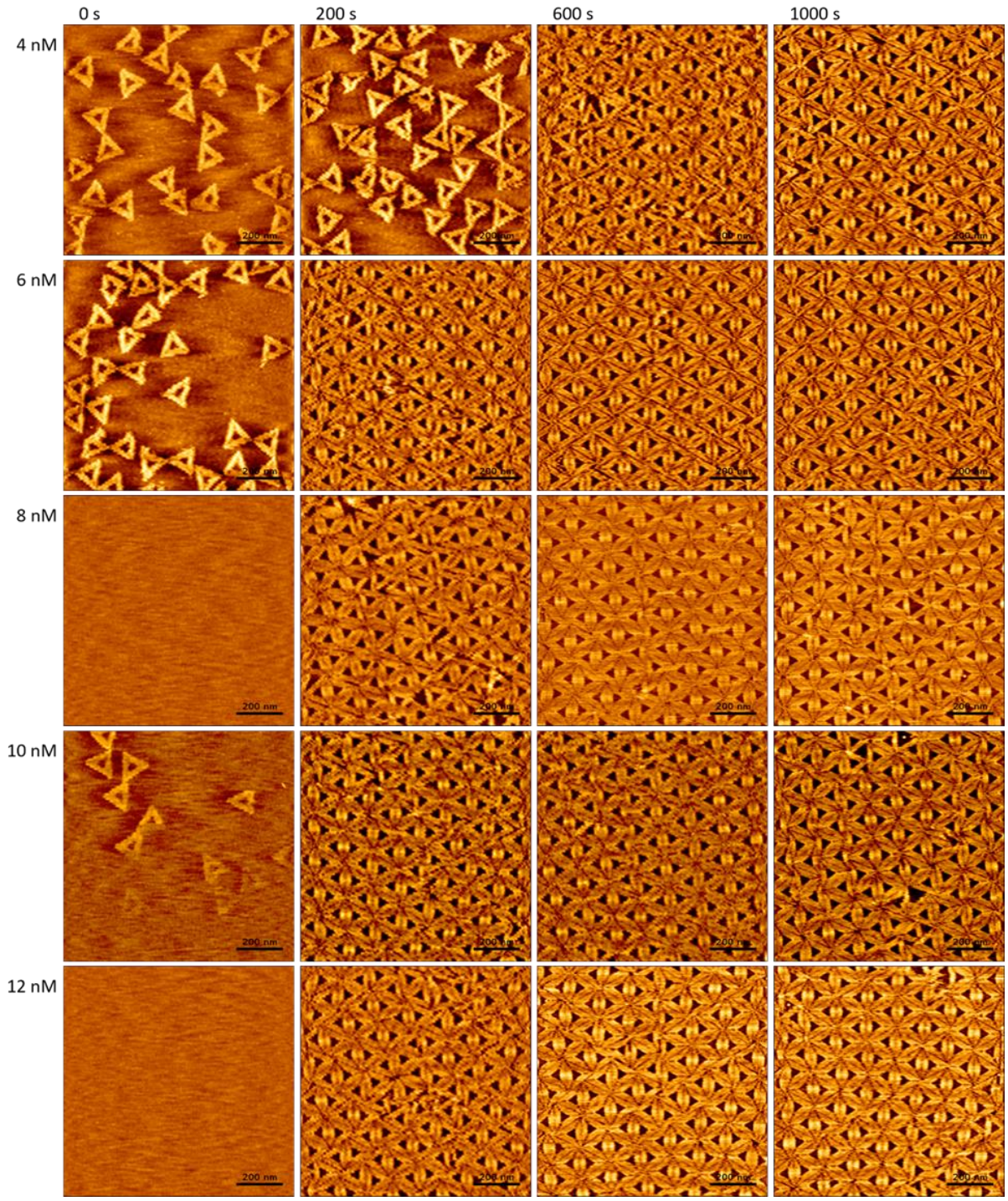

Figure 18:HS-AFM images (1 x 1 µm²) of DNA origami lattice assembly at different DNA origami concentrations recorded at different time points. The apparent differences in surface coverage at 0 s can be attributed to inhomogeneous surface coverage and variations in the manual injeciton of the sample solutions. The images were recorded at 1 frame per second (fps).

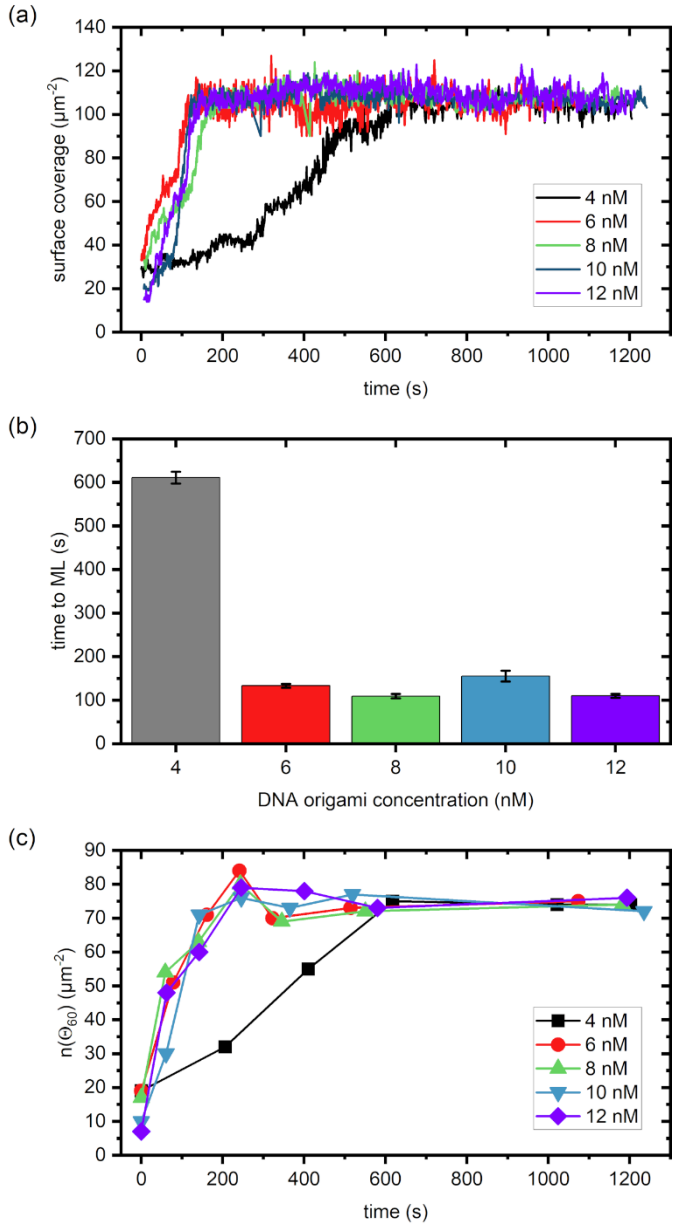

Figure 19: (a) Evolution of surface coverage over time. The 4 nM curve is statistically different ($p < 0.001$) from all other curves. (b) Time to monolayer (ML) formation extracted from the curves in a). (c) Evolution of the number of angles around 60° per µm², n(Θ$_{60}$), over time. There are no statistically significant differences in the final n(Θ$_{60}$) values obtained at the end of the experiments.

In the above experiments, the image size was limited by the high frame rate, so only rather small images of 1 x 1 µm² could be recorded. To assess lattice quality over larger scales, overview images 4 x 4 µm² in size were recorded at the end of each experiment, *i.e.*, about 25 min after sample injection. As can be seen in Figure 20, the obtained lattices are rather similar in appearance and exhibit the same general features. In particular, the lattices are rather homogeneous over these micrometer length scales but show some point and line defects at the grain boundaries. Such defects, however, may persist even for very long times and are observed also for assembly times exceeding one hour (*38, 34*). Despite the similar appearance of the different lattices, the fast Fourier transforms (FFTs)

shown in the insets, reveal some differences. Even though all FFTs exhibit very pronounced correlation peaks with hexagonal symmetry, one of the 4 nM images has a rather intense, diffuse background. With increasing DNA origami concentration, the intensity of the background decreases, until FFTs with extremely well-defined features are obtained at 8 and 10 nM concentrations. At 12 nM, however, the background reappears and the FFT again seems somewhat blurry. This is in line with the order parameter $n(\Theta_{60})$ shown in the bar chart of Figure 19, which has slightly larger values at 8 and 10 nM than at the other concentrations. Therefore, although no differences between concentrations are observed at smaller length scales, long-range order exhibits a small maximum at an intermediate optimum DNA origami concentration of 10 nM. At larger concentrations, $n(\Theta_{60})$ is decreased again. This is because development of order requires the annealing of defects by a local rearrangement of the DNA origami lattice, which is initiated after the spontaneous desorption of single triangles from lattice sites.(*38, 147*) If the DNA origami concentration is too high, this rearrangement is suppressed because as soon as a lattice triangle desorbs, its site in the lattice is occupied by a new incoming triangle from the bulk solution. It should be noted, however, that Fourier and topological analyses measure different aspects of what is generally termed order (*34*). Therefore, they are not fully comparable and may yield different assessments of lattice order for the same sample (*34*), which explains why the trend observed in the FFT images in Figure 20 is not reproduced in all details in the $n(\Theta_{60})$ data.

In these experiments, we have monitored lattice dynamics for about 25 min. However, previous works have shown that under similar conditions, lattice order increases constantly with time even after formation of a closed monolayer, albeit at a low rate (*34, 147*). Furthermore, the order parameters calculated from in-situ HS-AFM images may be affected by the continuously scanned AFM tip. It has been demonstrated previously that high scan rates such as the one used here may notably disturb biomolecular dynamics (*162*) and thereby negatively affect surface-assisted biomolecular self-assembly.(*163*) Under static conditions without external disturbances, the formed lattices may, therefore, exhibit even higher order parameters. Therefore, DNA origami triangles were incubated at the optimum concentration of 10 nM on mica for 20 and 67 min without continuously scanning the surface. After 20 min incubation, an order parameter of $n(\Theta_{60}) = 87\ \mu m^{-2}$ is obtained, which is identical to the one observed with continuous scanning in Figure 20. This indicates that the continuously scanned tip has only a minor influence on lattice order. However, after an additional 47 min incubation, the order parameter has increased to $n(\Theta_{60}) = 93\ \mu m^{-2}$. This verifies that longer incubation times will indeed lead to improved lattice order by the continuous annealing of defects as observed previously (*34, 147*). Whether such a comparably moderate improvement in lattice order warrants longer assembly times, however, will depend on the requirements of the envisioned application.

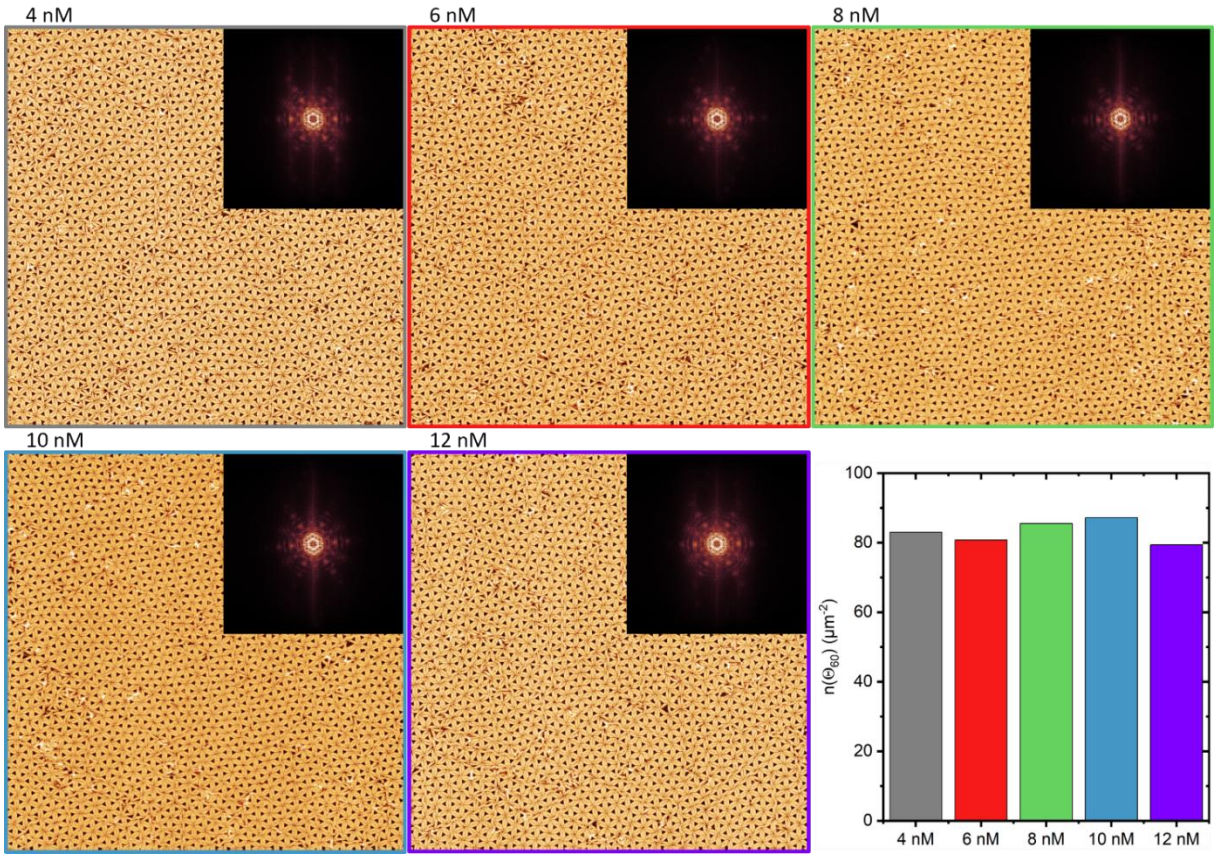

Figure 20: Overview AFM images (4 x 4 µm²) of DNA origami lattices assembled at different DNA origami concentrations recorded after approximately 25 min of incubation. The insets give the fast Fourirer transforms (FFTs) of each image. The bar chart gives the number of angles around 60° per µm², n(Θ60), calculated for the different AFM images.

3.1.3 Conclusion

The surface-assisted assembly of ordered DNA origami lattices at mica surfaces was investigated for different DNA origami concentrations. Using buffer conditions optimized for high lattice order and HS-AFM to monitor lattice assembly in situ at 1 frame per second, it was observed that the formation of ordered DNA origami lattices happens within minutes. At a low DNA origami concentration of 4 nM, formation of a regular lattice takes about 10 min, whereas similar lattices are obtained after 2 min for concentrations between 6 and 12 nM. Over short length scales below 1 µm, the DNA origami concentrations do not affect lattice order. However, a 10 nM concentration results in slightly improved lattice order at larger scales of several microns. This concentration thus appears to be the optimum for the rapid assembly of DNA origami lattices at mica surfaces.

The observation that increasing the DNA origami concentration from 6 to 12 nM does not result in faster lattice assembly kinetics is attributed to the dominant influence of DNA origami diffusion through the bulk volume after sample injection, which limits their rate of arrival at the surface. For the routine fabrication of DNA origami lattices for molecular lithography or other applications, it is thus recommended to use a different experimental setting, in which the substrate is getting immersed

in a well-mixed solution that contains the DNA origami nanostructures already at the final target concentration of 10 nM. Under such conditions, it can be expected that lattice assembly to occur almost instantly within less than 1 min.

3.1.4 Materials and Methods

DNA origami assembly and purification

The DNA origami triangles(*15*) were assembled using the 7249 nt M13mp18 scaffold (Tilibit) and 208 staples strands (Eurofins) at a tenfold staple excess in 1x TAE (Carl Roth) containing 10 mM $MgCl_2$ (Carl Roth). The solution was heated to 80 °C and subsequently cooled down to room temperature over 90 min in a thermocycler Primus 25 Advanced (PEQLAB). The folded DNA origami triangles were purified by spin filtering using Amicon Ultra 100K filters (Millipore). The molar concentration of the purified DNA origami nanostructures was estimated by UV/Vis absorption using an Implen Nanophotometer P330.

HS-AFM

HS-AFM was performed using a JPK Nanowizard ULTRA Speed 3 with USC F0.3-k0.3 cantilevers (NanoWorld) and a custom-made liquid cell. Different concentrations of DNA origami nanostructures suspended in 1x TAE (pH 8.5) containing 10 mM $CaCl_2$ (Merck) and 75 mM NaCl (VWR) were injected into the buffer-filled liquid cell to reach the final desired concentration in a total sample volume of 1 ml. The first AFM image of each experiment was recorded about 10 s after injecting the sample. Sample injection was performed manually, resulting in some variation between samples. This in particular concerns the exact timespan between injection and start of imaging, as well as the rate of injection and the place of injection within the volume of the liquid cell. Since the arrival rate of the DNA origami nanostructures at the mica surface is limited by diffusion, sample to sample variations of these parameters are responsible for differences in the number of adsorbed DNA origami triangles in the beginning of the experiments. For the first 10 min, HS-AFM images were recorded with 1 x 1 µm² scan size at a line rate of 200 Hz and a resolution of 200 x 200 pixels resulting in a frame rate of 1 frame per second (fps). After about 10 min, the resolution was increased to 400 x 400 pixels, lowering the frame rate to 0.5 fps. After about another 15 min, overview images 4 x 4 µm² in size were recorded at a line rate of 20 Hz and a resolution of 2048 x 2048 pixels.

Image processing

The HS-AFM images were flattened using the batch-processing capabilities of the JPK DP Data Processing Software, except the overview images in Figure 20, which were processed using Gwyddion.(*164*) For each experiment, between 795 and 880 HS-AFM images were analyzed, *i.e.*, 4267 images in total.

Statistical analysis

The surface coverage *vs*. time curves in Figure 2a were tested for statistical difference using the Compare Datasets and Fit Parameters App in Origin 2023b (OriginLab) in the dataset setting, applying the pseudo-first order model (*165*). The lattice order obtained for the different concentrations after incubation for about 20 min was tested for statistical differences in Origin 2023b by One Way ANOVA using five $n(\Theta_{60})$ values from the last 50 s of each time series in Figure 19c.

3.2 Cation-dependent Assembly of Hexagonal DNA origami Lattices on SiO_2 Surfaces

3.2.1 Introduction

In the past 15 years, DNA origami(*15*) has transformed the field of DNA nanotechnology and is now a well-established technology used on a daily basis in hundreds of labs around the word.(*166*) The main reasons for this tremendous popularity lie in the precise tunability of the nanoscale shapes and molecular arrangements of the resulting DNA origami nanostructures,(*167, 168*) their straightforward synthesis with high assembly yields,(*169, 16*) and their high mechanical and structural stability under relevant conditions.(*170–172*) Therefore, DNA origami nanostructures are currently employed in many fields of research, including biomedicine,(*173*) sensing,(*174*) electronics,(*175*) and materials science.(*176*)In a materials science context, the possibility to transfer the well-defined shapes of DNA origami nanostructures into organic or inorganic materials is a particularly promising approach toward nanomaterials synthesis.(*177*) DNA assisted lithography (DALI) is a technology that exploits DNA origami nanostructures as lithography masks in the fabrication of precisely shaped metal nanostructures on aluminum oxide or silicon nitride substrates for applications in plasmonics and optical sensing.(*178*) The accessible range of materials combinations has been further extended by biotemplated lithography of inorganic nanostructures (BLIN), which enables the transfer of DNA origami shapes into arbitrary inorganic materials on arbitrary substrates.(*179*) A central step in both of these technologies is the adsorption of the DNA origami nanostructures on an oxidized silicon surface. While DNA origami nanostructures can be adsorbed on various surfaces such as mica,(*15*) gold,(*180*) diamond-like carbon,(*181*) and graphene,(*182*) silicon is chosen because of its compatibility with established semiconductor processing methods such as HF and reactive ion etching.(*183, 184*) So far, DALI and BLIN both have been used to transfer only individual DNA origami shapes randomly placed on the surface. Many relevant applications of these techniques, *e.g.*, the fabrication of photonic crystals or plasmonic metamaterials, however, rather require defined arrangements such as ordered lattices or patterns.

Numerous methods have been explored to direct the adsorption of DNA origami nanostructures into defined arrangements. On SiO_2/Si surfaces, this was achieved using substrates that were pre-patterned with top-down(*181, 185, 186*) or bottom-up(*187–189*) lithographic techniques. As a more straightforward, one-step approach, highly ordered DNA origami lattices can be fabricated on mica surfaces without the need for any pre-patterning simply by controlling their electrostatic interactions with the surface.(*34, 38, 190, 32, 191, 192,*

44) This approach utilizes the competition between monovalent and divalent cations for the DNA-mica interface, which is tuned to a degree that provides the adsorbed DNA origami nanostructures with sufficient mobility to diffuse along the surface and assembly into tightly packed, polycrystalline monolayers.(*43*) In order to create highly ordered lattices in this way, the species and concentrations of the involved monovalent and divalent cation have to be carefully optimized.(*38, 32, 34*) While this enables the homogeneous patterning of wafer-sized substrates at low cost,(*192*) extending it to SiO_2 surfaces is not straightforward because mica and SiO_2 have different zeta potentials and different ion binding properties.(*193, 194*) Additionally, SiO_2 also has a larger root-mean-square surface roughness of about 2 Å compared to about 0.6 Å of muscovite mica.(*195, 196*) Nevertheless, Tapio *et al.* recently achieved highly ordered fishnet-type lattices of cross-shaped DNA origami tiles on oxidized silicon surfaces.(*197*) Compared to DNA origami lattice assembly on mica, the authors had to use much higher concentrations of monovalent cations and elevated substrate temperatures. Furthermore, lattice formation was promoted by blunt-end stacking of the DNA origami tiles.
In this study, we extend the approach of Tapio *et al.*(*197*) to hexagonal DNA origami lattices assembled on SiO_2 surfaces from DNA origami triangles without the aid of blunt-end stacking. A pronouncedly different behavior is observed for this particular system, which does not form ordered lattices under conditions equivalent to those used by Tapio *et al.*, *i.e.*, 12.5 mM Mg^{2+}, 200 – 600 mM Na^{+}, and temperatures between 30 and 40 °C. Our results thus underscore the benefit of attractive interactions between individual DNA origami tiles in the form of blunt-end stacking in the assembly of highly ordered lattices on SiO_2 surfaces. Nevertheless, ordered hexagonal lattices of DNA origami triangles on SiO_2 surfaces are obtained upon replacing Mg^{2+} by Ca^{2+}. Under those conditions, the assembled lattices exhibit a degree of order slightly below that of equivalent lattices assembled on mica surfaces in the presence of Mg^{2+} and Na^{+} ions. Successful transfer of the so-assembled DNA origami lattices into the dry state is demonstrated as well.

3.2.2 Results and Discussion

DNA origami lattice assembly on SiO_2 surfaces was investigated *in situ* by time-lapse atomic force microscopy (AFM) over a time course of about 3.5 hours. The substrates were p-doped Si(100) wafers with hydroxylated surface oxide. Figure 21a shows AFM images recorded in the beginning and at the end of lattice assembly at 20 °C in the presence of 200 mM Na^{+} and 12.5 mM of either Mg^{2+} or Ca^{2+}. It was observed that the presence of Mg^{2+} as the major cation leads to an overlapping of neighboring DNA origami triangles from the very beginning. The results in the formation of a rather disordered monolayer after about 210 min of incubation. The lack of

order is further confirmed by the corresponding fast Fourier transforms (FFTs) of the AFM images in the insets of Figure 21a, which do not show any visible rings. Replacing Mg^{2+} with Ca^{2+} under otherwise identical conditions changes the behavior of the DNA origami triangles on the surface, so that no overlapping is observed anymore in the corresponding AFM images in Figure 21a. Nevertheless, the DNA origami do not assemble into an ordered lattice but rather form a monolayer of randomly oriented triangles. These different behaviors may be explained by the rather high Na^{+} concentration. Both Na^{+} and Mg^{2+} can occupy various binding sites at the phosphate backbone as well as the minor and major grooves of DNA,(*198, 199*) so that their combined presence may induce a local charge inversion of the DNA origami nanostructures and thereby promote DNA origami aggregation. Ca^{2+}, on the other hand, interacts more weakly with nucleic acids(*200–202*) and is more easily replaced by Na^{+} than Mg^{2+}. Therefore, this system shows a reduced propensity for aggregation.

The degree of order of the assembling lattices as a function of time was quantified by calculating the relative correlation length ξ for each AFM image in the two time series, which is a measure of the average domain size (see experimental section).(*38, 203*) The results are plotted in Figure 21b. In both cases, ξ is found to start at a value around 2.5 λ, with λ representing the periodicity of the lattice. Then, ξ decreases with time and reaches a saturation value of around 1.5 λ at about 90 min incubation. The initial decrease stems from the fact that surface coverage starts well below one monolayer and increases only slowly, so that the concept of correlation lengths and domain sizes does not apply yet. Only when a closed monolayer is formed, ξ assumes a stable value and does not increase any further with incubation time. The latter indicates that surface diffusion is insufficient under the applied conditions. On mica surfaces, it was previously observed under optimized assembly conditions that ξ continuously increases with time, which results from the rearrangement of DNA origami triangles and the associated dynamic annealing of lattice defects.(*34, 191, 38*) Nevertheless, it can be seen that surface coverage still increases for prolonged assembly times, indicating that the lattice is far from static at this point and more DNA origami adsorb with time. Unfortunately, this does not result in notable improvements in lattice order. For all time points, slightly higher ξ values are obtained in the presence of Ca^{2+}, which indicates a slightly higher surface mobility of the adsorbed DNA origami nanostructures, similar to what was previously observed on mica.(*34*)

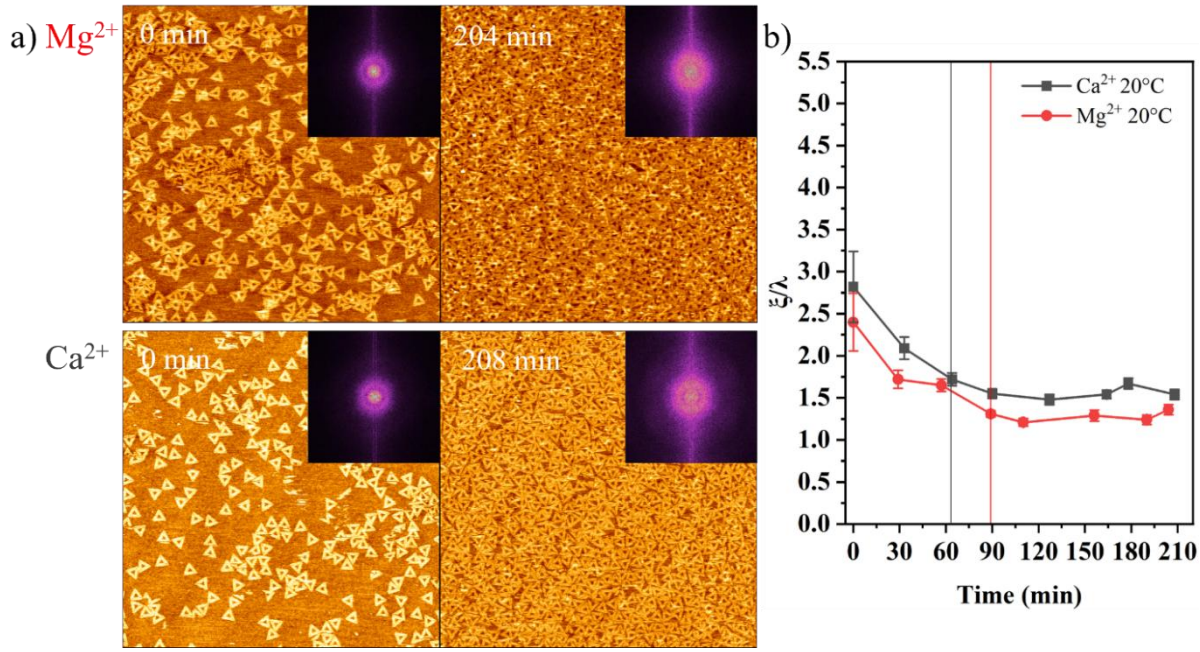

Figure 21: a) AFM images (3 x 3 µm²) recorded at time points 0 (left) and ~ 210 min (right) at 20 °C, 200 mM Na+, and 12.5 mM of either Mg^{2+} or Ca^{2+}, respectively. Insets show the fast Fourier transforms (FFTs). b) Relative correlation lengths ξ/λ as calculated from all recorded AFM images as a function of incubation time. The vertical lines in b) indicate the time points at which closed monolayers are observed.

Building on previous experience with DNA origami lattice assembly on mica surfaces,(*38*) the concentration of Na^+ was increased to 400 mM in order to increase the surface mobility of the adsorbed DNA origami nanostructures. As can be seen in Figure 22a, this increase in the Na^+ concentration did not result in any improvements in lattice order. In the presence of Mg^{2+}, the overlapping of the DNA origami triangles in the monolayer seems to have gotten worse, which agrees with the above interpretation of the combination of high Na^+ and moderate Mg^{2+} concentrations promoting DNA origami aggregation. In the case of Ca^{2+} as the divalent cation, the obtained lattice is still rather unordered with the corresponding FFT not showing any discernable ring structure. The most remarkable difference compared to 200 mM Na^+ is a delay in the decrease of the correlation lengths (see Figure 21b and Figure 22b). This results from DNA origami adsorption at the SiO_2 surface being slowed down by the higher Na^+ concentration, presumably because of the screening of electrostatic interactions at the DNA-SiO_2 interface.

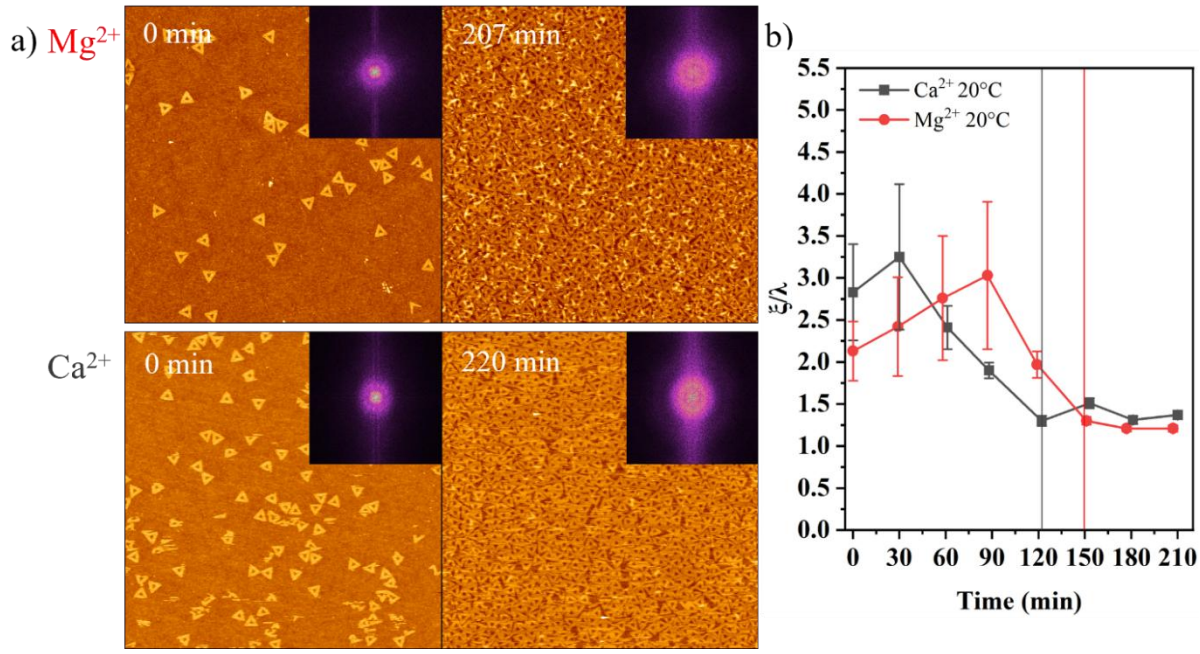

Figure 22: a) AFM images (3 x 3 µm²) recorded at time points (left) and ~ 210 min (right) at 20 °C, 400 mM Na^+, and 12.5 mM of either Mg^{2+} or Ca^{2+}, respectively. Insets show the fast Fourier transforms (FFTs). b) Relative correlation lengths ξ/λ as calculated from all recorded AFM images as a function of incubation time. The vertical lines in b) indicate the time points at which closed monolayers are observed.

Increasing the Na^+ concentration further to 600 mM did not result in dramatic changes in the assembly and the quality of the DNA origami monolayer in the presence of Mg^{2+} (see Figure 23). In the case of Ca^{2+} as the divalent cation, however, the FFT of the AFM image obtained after about 210 min incubations shows weak ring structures (see Figure 23a), indicating a slight improvement in lattice order. This is further verified in the evolution of the correlation length ξ in Figure 23b, which from the point of monolayer formation shows larger values between 2 and 2.5 λ, consistent with slightly improved order. This is most likely a result of enhanced surface diffusion allowing the DNA origami lattices to optimize their arrangement within the lattice and thus enables them to form larger domains. As can further be seen in Figure 23b, the correlation length of this system shows somewhat erratic behavior with sudden jumps to higher or lower values. This behavior was attributed to the enhanced surface mobility of the DNA origami nanostructures, which leads to a large number of adsorption and desorption events and thus highly dynamic behavior.

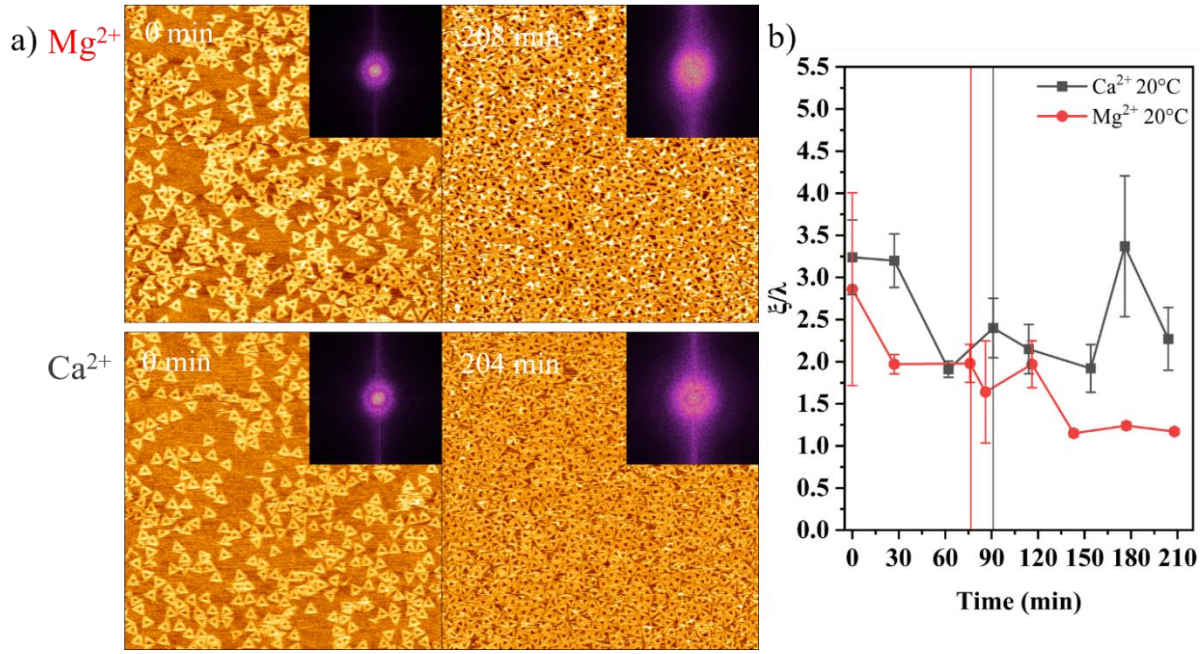

Figure 23: a) AFM images (3 x 3 µm²) recorded at time points 0 (left) and ~ 210 min (right) at 20 °C, 600 mM Na^+, and 12.5 mM of either Mg^{2+} or Ca^{2+}, respectively. Insets show the fast Fourier transforms (FFTs). b) Relative correlation lengths ξ/λ as calculated from all recorded AFM images as a function of incubation time. The vertical lines in b) indicate the time points at which closed monolayers are observed.

While an increase of the Na^+ concentration to 600 mM has resulted in a slightly increased order of the assembled DNA origami lattice, the corresponding AFM image in Figure 23a shows also the first signs of DNA origami aggregation and multilayer formation (bright spots). Therefore, a further increase in Na^+ concentration beyond 600 mM does not appear promising. Rather, in the next set of experiments, we have increased the substrate temperature from 20 to 30 °C. In the recent work of Tapio *et al.*, an elevated substrate temperature of about 30 to 40 °C was essential for obtaining large and well- formed DNA origami lattices on SiO_2 surfaces mediated by blunt-end stacking.(*197*) As can be seen in Figure 24, this moderate increase in temperature did not result in any notable improvement at a Na^+ concentration of 200 mM, with the correlation lengths of both the Mg^{2+} and the Ca^{2+} systems remaining below 2 λ. This indicates that the surface mobility of the DNA origami nanostructure under these conditions was still too low. Therefore, higher Na^+ concentrations was also evaluated, which had shown slightly better results at 20 °C.

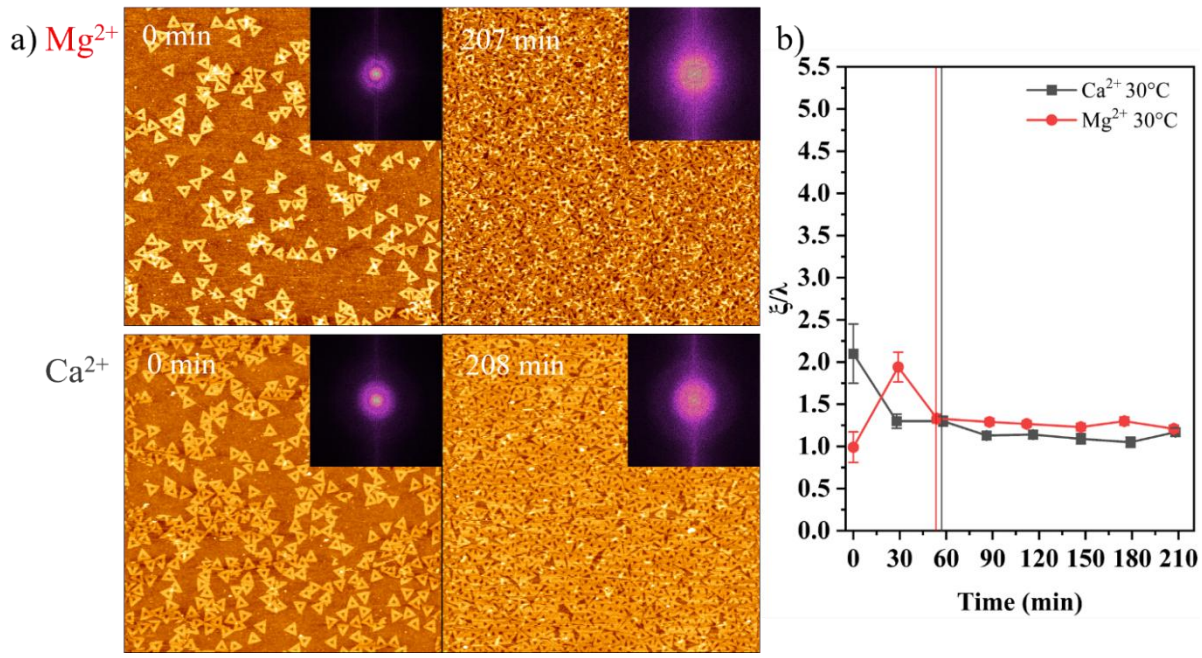

Figure 24: a) AFM images (3 x 3 µm²) recorded at time points (left) and ~ 210 min (right) at 30 °C, 200 mM Na^+, and 12.5 mM of either Mg^{2+} or Ca^{2+}, respectively. Insets show the fast Fourier transforms (FFTs). b) Relative correlation lengths ξ/λ as calculated from all recorded AFM images as a function of incubation time. The vertical lines in b) indicate the time points at which closed monolayers are observed.

At 400 mM Na^+ concentration, Figure 25 indeed reveals some improvement. While the monolayer formed in the presence of Mg^{2+} is still characterized by low order and multilayer buildup, the presence of Ca^{2+} facilitates the assembly of a DNA origami lattice with increased quality and order. In particular, the FFT shown in the insets of the corresponding AFM images in Figure 5a develops a weak ring structure over time. At the same time, also the correlation length is increasing with time – albeit with strong fluctuations – and reaches a final value of about 2.5 λ at about 210 min. For comparison, under otherwise identical conditions at 20 °C substrate temperature, ξ remains below 1.5 λ (see Figure 23b).

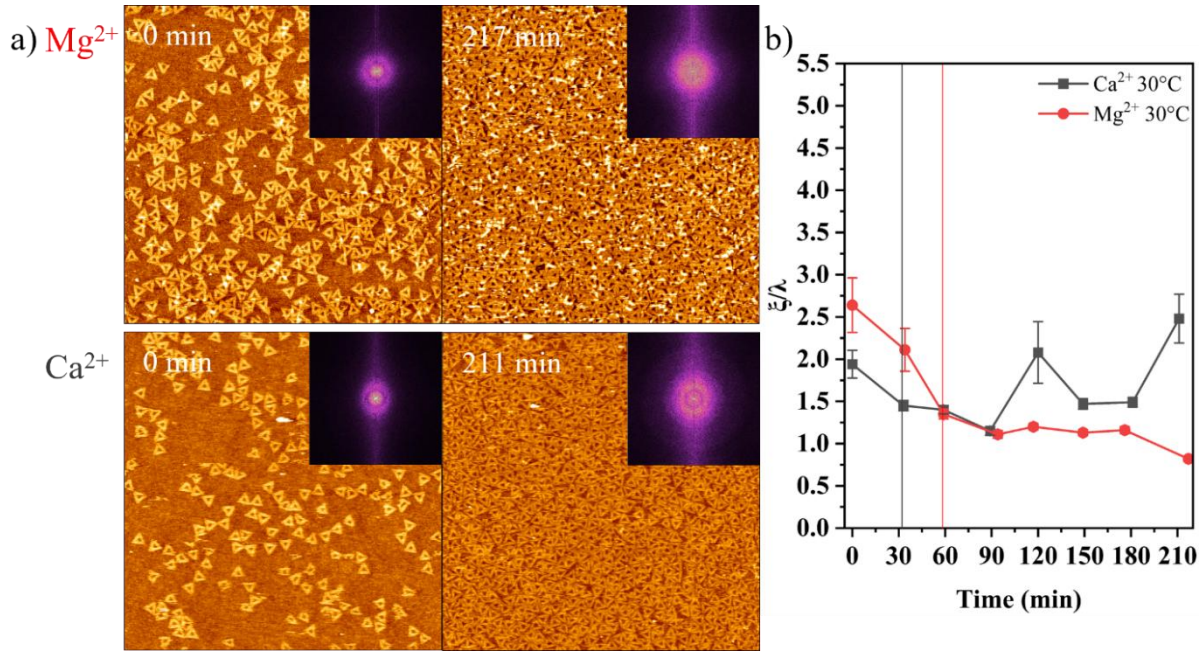

Figure 25: a) AFM images (3 x 3 µm²) recorded at time points (left) and ~ 210 min (right) at 30 °C, 400 mM Na^+, and 12.5 mM of either Mg^{2+} or Ca^{2+}, respectively. Insets show the fast Fourier transforms (FFTs). b) Relative correlation lengths ξ/λ as calculated from all recorded AFM images as a function of incubation time. The vertical lines in b) indicate the time points at which closed monolayers are observed.

Increasing the Na^+ concentration to 600 mM at 30 °C substrate temperature leads to further improvement. For Ca^{2+}, Figure 26a shows the formation of a rather well-ordered DNA origami lattice. Despite a considerable number of lattice defects, the corresponding FFT has the form of a well-defined ring with vaguely hexagonal shape. This enhanced lattice order is also reflected in the correlation length (Figure 26b), which further increases to about 3.5 λ after about 210 min incubation. While this is a rather pronounced improvement compared to the lower temperatures and Na^+ concentrations, the obtained correlation length is still lower than those achieved on mica surfaces under optimized conditions, which routinely reach values of about 5 λ but may go as high as about 8 λ.(*34, 38*) However, it was seen that ξ has not yet saturated at this time point but is still increasing, so that even higher values may be achievable at longer incubation times. Interestingly, the combination of elevated substrate temperature and high Na^+ concentration also leads to small improvements in the Mg^{2+} system. Here, ξ values between 1.5 and 2 are obtained, which is further proof of thermally enhanced surface diffusion. Nevertheless, lattice assembly is still hindered by multilayer formation (see corresponding AFM image in Figure 26a).

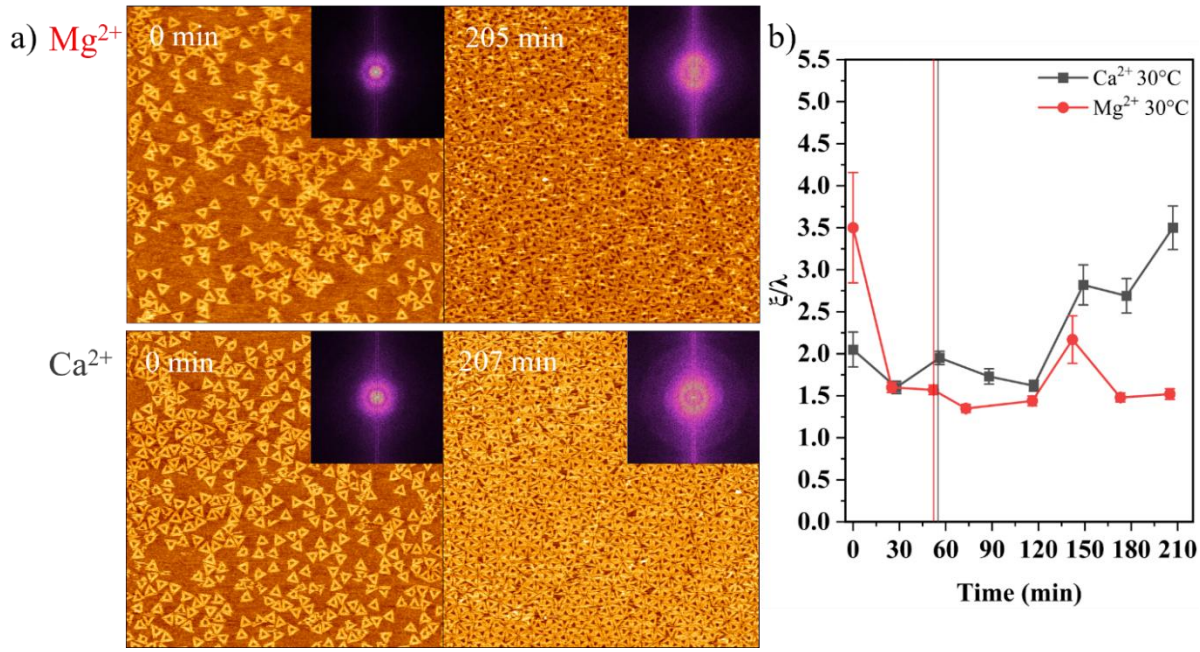

Figure 26: a) AFM images (3 x 3 µm²) recorded at time points 0 (left) and ~ 210 min (right) at 30 °C, 600 mM Na^+, and 12.5 mM of either Mg^{2+} or Ca^{2+}, respectively. Insets show the fast Fourier transforms (FFTs). b) Relative correlation lengths ξ/λ as calculated from all recorded AFM images as a function of incubation time. The vertical lines in b) indicate the time points at which closed monolayers are observed.

Finally, the substrate temperature was increased further to 40 °C. At 200 mM Na^+, this further increase does not have any positive effect on lattice assembly (see Figure 27). On the contrary, under these conditions, the AFM images in Figure 27a show two distinct differences compared to all previous experiments. First, an exceptionally high surface coverage is observed at the very beginning of the experiment. While this may to some extent be related to a small delay between the injection of the DNA origami sample into the liquid cell and the start of the first AFM scan, it may also be a result of the increased diffusion of the DNA origami in the bulk solution. Since our experimental setting is diffusion limited, such an increased bulk diffusion will lead to higher arrival rate of the DNA origami at the surface and thereby to increased adsorption. The latter interpretation was further supported by the second observation, *i.e.*, rather strong multilayer formation not only in the presence of Mg^{2+} but also for Ca^{2+}, which was not seen in the above experiments.

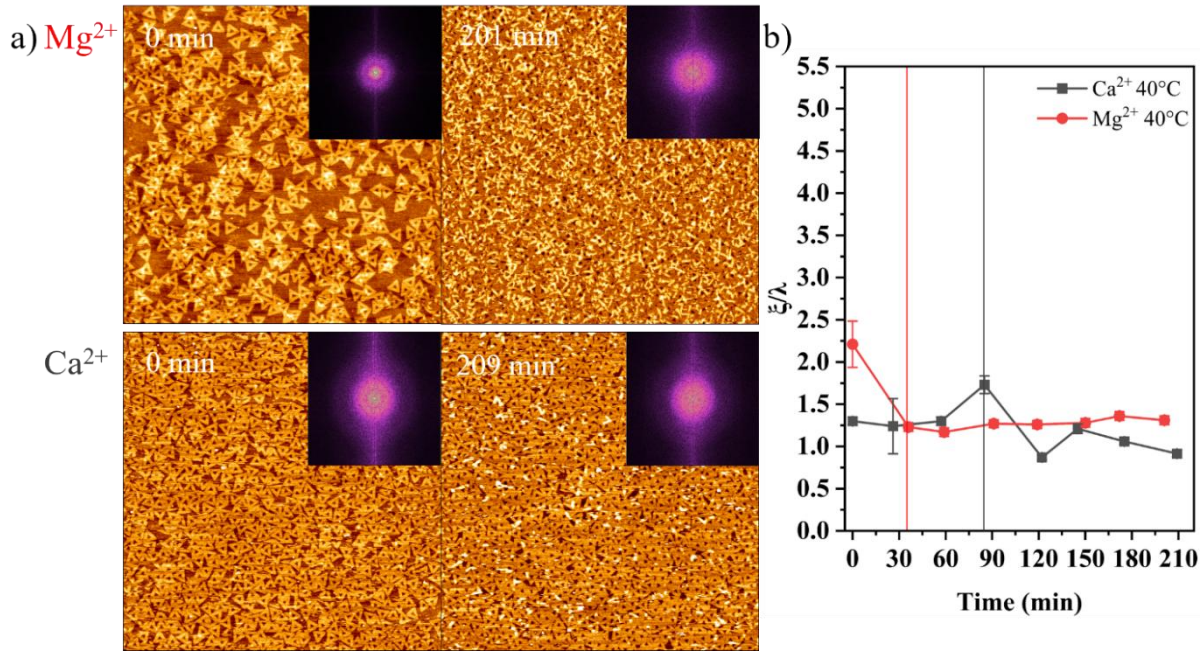

Figure 27: a) AFM images (3 x 3 µm²) recorded at time points 0 (left) and ~ 210 min (right) at 40 °C, 200 mM Na^+, and 12.5 mM of either Mg^{2+} or Ca^{2+}, respectively. Insets show the fast Fourier transforms (FFTs). b) Relative correlation lengths ξ/λ as calculated from all recorded AFM images as a function of incubation time. The vertical lines in b) indicate the time points at which closed monolayers are observed.

Both effects of the increased temperature, *i.e.*, high surface coverage and multilayer formation in the presence of Ca^{2+}, are markedly reduced at 400 mM Na^+ (see Figure 28a). This indicates that the increased Na^+ concentrations drastically enhances the surface mobility, and particularly the desorption rate of the DNA origami, which now counterbalances the increased adsorption rate. The dramatically enhanced surface mobility in the presence of Ca^{2+} could directly been seen in the initial AFM image recorded at 0 min incubation in Figure 28a. Here, the DNA origami triangles have a rather blurry appearance because of their rapid motion along the surface. A similar observation was made also on mica at room temperature in the presence of 75 mM Na^+ and 10 mM Ca^{2+},(*34*) which was a further indication of the comparably low surface mobility of the DNA origami nanostructures on the SiO_2 surface. As one would expect, the enhanced surface mobility also leads to improved lattice order as demonstrated by the corresponding FFT in Figure 28a, which shows a clear ring structure with notably hexagonal shape. Furthermore, as can be seen in Figure 28b, the correlation length of the lattice assembled in the presence of Ca^{2+} reaches a value of about 4.5 λ already after 120 min incubation, after which it fluctuates between 4.5 and 3.0 λ. These rather strong fluctuations could be attributed to the strong dynamics of the lattice, which is characterized not just by lateral diffusion of the adsorbed DNA origami along the surface but also many desorption and adsorption events. For this condition, it was observed that the largest increase in surface

coverage during assembly, *i.e.*, from about 73% upon formation of a closed monolayer to about 88% at the end of incubation.

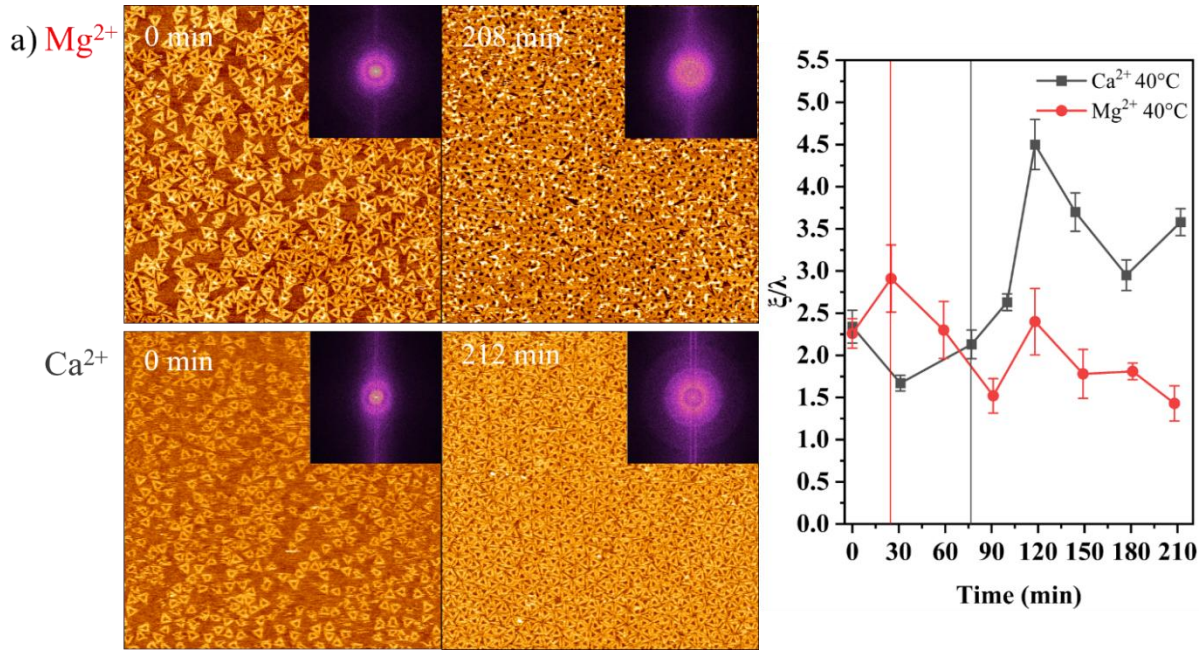

Figure 28: a) AFM images (3 x 3 µm²) recorded at time points 0 (left) and ~ 210 min (right) at 40 °C, 400 mM Na^+, and 12.5 mM of either Mg^{2+} or Ca^{2+}, respectively. Insets show the fast Fourier transforms (FFTs). b) Relative correlation lengths ξ/λ as calculated from all recorded AFM images as a function of incubation time. The vertical lines in b) indicate the time points at which closed monolayers are observed.

Similar behavior can also be observed in Figure 29 at a higher Na^+ concentration of 600 mM. Here, however, an even higher surface mobility leads to stronger dynamics, which in turn delays the increase in ξ. Only after about 210 min, ξ reaches a value of about 4 λ and the corresponding FFT in Figure 29a is less defined than the corresponding one observed at 400 mM (see Figure 28a). The strongly increased surface mobility is also apparent in the presence of Mg^{2+}, where the formed lattice reaches a maximum ξ value of almost 3 λ. However, this system still suffers from multilayer formation.

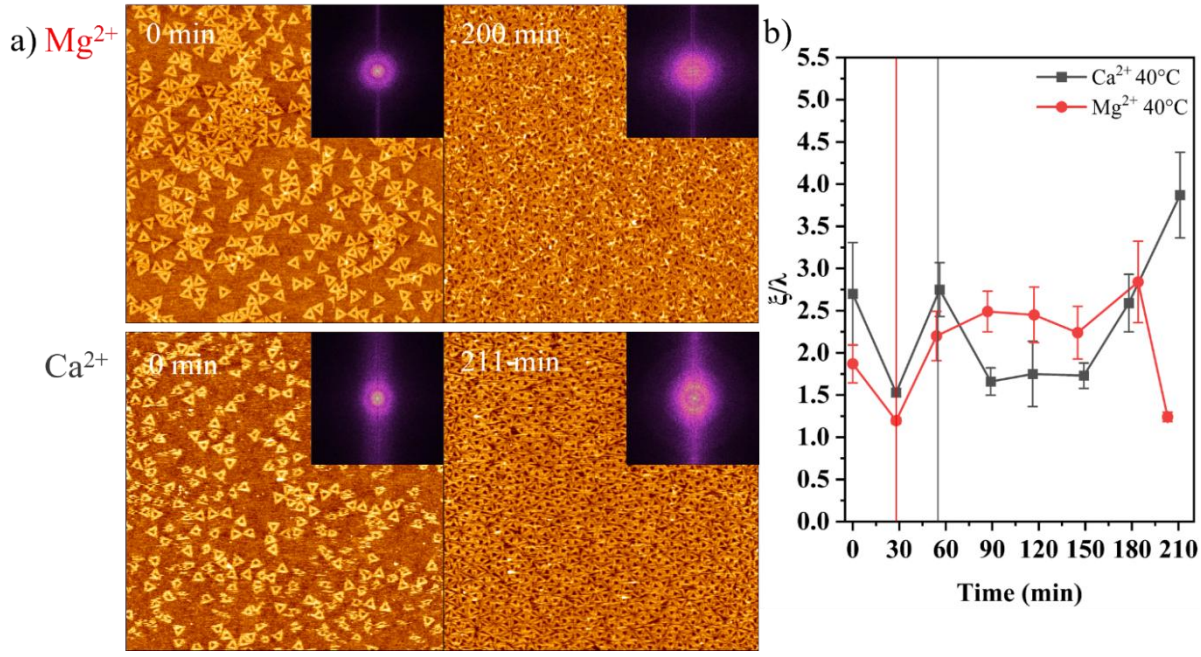

Figure 29: a) AFM images (3 x 3 µm²) recorded at time points 0 (left) and ~ 210 min (right) at 40 °C, 600 mM Na^+, and 12.5 mM of either Mg^{2+} or Ca^{2+}, respectively. Insets show the fast Fourier transforms (FFTs). b) Relative correlation lengths ξ/λ as calculated from all recorded AFM images as a function of incubation time. The vertical lines in b) indicate the time points at which closed monolayers are observed.

In Figure 30, the correlation lengths of the different lattices obtained after incubation for about 210 min under the tested conditions are compared. It is observed that increasing either the substrate temperature or the Na^+ concentration leads to increased lattice order. Furthermore, there is an apparent interdependency of these two parameters, i.e., essentially the same degree of order that is achieved at 40 °C with 400 mM Na^+ can also be obtained at a lower temperature of 30 °C if the Na^+ concentration is increased to 600 mM. This implies that the Na^+ concentration essentially acts as an effective temperature with higher concentrations leading to increased DNA origami mobility. This confirms previous postulations for DNA origami lattice assembly on mica surfaces.(*38*) Finally, all these trends were much more pronounced for Ca^{2+} than for Mg^{2+} as the divalent cation.

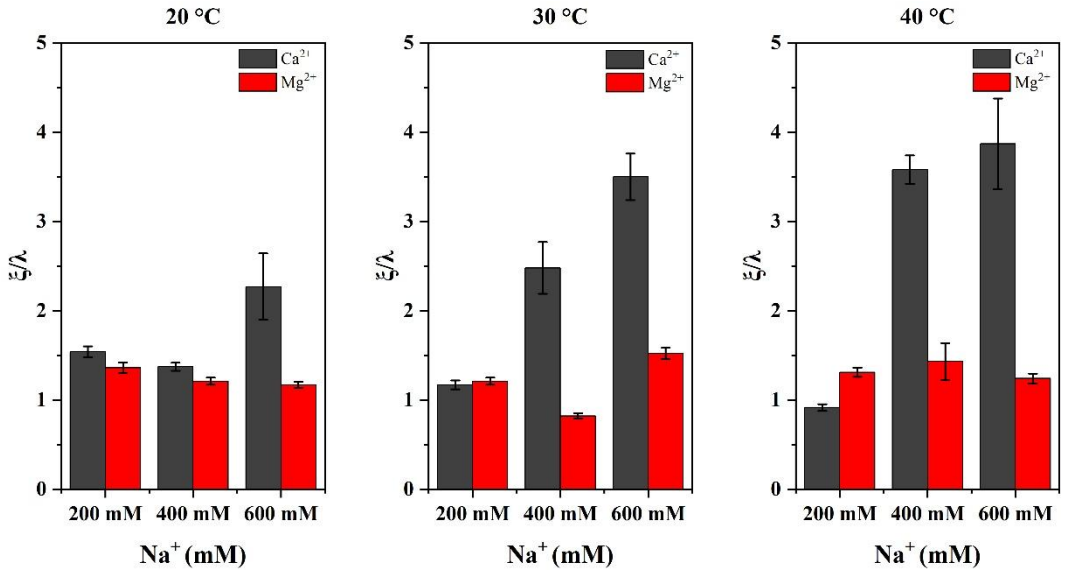

Figure 30: Comparison of the relative correlation lengths ξ/λ of the different lattices obtained in the presence of Mg^{2+} and Ca^{2+}, respectively, after about 210 min incubation.

However, even under optimized conditions, the obtained lattices have a much lower degree of order than on mica. For instance, incubation of 3 nM DNA origami triangles in 10 mM Ca^{2+} and 75 mM Na^+ on mica for 90 min at room temperature resulted in a highly ordered lattice with a correlation length ξ > 8 λ.(*34*) While this may not be surprising considering the different surface properties of mica and SiO_2, even higher correlation lengths were obtained for tetragonal DNA origami lattices assembled on similar SiO_2 surfaces and under similar environmental conditions as used here.(*197*) This was because the lattices of Tapio *et al.* were assembled from Seeman tiles, which are able to participate in blunt-end stacking with neighboring tiles. This additional attractive intermolecular interaction appears to be crucial for obtaining highly ordered lattices on SiO_2 surfaces because it lowers the mobility of DNA origami nanostructures incorporated into a growing lattice. For the DNA origami triangles studied here, the limiting factor appears to be the high desorption rate that accompanies a high lateral mobility of adsorbed DNA origami nanostructures along the SiO_2 surface. At the high temperatures and Na^+ concentrations required for sufficient lateral mobility, continuous DNA origami desorption from lattice sites prevents the lattice from approaching a low-energy state with optimized packing density. In the presence of blunt-end stacking, however, DNA origami monomers have a higher surface mobility and desorption rate than dimers and multimers. Lattice assembly under such conditions thus resembles a nucleated crystal growth mechanism and leads to much larger single-crystalline lattice domains.

Finally, an attempt was made to transfer the DNA origami lattices assembled on the SiO_2 surface in the presence of Ca^{2+} into the dry state, in order to enable further processing steps such as growth of an oxide mask by chemical vapor deposition.(*184, 178, 204, 179*) For DNA

origami lattices assembled on mica and SiO_2 in the presence of Mg^{2+}, such a transfer was achieved previously by addition of Ni^{2+} either directly to the sample solution after lattice assembly or after gentle washing of the substrate surface to remove free DNA origami.(*192*) Ni^{2+} has a higher affinity for DNA than Mg^{2+} and Na^{+} and thereby efficiently fixates the DNA origami nanostructures to the surface. For the current hexagonal lattices assembled on SiO_2 in the presence of Ca^{2+}, however, a more gentle approach was required. While the simple addition of Ni^{2+} to the DNA origami-containing solution after lattice assembly ensured that the formed lattice remained essentially intact during subsequent washing, it also resulted in the random adsorption of a large amount of DNA origami triangles from solution. This is a general issue frequently observed upon lattice transfer into the dry state(*192, 197, 44*) and may be reduced to some extent by additional fine-tuning of environmental parameters.(*197*) In the present case, it was found that cooling the substrate to 4°C before the addition of Ni^{2+} led to less pronounced DNA origami deposition, probably due to the reduced diffusion of the free DNA origami nanostructures suspended in the bulk solution. Figure 31 shows an AFM image of the resulting lattice in the dry state. As can be seen, DNA origami deposition is not fully suppressed and there are still some triangles from solution adsorbed on top of the lattice. Reducing the DNA origami concentration from 4 nM to 3 nM did not result in a notable difference. In an attempt to completely suppress DNA origami deposition, we also tried to carefully remove the DNA origami-containing solution from the substrate surface before addition of Ni^{2+}. However, this destroyed the assembled lattice because of the high mobility of the DNA origami nanostructures within the lattice. Despite the remaining DNA origami triangles adsorbed on top of the lattice, the image in Figure 31 demonstrates the possibility of transferring the DNA origami lattice assembled on the SiO_2 surface in the presence of Ca^{2+} into the dry state, which is an important prerequisite for further processing steps.

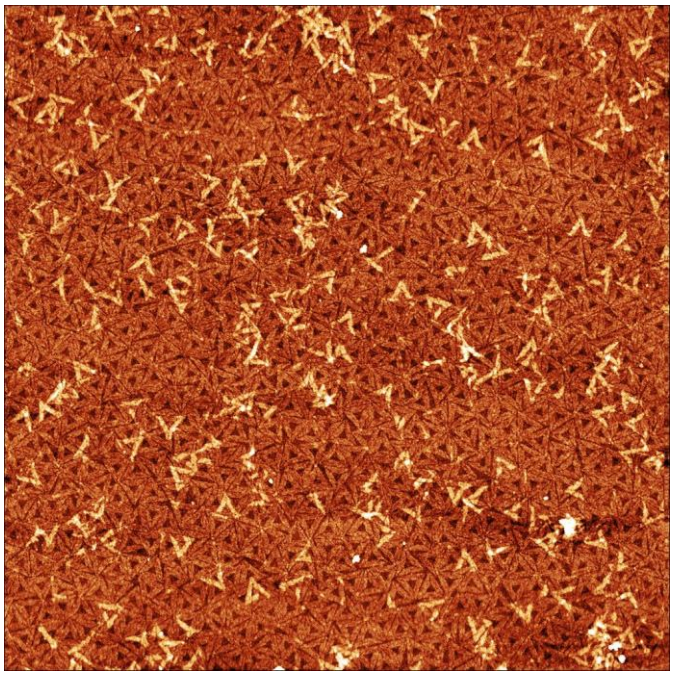

Figure 31: AFM image (3 x 3 µm²) of a DNA origami lattice assembled at 40 °C in the presence of 400 mM NaCl and 12.5 mM $CaCl_2$ after transfer into the dry state.

3.2.3 Conclusion

In summary, the effects of Mg^{2+} and Ca^{2+} on the assembly of hexagonal DNA origami lattices on RCA-cleaned silicon surfaces in the absence of attractive intermolecular interactions were investigated. Lattice assembly was monitored by time-lapse AFM in dependence of Na^+ concentration and substrate temperature. Remarkably, in the presence of Mg^{2+}, no ordered lattices were obtained, instead the formation of disordered multilayers was observed under all the conditions tested. This is most likely related to a partial charge inversion of the DNA origami triangles in the presence of Mg^{2+} and large concentrations of Na^+. In the presence of Ca^{2+}, on the other hand, assembly of ordered lattices was achieved at substrate temperatures of 30 – 40 °C and Na^+ concentrations of 400 to 600 mM. This is attributed to the general weaker binding of Ca^{2+} to DNA so that it is easier to replace by Na^+, which provides the adsorbed DNA origami nanostructures with enhanced surface mobility. Unfortunately, this enhanced surface mobility was accompanied by an increased desorption rate, which appears to limit the maximum degree of lattice order that can be achieved in this way, so that the correlation length of the hexagonal lattices assembled in this work on hydroxyl-rich silicon oxide surfaces is only about half that of equivalent lattices assembled previously on mica surfaces.(*38, 34*)
In the recent work by Tapio *et al.*,(*197*) highly ordered tetragonal DNA origami lattices were obtained on SiO_2 surfaces under similar conditions as employed here. Comparison with our results suggests that such high degrees of order requires attractive intermolecular interactions such as blunt-end stacking to minimize DNA origami desorption after incorporation into the

growing lattice. It should be mentioned, however, that Tapio *et al.* had assembled their lattices in the presence of Mg^{2+}, which in our experiments resulted only in low degrees of order and multilayer formation. This suggests that the shape of the DNA origami nanostructures plays a role as well. Indeed, Tapio *et al*. reported that large and well-ordered lattices could be obtained only from twist-corrected Seeman tiles whereas non-twist corrected nanostructures formed only unordered monolayers. While this was attributed to shape distortions of the non-twist corrected Seeman tiles preventing proper blunt-end stacking, our experiments with the non-twist corrected and thus strongly distorted triangles(*205*) may indicate that such factors may also affect the general surface mobility, the desorption rate, and the aggregation propensity of the DNA origami nanostructures.

Compared to mica surfaces, it appears that DNA origami lattice formation on hydroxylated SiO_2 surfaces is more sensitive toward environmental parameters. Based on our results, the order of DNA origami lattices assembled on SiO_2 surfaces may be further enhanced in the future by two general strategies. First, since DNA origami adsorption at electrolyte/SiO_2 interfaces involves electrostatic interactions, tuning the charge density of the surface may be used to control the interaction strength. This may be achieved for instance by adjusting the pH in solution or by surface modification approaches such as ion implantation.(*206*) However, it should also be mentioned that the hydroxyl density and surface energy of SiO_2 surfaces depends strongly on the nature and history of the substrates,(*207*) including any applied surface cleaning procedures.(*208*) Alternatively, complex temperature profiles may be applied during lattice assembly as they are used for instance in the growth of inorganic mixed crystals(*209, 210*) in order to enable a slow crystallization with gradual immobilization of DNA origami nanostructures on lattice sites. Even though exploring all these parameters in a systematic way may turn out rather time consuming and be further complicated by non-trivial interdependencies, it may lead to optimized protocols for the reproducible fabrication of DNA origami-based molecular lithography masks on silicon wafers fully compatible with established microfabrication techniques.

3.2.4 Materials and Methods

DNA origami assembly and purification

The DNA origami triangles(*15*) were prepared using the 7249 nt M13mp18 scaffold (Tilibit) and 208 staples strands (Eurofins). Staples and scaffold were mixed at tenfold staple excess in 1x TAE (Carl Roth) supplemented with 10 mM $MgCl_2$ (Carl Roth). The solution was heated to 80 °C in a thermocycler (Primus 25 Advanced, PEQLAB) and subsequently cooled down to room temperature over a time span of 90 min. The assembled DNA origami nanostructures were

spin filtered to remove the excess unbound staples (Amicon Ultra 100K, Millipore). The molar concentration of the synthesized DNA origami nanostructures was estimated by UV/Vis absorption using a nanophotometer (Implen Nanophotometer P330)

Substrate preparation

Commercial epi-ready p-doped Si(100) wafers (root-mean-square surface roughness ~ 2.6 Å, Siegert Wafer) were cut into 2 x 2 cm² pieces and cleaned in RCA-1 solution (1:1:5 35% H_2O_2, 25% NH_3, H_20) for 15 min at 75 °C to remove the organic residues and create a hydrophilic hydroxyl-rich surface.(*208*)

Time-lapse AFM

Time-lapse AFM was performed using a JPK Nanowizard ULTRA Speed with USC F0.3-k0.3 cantilevers (NanoWorld). 4 nM DNA origami nanostructures were suspended in 1x TAE (pH 8.5) containing 12.5 mM $MgCl_2$ (Carl Roth) or $CaCl_2$ (Merck) and varying concentrations of NaCl (VWR). The silicon substrate was placed in a liquid cell (JPK) with a temperature-controlled stage (JPK), after which the cell was manually filled with 1 ml sample solution. The first AFM images (indicated as time point 0 min in Figures 21-29) were recorded after 1 to 8 min after filling the liquid cell. AFM images were recorded with 3 x 3 µm² scan size at a line rate of 10 Hz and a resolution of 512 x 512 pixels resulting in 51.2 s per frame. The measurements were carried out over a period of approximately 210 min, during which sets of 8 images were recorded at different time points.

Transfer into the dry state

The freshly cleaned silicon wafer was placed in a custom-built liquid cell. The liquid cell in turn was placed inside a Petri dish containing an open reservoir filled with 10 ml of water. 500 µl of 1x TAE containing 400 mM NaCl, 12.5 mM $CaCl_2$, and 3 nM or 4 nM DNA origami triangles were added to the liquid cell to immerse the silicon wafer. The Petri dish was covered with a lid, placed in an incubator (INCU-Line, VWR), and incubated for 3.5 h at 40 °C. After incubation, the liquid cell was taken out of the incubator and placed on ice. After 15 min, 25 µL of 50 mM $NiCl_2$ solution was added to the Petri solution in the liquid cell, resulting in a final Ni^{2+} concentration of 2.38 mM. After another 15 min of incubation, the sample was removed from the liquid cell, washed with 12 ml of HPLC grade water, and dried in a stream of argon.

AFM imaging of dried lattices

The dry samples were imaged in air using a Bruker Dimension ICON in ScanAsyst Peak-Force Tapping mode with ScanAsyst Air cantilevers (Bruker). Images were recorded with 1024 x 1024 pixels at a scan size of 3 x 3 µm².

Image processing

The images were processed using the open-source software Gwyddion(*211*) to calculate the FFTs and the radial power spectral density functions. The latter were plotted using OriginPro 2022 and the first correlation peak fitted with a Lorentzian to determine its full-width at half-maximum (fwhm). The so determined fwhm was then used to calculate the correlation length of the lattice.(*38, 191, 34, 203*)

3.3 DNA Origami Adsorption and Lattice Formation on Different SiO_x Surfaces

3.3.1 Introduction

The past few years have seen increasing interest in the hierarchical self-assembly of DNA origami nanostructures into ordered lattices.(*43, 212*) This interest is motivated mainly by promising applications of the resulting lattices in synthetic biology(*213–216*) and materials science.(*217–223*) In contrast to biological applications that often rely on the functionality of the assembled DNA origami nanostructures themselves, applications in materials science usually employ the DNA origami nanostructures only as templates for the synthesis or assembly of functional inorganic nanostructures.(*217, 219–223, 46*) This can be achieved by a variety of techniques such as sol-gel silicification(*219, 221–223*) or the binding of colloidal nanoparticles.(*217, 220, 46*) Molecular lithography approaches are particularly appealing for the fabrication of functional 2D surfaces because they are based on well-established nanofabrication methods and thus not only highly versatile but also compatible with large-scale, high-throughput production.(*224–226*) While being powerful in producing functional surfaces for plasmonic and sensing applications,(*225, 227, 228*) these molecular lithography approaches so far utilized only disperse DNA origami nanostructures randomly adsorbed at the substrate surface. This is because large-area DNA origami lattices traditionally were fabricated only on mica surfaces,(*229*) whereas molecular lithography relies on silicon processing technology. Recently, however, the surface-assisted assembly of DNA origami nanostructures into large and well-ordered lattices was demonstrated on oxidized silicon wafers,(*156, 33*) thereby paving the way toward the molecular lithography-based fabrication of ordered arrays of arbitrarily shaped inorganic nanostructures.

Compared to surface-assisted DNA origami assembly on mica, lattice assembly on SiO_2 surfaces was found to be more sensitive toward environmental factors and especially the ionic composition of the electrolyte and the substrate temperature.(*156, 33*) This is mostly because SiO_2 surfaces have a lower zeta potential than mica(*230, 231*) and a larger root-mean-square (rms) surface roughness.(*232, 233*) Additionally, however, it is well established that the hydroxylation state and surface energy of SiO_2 surfaces depend critically on the type and history of the specimen, including the fabrication method and the storage conditions.(*234–239*)

While many previous studies adsorbed DNA origami nanostructures on SiO_2 surfaces, the vast majority used silicon wafers with native surface oxide.(*156, 33, 240–242, 187, 243–246*) It is thus unclear whether the reported protocols for DNA origami adsorption and lattice assembly on this type of surface can also be applied to other silicon oxide surfaces. Therefore, in this work, we investigate DNA origami adsorption and lattice formation on different SiO_x surfaces fabricated by thermal oxidation, magnetron sputter deposition (MSD), and plasma-enhanced chemical vapor deposition (PE-CVD). All

SiO_x surfaces were wet-chemically oxidized and hydroxylated by RCA1 directly before the experiments,(*156*) and thus had similar hydroxylation states as indicated by X-ray photoelectron spectroscopy (XPS). Nevertheless, dramatic differences in DNA origami adsorption and lattice assembly are observed. Of all surfaces tested, only the thermally grown SiOx film yields results comparable to the native surface oxide. On all other surfaces, DNA origami adsorption is notably reduced, with the SiO_x surfaces fabricated by PE-CVD barely adsorbing any DNA origami nanostructures at all. While the latter can be attributed to the higher surface roughness of the PE-CVD films, strongly reduced DNA origami surface coverage is observed also for the MSD films with surface roughness values comparable to that of the native surface oxide. XPS reveals minor variations in the oxide composition of the different surfaces, which, however, do not correlate with the observed differences in DNA origami adsorption. Rather, we attribute the observed differences in DNA origami adsorption to differences in oxide density, with efficient DNA origami lattice assembly on SiO_x surfaces requiring a high oxide density in addition to a low surface roughness. Our results thus demonstrate that the employed SiO_x surface should be considered as an additional and important parameter that may require tuning and optimization before high-quality lattices can be assembled.

3.3.2 Results and Discussion

Surface Characterization

Six different silicon oxide surfaces on identical silicon wafers were investigated with the native surface oxide (1.4 nm) of the silicon wafer (N) being used as the benchmark. A 30 nm thermal oxide film (T) was grown by thermal oxidation at 1200 °C in air. SiOx films of 18 nm and 11 nm thickness were deposited by MSD with (MB) and without (M) a bias voltage of -20 V applied to the substrate, respectively. Application of a negative bias to the substrate during MSD increases ion bombardment during growth and typically results in denser and more compact films.(*233, 247*) 20 nm SiO_x (PO) and 17 nm SiOCH films (PC) were deposited by PE-CVD using different mixtures of argon and oxygen gas and HMDSO vapor. All surfaces were wet-chemically oxidized and hydroxylated by RCA1 treatment and subsequently imaged by atomic force microscopy (AFM). As can be seen in Figure 32, all surfaces have a smooth topography without any pronounced texture. However, the surfaces fabricated by PE-CVD, *i.e.*, PC and especially PO, appear to have a larger surface roughness. This is confirmed by the rms surface roughness S_q, which has been calculated from the AFM images and is given for all six surfaces in Figure 33. While the native, thermal, and MSD oxide surfaces all have S_q values between 2 and 3 Å, the S_q of surface PC is increased to almost 5 Å. Surface PO has an even higher S_q of more than 8 Å.

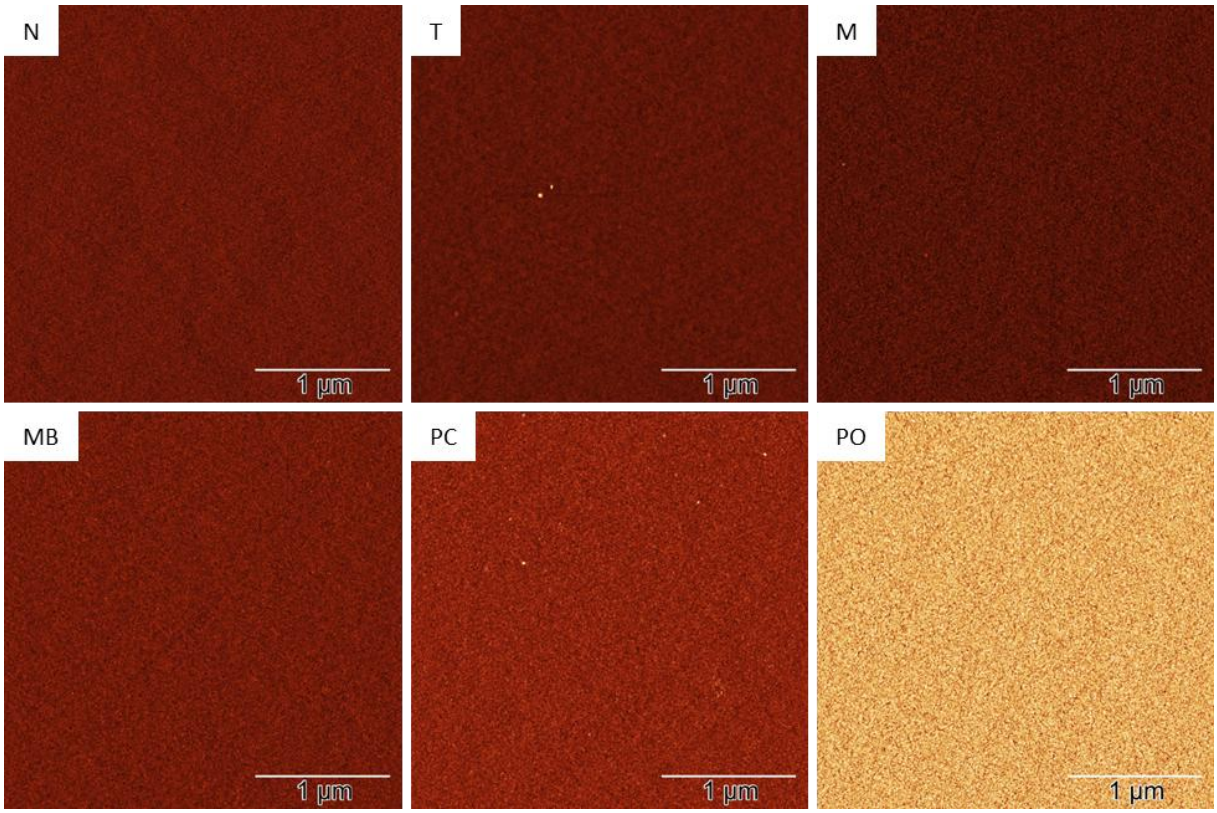

Figure 32: AFM images of the different SiO_x surfaces after wet-chemical oxidation by RCA1. Height scales are 6 nm for all images. See Figures S3 – S8 for additional AFM images.

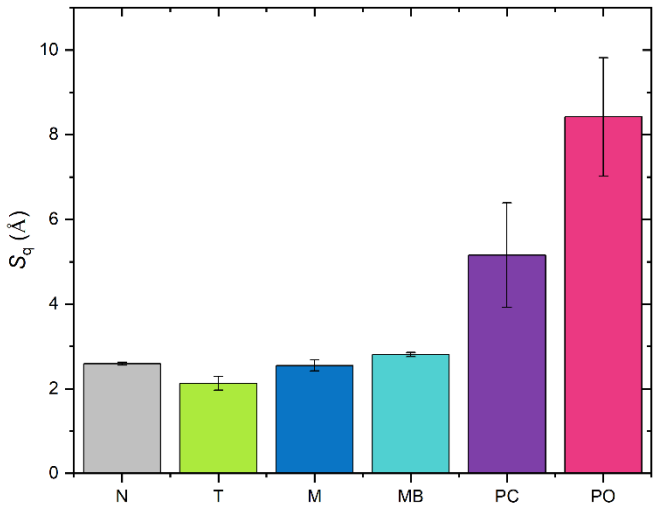

Figure 33: Average rms roughness S_q of the different SiO_x surfaces as determined from the AFM images (n = 4) with the error bars indicating the standard deviations.

The chemical composition of the different SiO_x surfaces after wet-chemical oxidation was investigated by XPS. A quantitative analysis of the XPS data is presented in Table 2. To identify the characteristics of the SiO_x films as determined by XPS, the O:Si ratio, the separation between the O1s and Si2p peaks, and the full width at half maximum (FWHM) of the O1s peak were used. The native oxide surface N has the lowest O:Si ratio (1.40, within the oxide layer) of all samples. This is frequently observed for

native surface oxides,(*233*) which in general are partly sub-stoichiometric.(*248*) The PO surface was also found to be slightly sub-stoichiometric, with a O:Si ratio of 1.61. All other surfaces have an average O:Si ratio of 2.01 ± 0.10, corresponding to stochiometric SiO_2. Additionally, SiO_x was identified using the distance between the O1s and Si2p peaks, Δ(O1s-Si2p) instead of the measured value of the binding energies of the peaks, because the thicker oxide films displayed charging during the XPS measurement. The average separation between the O1s and Si2p peaks is 429.6 ± 0.2 eV corresponding clearly to SiO_2.(*249*) The FWHM of the O1s peak also shows only minor fluctuations between surfaces, with an average value of 1.71 ± 0.09 eV. Except for the sub-stoichiometric nature of surfaces N and PO, the XPS analysis of the surfaces shows no notable differences or trends between samples.

Sample	O1s (O-Si) (at%)	O1s (O-H) (at%)	Si2p (Si-O) (at%)	Si2p (Si-Si) (at%)	O:Si	O-H:O-Si	Δ(O1s-Si2p) (eV)	O1s (Si-O) FWHM (eV)
N	28.0	1.1	20.0	50.9	1.40	0.039	429.5	1.80
T	64.7	1.2	34.1	-	1.90	0.019	429.4	1.62
M	65.2	1.3	33.5	-	1.95	0.020	429.5	1.72
MB	67.4	0.8	31.8	-	2.12	0.012	429.5	1.70
PC	66.9	1.0	32.1	-	2.08	0.015	429.6	1.83
PO	60.4	2.1	37.5	-	1.61	0.035	429.9	1.60

Table 2: Quantitative analysis of the XPS data. The O:Si ratio was calculated using the O1s peak component of SiO_x (OH component not considered) and the corresponding Si2p component. The OH:O-Si ratio was calculated using the OH and the Si-O components of the O1s peak. The O1s to Si2p at % ratios were calculated from the peak areas with appropriate normalization factors.

DNA origami adsorption on SiO_2 surfaces is strongly influenced by their hydroxylation state.(*250*) This was addressed also by XPS by a thorough analysis of the O1s core level. The peak was decomposed into two components, of which the most intense component was assigned to O-Si bonds, and the much smaller component, placed at a fixed 1.5 eV higher binding energy position, to -OH groups.(*251*) The ratio O-H:O-Si obtained from the two components is shown in Table 2 as well. Interestingly, there is a negative linear correlation between O-H:O-Si and O:Si (see

Figure 34). This suggests that the variations in the O-H:O-Si ratio are not caused by different surface densities of OH groups but rather by differences in the SiO_x stoichiometry. Therefore, we assume that all SiO_x surfaces have similar hydroxylation states after wet-chemical hydroxylation.

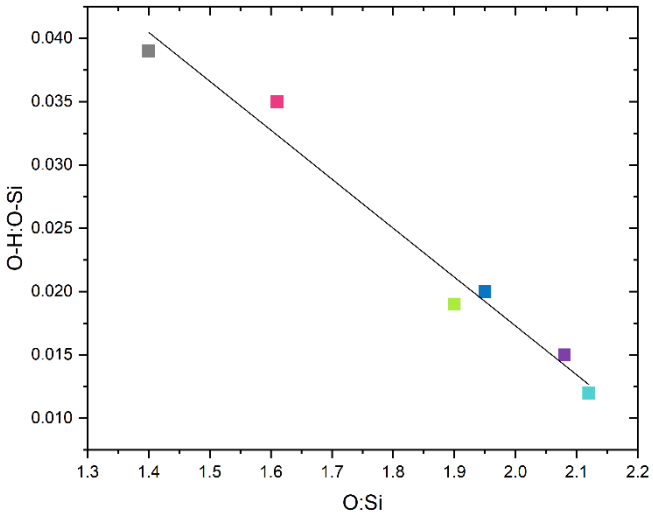

Figure 34: Correlation between the O-H:O-Si and the O:Si ratios given in table 1. Colors indicate the different samples as shown in Figure 2. The solid line corresponds to a linear fit to the data.

DNA Origami Lattice Formation

DNA origami lattice formation on the different SiO_x surfaces was investigated using Rothemund triangles(*15*) and a protocol established previously for RCA1-treated silicon wafers with hydroxylated native surface oxide.(*156*) For this, 3 nM DNA origami triangles were incubated for 3.5 h on the different surfaces at 40 °C in the presence of 12.5 mM $CaCl_2$ and 400 mM NaCl. Afterwards, the adsorbed DNA origami nanostructures were fixed at the surfaces by Ni^+ ions and transferred into the dry state. Figure 35 shows AFM images of the dried surfaces. Despite the highly similar chemical compositions of the six SiOx surfaces, remarkable differences in DNA origami adsorption and lattice formation are observed. The native and the thermal oxide surfaces both show DNA origami lattices of expected quality(*156*) with no major differences. For the other four surfaces, however, DNA origami coverage is dramatically reduced. Of those surfaces, MB shows the highest DNA origami coverage, which, however, is still far from that of a complete monolayer. For surface M, surface coverage is further reduced and only very few DNA origami triangles can be identified in the AFM images. For the two PE-CVD surfaces, barely any DNA origami nanostructures are visible at all.

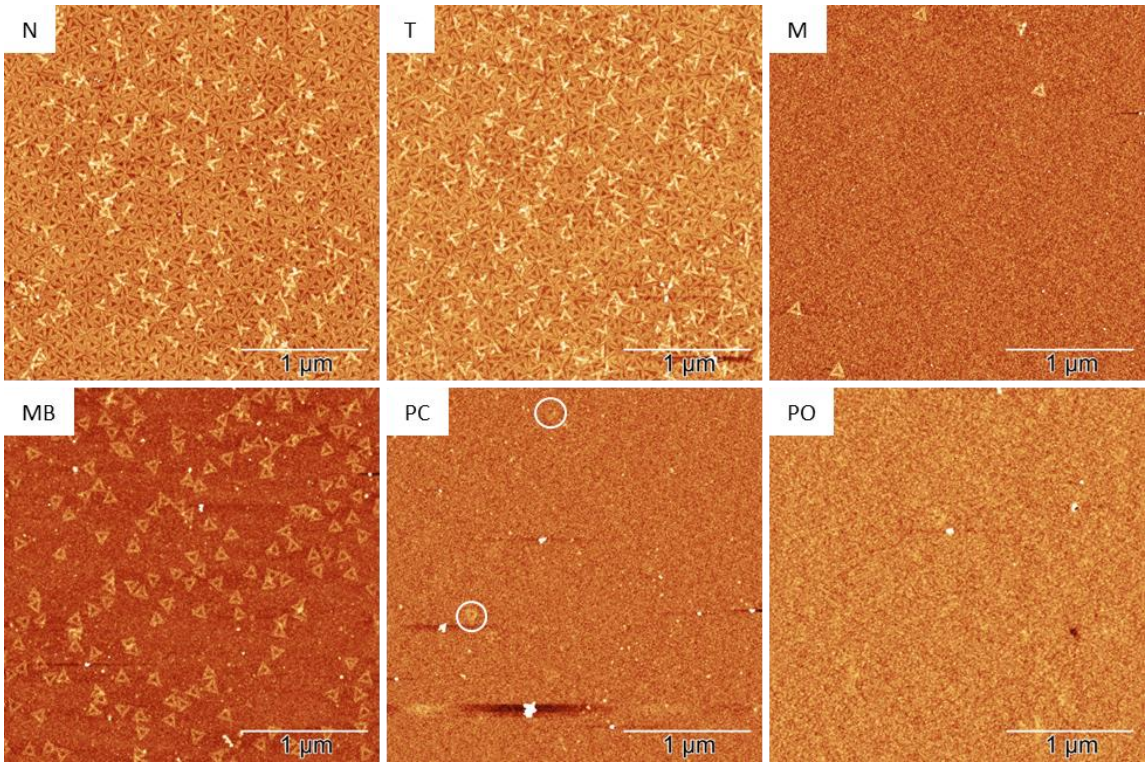

Figure 35: AFM images of the different SiOx surfaces after DNA origami adsorption and lattice formation. In the image of surface PC, two adsorbed DNA origami triangles can be identified (white circles). Height scales are 5 nm (N, T), 3.5 nm (M), 6 nm (MB), 9 nm (PC), and 14 nm (PO)

DNA origami surface coverage was quantified from the AFM images of the different surfaces and is shown in Figure 35. Surfaces N and T have very similar surface coverage larger than 90 % of an ideal monolayer (ML), whereas that of surface MB is only about 10 ML%. For the other three surfaces, surface coverage is below 1 ML%. The extremely low DNA origami adsorption on both PE-CVD surfaces is probably caused by their high surface roughness (see Figure 33). The reasons for the reduced surface coverage on the MSD surfaces, however, are less obvious. As can be seen in Figure 33, the M and MB surfaces have almost identical S_q values as the N and T surfaces. Furthermore, while XPS did reveal variations in the surface chemistry of these four surfaces, they do not follow the same trend as the surface coverage (see Table 2). For instance, surfaces T and M have almost identical O:Si and O-H:O-Si ratios, but very different surface coverage. In contrast, surfaces N and T have almost identical surface coverage, but different O:Si and O-H:O-Si ratios, as well as different O1s (Si-O) FWHM. This suggests that the differences in DNA origami adsorption are caused not by variations in the chemical composition of the different oxides but rather by different physical properties.

Considering only the two MSD surfaces, surface MB that was produced in the presence of a bias of -20 V shows a higher DNA origami coverage than surface M, which was produced without bias. Since the application of a negative bias during MSD increases the density of the deposited films,(*233, 247*) it is rather obvious to attribute the enhanced DNA origami adsorption to an increased film density.

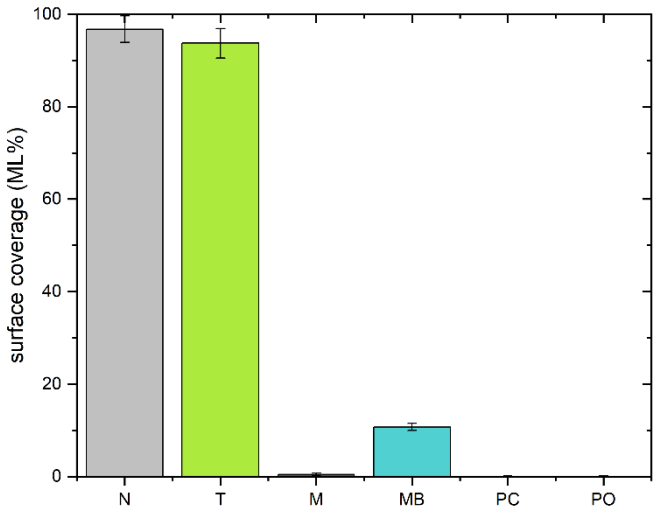

Figure 36: Average DNA origami surface coverage in percent of an ideal, densely packed monolayer (ML%) as determined from the AFM images (n = 4).

Furthermore, it is well established that thermally grown SiO_x films have a higher density than sputtered oxides.(*252*) Therefore, the strong variations in DNA origami coverage observed on the different SiO_x surfaces can be attributed to two independent parameters, *i.e.*, surface roughness and oxide density, with efficient lattice assembly requiring SiO_x surfaces of low surface roughness and high oxide density.

3.3.3 Conclusion

We have investigated the influence of the type of the SiO_x surface on surface-assisted DNA origami lattice assembly. Even though all surfaces were wet-chemically oxidized and hydroxylated prior to the experiments and thus were chemically very similar as verified by XPS, we observed strong differences in DNA origami adsorption and lattice assembly. Among all surfaces tested, only thermally grown oxide films performed similarly well as silicon wafers with native surface oxide, whereas DNA origami adsorption was dramatically reduced on SiO_x surfaces prepared by MSD and PE-CVD. While the latter can be explained by the larger surface roughness of the PE-CVD surfaces, the MSD surfaces are rather similar to the native and/or the thermal oxide in terms of surface roughness, film composition, and hydroxylation state. Nevertheless, application of a substrate bias during MSD resulted in slightly increased DNA origami adsorption, which we attribute to a higher density of the SiO_x films deposited with bias.(*233, 247*) In combination with the fact that thermally grown SiO_x has a much higher density than sputtered oxide films,(*252*) we conclude that the density of the grown SiO_x films is a dominant factor with a surprisingly strong influence on DNA origami adsorption and lattice assembly.

Our results demonstrate that the employed SiO_x surface may decide over the outcome of an experiment and should be considered as an additional parameter that may require tuning and optimization before high-quality lattices can be assembled. In particular, our results suggest that efficient DNA origami lattice assembly on SiO_x surfaces requires a low surface roughness and a high

oxide density. While these requirements may automatically disqualify SiOx surfaces prepared by certain techniques, oxide density may be increased either during deposition by appropriate choices of experimental parameters such as the application of a negative substrate bias during MSD, or by additional post-deposition processing steps such as hydrogen plasma treatment.(*253*)

Finally, we would like to note that our results do not necessarily imply that it is impossible to assemble ordered DNA origami lattices on the SiO_x surfaces fabricated by MSD without additional surface treatments. Rather, we assume that different environmental parameters are required to stimulate DNA origami adsorption and lattice formation on these surfaces. For this, however, one may have to screen a large number of parameters, including species and concentrations of the mono- and divalent cations, substrate temperature, DNA origami concentration, and possibly pH of the buffer solution, every time DNA origami lattices should be assembled on a new type of SiO_x surface. In such cases, it may turn out economically more beneficial to develop a protocol for a well characterized and highly reproducible SiO_x film that can be deposited on various substrates without major changes in its density and surface roughness. The viability of this route should be explored in future studies.

3.3.4 Materials and Methods

Wafer Preparation

The substrates for the SiO_x films were commercially available epi-ready p-doped Si(100) wafers (Siegert Wafer, resistivity 1-10 Ωcm, thickness 675 ± 25 µm, single-side polished). Prior to thermal oxidation, MSD, and PE-CVD, the wafers were cleaned in RCA1 solution (1:1:5 35% H_2O_2, 25% NH_3, H_2O) for 15 min at 75 °C to remove organic contaminants. This cleaning step was repeated with the SiO_x-coated wafers directly before DNA origami adsorption to generate hydrophilic, hydroxylated surfaces as previously reported.(*156*)

Thermal Oxidation

The cleaned wafers were placed in a pre-heated oven (RHF 1500, Carbolite) in ambient atmosphere at 1200 °C. After 5 min, the samples were removed from the oven and left at room temperature to cool down.

MSD (Performed by Chantal Theile-Rasche, Paderborn University, Paderborn, Germany)

The cleaned wafers were introduced into a magnetron system containing a vacuum chamber, an RF generator (bdiscom), an automatic matching network (BDS ANM750, bdiscom), and a mass flow controller (EL FLOR SELECT, FLOW-BUS). The system reached a base pressure of 1.6×10^{-5} mbar. The magnetron (Thin Film Consulting) was capped with a circular Si target of 2” diameter and 5 mm thickness (99.999 % purity, Evochem Advanced Materials). The magnetron had an unbalanced configuration, and the sample was placed at a distance of about 45 mm from the target. SiO_x

deposition was performed at a working pressure of 4.6 x 10^{-3} mbar with an Ar flow of 27 sccm and an O_2 flow of 3 sccm. The forward power was set to 10 W resulting in a DC Bias of 171 ± 17 V. For surfaces MB, a bias voltage of -20 V was applied to the substrate, leading to an increase in DC voltage to 215 ± 37 V. The deposition rate was determined via a quartz crystal microbalance (QCM) to be about 1.26 nm/min. A deposition time of 8 min was chosen to generate films with a thickness of approximately 10 nm.

PE-CVD (Performed by Hendrick Müller, Paderborn University, Paderborn, Germany)

The wafers were placed onto a grounded electrode. The base pressure was below 5 x 10^{-5} mbar while the working pressure ranged between 0.2 and 0.5 mbar. As mixture of argon, oxygen and hexadimethylsiloxane (HMDSO, 98.5 % purity, Sigma Aldrich) was used in different ratios. For the deposition of SiO_x, the partial pressure of argon and oxygen was set to 0.1 mbar and 0.3 mbar, respectively. The monomer partial pressure was set to 0.05 mbar. The high partial pressure of oxygen in a ratio of 3:1 promotes the formation of SiOx films. The plasma voltage was 430 V while the power was 1 W. The plasma frequency was 3.5 kHz. For the SiOCH deposition, the partial pressure of argon was increased to 0.2 mbar. The plasma voltage was 405 V and the plasma power was 0.9 W. The plasma frequency was 3.5 kHz. The thickness of the deposited films was monitored with a QCM.

Ellipsometry (Performed by Chantal Theile-Rasche, Paderborn University, Paderborn, Germany)

To determine the thickness of the as-deposited oxide films, a nulling ellipsometer (Nanofilm EP3, Accurion) was used. The spectroscopic measurements were performed over a range of wavelengths from 363.7 nm to 882.5 nm with an angle of incidence of 75°. The applied optical layer model consisted of Si(100), SiO_2 and air. The dispersions were obtained from the software database, which are based on the public Sopra database (www.sspectra.com/sopra.html).

XPS (Performed by Chantal Theile-Rasche, Paderborn University, Paderborn, Germany)

The coated substrates were inserted into the XPS setup shortly after RCA1 treatment with exposure times to air ranging from some tens of minutes to three hours for the different samples. XPS was performed using a laboratory setup equipped with a Phoibos 150 NAP analyzer from SPECS. The X-ray source employed monochromatized Kα radiation (1486.7 eV), generated by a µ-FOCUS 600 NAP source. This source produces a spot size of approximately 250 – 300 µm in diameter and impinges on the sample at an angle of 56.5° relative to the surface normal. The detection is done at 0° relative to the surface normal. The power used for the measurements was 50 W. The nozzle used for the experiments had an aperture of 300 µm, with the nozzle-sample distance ranging between 230 and 250 µm. The background pressure during the measurements was maintained at 10^{-8} mbar. All measurements were conducted at room temperature. Survey spectra were acquired with a pass

energy of 100 eV, while core level spectra were recorded at a pass energy of 40 eV. Under the latter conditions, the FWHM of the $Au4f_{7/2}$ peak was 0.87 eV, at a binding energy of 84.2 eV.

The evaluation of the data was performed with the Unifit software using a Shirley-type background and a convolution of Gauss and Lorentz line shapes. The Si2p peaks were fitted using doublets for the $Si2p_{3/2}$ and $Si2p_{1/2}$ components. The intensity ratio was 2:1 and the separation between the peaks was 0.6 eV.

The O1s peaks were decomposed in two components. The most intense component was assigned to O-Si bonds, and the smaller component, placed at a fixed 1.5 eV higher binding energy position, to -OH groups. In the fit, both components were forced to have the same width. The FWHM of the Gauss component was left free to fit, while the FWHM of the Lorentz component was fixed to 0.27 eV.

DNA Origami Lattice Assembly

DNA origami triangles were synthesized and purified as previously described(*156*) using the 7249 nt M13mp18 scaffold (Tilibit) and 208 staple strands (Eurofins). For lattice assembly, we used the protocol previously established for RCA1-treated silicon wafers with native surface oxide.(*156*) In short, the freshly cleaned substrates were placed in a liquid cell placed inside a Petri dish with a small water reservoir to avoid the evaporation of the sample. The liquid cell was filled with 500 µL of 1xTAE (Carl Roth) with 400 mM NaCl, 12.5 mM $CaCl_2$ and 3 nM DNA origami triangles. The filled and covered Petri dish was incubated for 3.5 h at 40 °C (INCU-Line, VWR). Afterwards, the liquid cell was placed on ice for 15 min and 25 µL of 50 mM $NiCl_2$ solution was subsequently added to the sample. After incubation for another 15 min, the substrate was removed, washed with 15 mL HPLC-grade water, and dried with a stream of argon.

AFM

The different surfaces before and after DNA origami adsorption were imaged in air using a Bruker Dimension ICON operated in ScanAsyst Peak-Force Tapping mode with ScanAsyst Air cantilevers (Bruker). For each surface before and after DNA origami adsorption, four AFM images were recorded at different positions with 1024 x 1024 pixels and a scan size of 3 x 3 μm^2.

The AFM images were analyzed using Gwyddion.(*254*) The rms surface roughness of each image was calculated using the Statistical Quantities tool. For surfaces N and T, DNA origami surface coverage was determined by thresholding as previously described.(*156*) Since the other surfaces exhibited a much lower surface coverage and a pronounced background topography originating from residual salt and, in the case of the PE-CVD surfaces, a higher surface roughness, the thresholding approach suffered from large artefacts. Therefore, the adsorbed DNA origami nanostructures for each image were counted manually instead. The relative surface coverage and number of DNA origami

nanostructures, respectively, of each image were then normalized to those of an ideal, densely packed monolayer. The Rothemund triangle has an outer and inner edge length of about 120 and about 50 nm, respectively. A densely packed, hexagonally ordered monolayer will thus feature 160 triangles per μm^2, corresponding to a relative surface coverage of 83 %.

Statistical Analysis

The rms roughness and surface coverage values are presented as the mean of four AFM images (n = 4) ± standard deviation.

Chapter 4: Interaction of Viruses with Cells and Surfaces Studied by QCM-D

4.1 Monitoring Phage Infection and Lysis of Surface-immobilized Bacteria by QCM-D

4.1.1 Introduction

Bacteriophages, also known as bacterial viruses, are minuscule particles that have the ability to infect bacteria and replicate exponentially by hijacking the host cell's genetic machinery.(*255, 256*) Phages are omnipresent in nature, cohabiting with bacteria and sustaining their population through perpetual cycles of eradication. Consequently, new phages are continuously discovered in diverse environments ranging from the deep sea(*257*) to human wastewater.(*258*) While phages contribute to the spreading of bacterial virulence(*259*) and antibiotic resistance genes,(*260*) they can also be utilized to treat antibiotic-resistant bacterial infections in what is called phage therapy.(*261*) However, while there is an increasing number of case studies reporting positive treatment outcomes under compassionate use, clinical trials so far had mixed success.(*261, 262*) The latter is rooted in a number of challenges that the clinical implementation of phage therapy faces. Chief among them is the high strain-specificity of many phages, which requires the preparation of cocktails of different strain-specific phages that can effectively treat a large number of clinical isolates of the target pathogen.(*261–263*) To achieve this, large collections of hundreds of phages need to be screened.(*262, 263*) While several methods have been developed or adapted for this purpose, ranging from well-established plaque assays(*264*) to more sophisticated techniques such as qPCR,(*265*) surface plasmon resonance,(*266*) atomic force microscopy,(*267*) and several fluorescence-based assays,(*268, 269*) all these approaches have their own disadvantages and limitations, in particular regarding response time, universality, ease of use, and throughput.(*262*) Furthermore, phage therapy is considered a promising strategy against biofilm-related infections that are particularly difficult to treat.(*270*) Most high-throughput screening techniques, however, are compatible only with planktonic cells. Consequently, there is a growing demand for surface-sensitive analytical techniques that enable the efficient screening of phages against bacterial biofilms.

Quartz crystal microbalance with dissipation monitoring (QCM-D) is a label-free technique that detects changes in the mass and viscoelasticity of a thin adsorbate film on the surface of a piezoelectric quartz sensor *in situ* and in real time. An AC voltage is applied across the sensor, which in response undergoes a shear oscillation at its resonance frequency in the MHz range. Adsorption or desorption events on the sensor surface result in shifts in the sensor's resonance frequency Δf and energy dissipation ΔD,

which can be translated into changes in mass and viscoelastic properties, respectively, by the application of appropriate models.(*83*) Because of its exceptional mass sensitivity(*271*) down to a few ng/cm² and the commercial availability of highly automated multichannel systems,(*272*) QCM-D has become a powerful method for the screening of biomolecular and cellular interactions. As such, it is employed in various biomedical research fields such as drug discovery,(*273, 274*) drug delivery,(*275, 276*) amyloid aggregation,(*277, 278*) bacterial adhesion,(*279, 280*) and biofilm formation.(*281, 282*)

In this work, we evaluate the potential of QCM-D to monitor phage infections of bacteria in real time. To this end, *Escherichia coli* cells are adsorbed on the gold surface of the QCM-D sensor and subsequently exposed to infectious bacteriophage T7 or non-infectious phage phi29. T7 was specifically selected because of its short lytic life cycle of only 17 min.(*283*) We demonstrate that this approach is able to distinguish infectious from non-infectious phages within four hours. We also show that phage-induced lysis can be detected using only a single measurement parameter, *i.e.*, the spread between the different overtones of the ΔD traces, which substantially reduces the complexity of the evaluation of the sensor response and will aid future phage screening campaigns.

4.1.2 Results and Discussion

E. coli Adsorption, Adhesion, and Growth on the QCM-D Sensor Surface

Before investigating the effects of T7 infection by QCM-D, Figure 37a,b evaluates the QCM-D response of *E. coli* adsorption and growth on the QCM-D sensor in the absence of any phages for the overtones three to eleven. Injection of bacteria-containing LB medium results in a rapid decrease in Δ*f* for all overtones, which corresponds to an increase in mass and thus is indicative of the adsorption of bacteria and possible molecular components of the medium on the sensor surface. At the same time, Δ*D* shows a rapid increase, indicating that the system becomes more viscoelastic due to adsorbing and adhering to bacteria. Both Δ*f* and Δ*D* saturate rather quickly, at which point their overtones start separating from each other. Flushing of the flow cell with bacteria-free medium results only to minor changes in the Δ*f* and Δ*D* traces, indicating that the bacteria stably adhere to the sensor surface. After flushing, the pump was stopped, and the behavior of the adhering bacteria was monitored under static conditions. Over the following two hours, both Δ*f* and Δ*D* increase in value, which is accompanied by increased spreading between the overtones of Δ*D*. The increase in Δ*D* as well as the large spread between its individual overtones are consistent with bacteria growing on the surface. A larger number of adhering bacteria leads to more efficient energy dissipation due to their intrinsic viscoelasticity and the enhanced coupling to the liquid phase. At the same time, the effective thickness of the bacterial film increases with the number of bacteria, which accounts for the increased spread between overtones. This is because the penetration depth of the acoustic shear wave into the medium

decreases with increasing overtone number.(*90*) For the third overtone, the penetration depth into an aqueous medium is about 140 nm, which is considerably smaller than the diameter of an *E. coli* cell.(*284*) The eleventh overtone, however, has an even smaller penetration depth of only about 70 nm.(*90*) Therefore, while the lower overtones sense a certain fraction of the more liquid-like bacterial cytoplasm, the higher overtones are more sensitive toward the stiffer cell envelope close to the sensor surface. Surprisingly, Δ*f* increases as well in this regime. At first glance, this indicates the desorption of bacteria instead of bacterial growth. Nevertheless, such positive shifts of Δ*f* are frequently observed during bacterial adhesion and biofilm formation on the sensor surface, which follows a coupled resonance model instead of conventional Saurbrey theory.(*281, 285, 286, 89*) In this context, it was shown Δ*f* is not a reliable measure of the number of bacterial cells adhering to the sensor surface,(*287*) so that detailed analyses of their behavior should rather be based on ΔD.(*288, 289*)

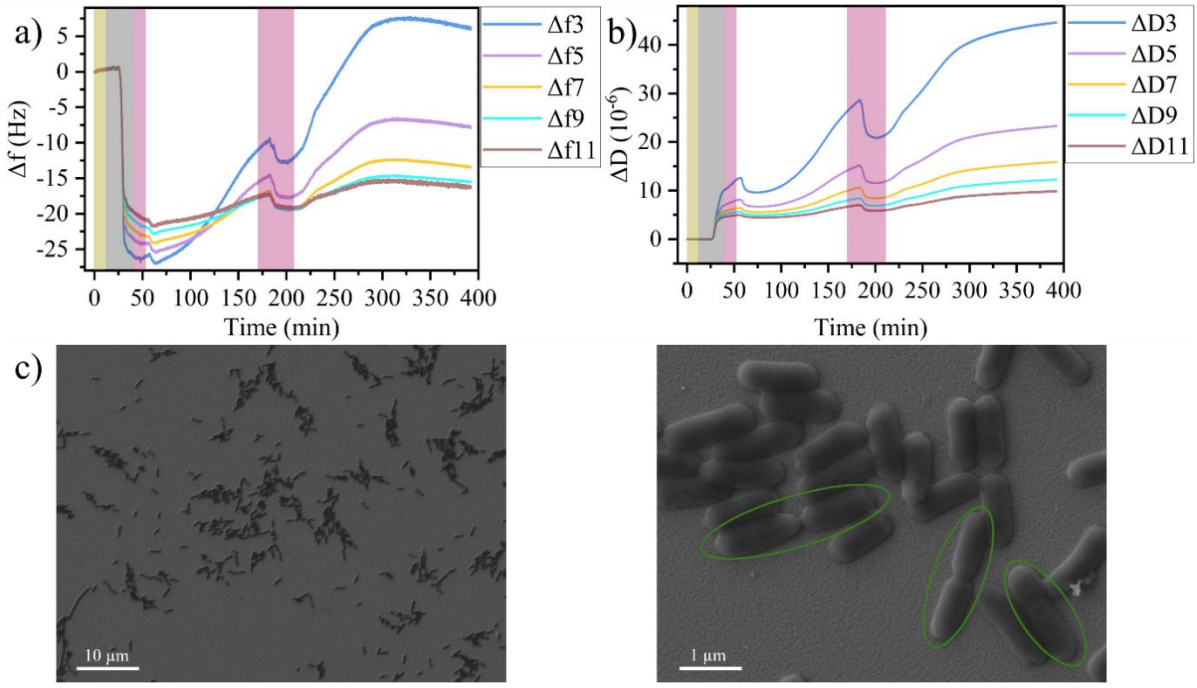

Figure 37: Change in frequency Δf (a) and dissipation ΔD (b) during E. coli adsorption and growth on the QCM-D sensor surface. Shaded regions indicate the injection of different media: yellow – PBS, grey – bacteria in medium, pink – medium. c) SEM images of the sensor surface after the experiment at two different magnifications. Dividing bacteria are highlighted.

Flushing the flow cell once more with medium about 170 min after the start of the experiment leads to a decrease in both Δ*f* and Δ*D*. This is indicative of the desorption of loosely bound bacteria from the sensor surface and a simultaneous increase in the adhesion of the remaining bacteria. Immediately after flushing, both Δ*f* and Δ*D* increase again until they saturate about 100 min later. In this phase, the spread between the individual overtones increases as well. These behaviors of the Δ*f* and Δ*D* traces are thus consistent with the resumed growth of bacteria firmly attached to the sensor surface, which

continues until the medium in the flow cell (volume ~ 40 µl) is depleted of nutrients. Bacterial growth was further verified by SEM imaging of the sensor surface after the end of the QCM-D measurement. Several stages of dividing bacteria (see Figure 37c) can be identified, which proves that bacterial growth is resumed after addition of fresh medium. The SEM images in Figure 38 further reveal several long filamentous bacterial cells. MacConkey and EMB agar cultures (see Figure 39) indicate that these cells are not the result of contamination but indeed filamentous *E. coli* cells. Filamentation of *E. coli* and other bacteria is a common phenomenon.(*290, 291*)

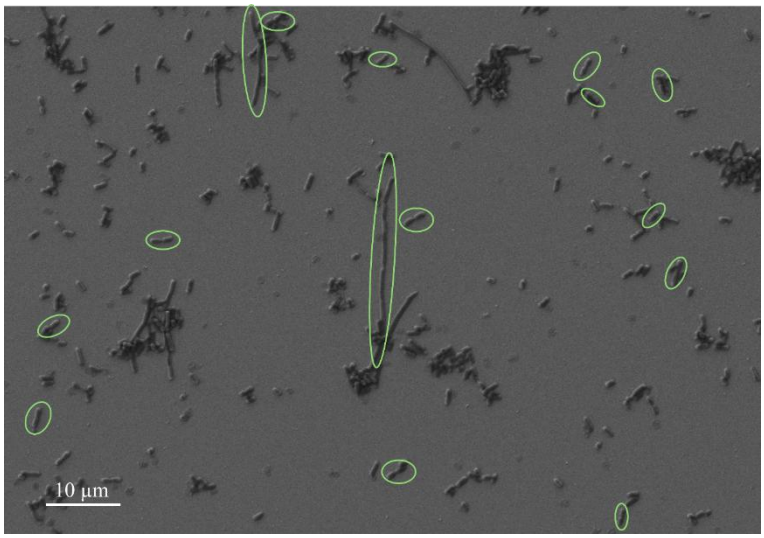

Figure 38: SEM image of the sensor surface after the experiment in Figure 1 without phages. Dividing bacteria with and without notable cell separation are highlighted.

While occurring naturally at a low rate, filamentation is induced under stress conditions, including starvation, temperature shock, and antibiotics exposure.(*292*) However, surface immobilization and shear flows have also been identified as factors that may stimulate filamentation of *E. coli*.(*293*) In our experiments, the bacteria are immobilized on the sensor surface, subjected repeatedly to shear flows, and grown under static conditions with limited nutrient availability, all while being exposed to acoustic surface waves of 5 MHz. The stress resulting from those conditions may induce filamentation of some of the immobilized cells indeed. This filamentation may then further lead to an additional increase in dissipation.

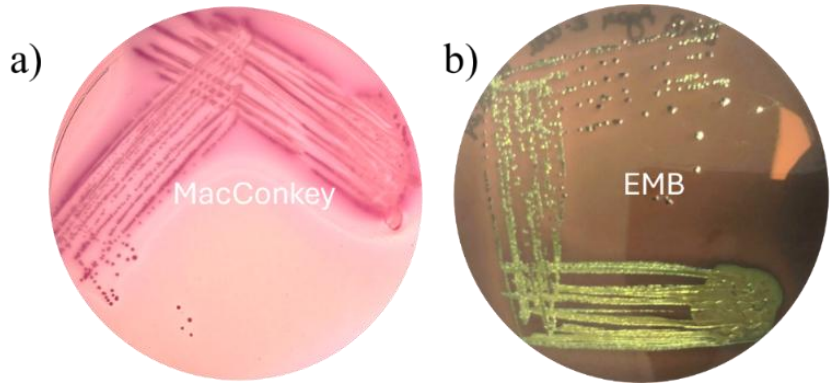

Figure 39: a) E. coli quadrant streaked on MacConkey agar showing pink non-mucoid colonies of lactose-fermenting E. coli. b) E. coli quadrant streaked on EMB agar showing colonies with green metallic sheen.

A general issue in QCM-D is the strong dependence of the measurement on the employed sensor, with seemingly identical sensors often having rather different sensitivities and responses. In these experiments, the strongest deviations between measurements are observed in the Δ*f* traces, which in some cases show positive frequency shifts during bacterial adhesion and growth, while in other cases, negative shifts are observed. The ΔD curves, however, follow rather similar trends, in further support of Δ*D* being the more relevant parameter for evaluating bacterial adhesion and growth. Here, the most notable differences are observed after the second injection of medium, i.e., in the second growth stage. While flushing with medium leads in all experiments to a drop in ΔD that is followed by an increase with subsequent saturation, the overall magnitude of the increase and the saturation level vary.

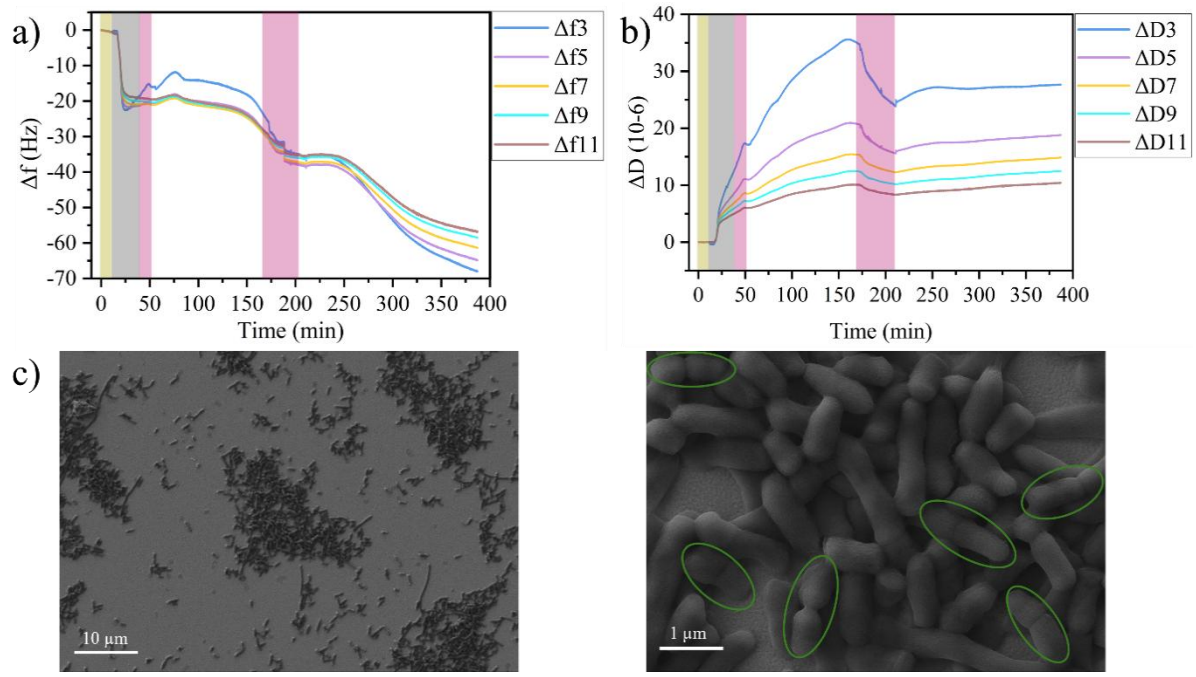

Figure 40: Replicate of the data shown in Figure 37. Change in frequency Δf (a) and dissipation ΔD (b) during E. coli adsorption and growth on the QCM-D sensor surface. Shaded regions indicate the injection of different

media: yellow – PBS, grey – bacteria in medium, pink – medium. c) SEM images of the sensor surface after the experiment at two different magnifications. Dividing bacteria are highlighted.

The SEM images shown in Figure 37 and Figure 40 suggest that these differences result from different numbers of bacteria and/or the formation of microcolonies on the sensor surface, which most likely are caused by different surface properties of the gold electrodes. Even though AFM reveals rather similar surface topographies (see Figure 41), surface inhomogeneities over larger length scales may lead to locally different bacterial adhesion and growth.

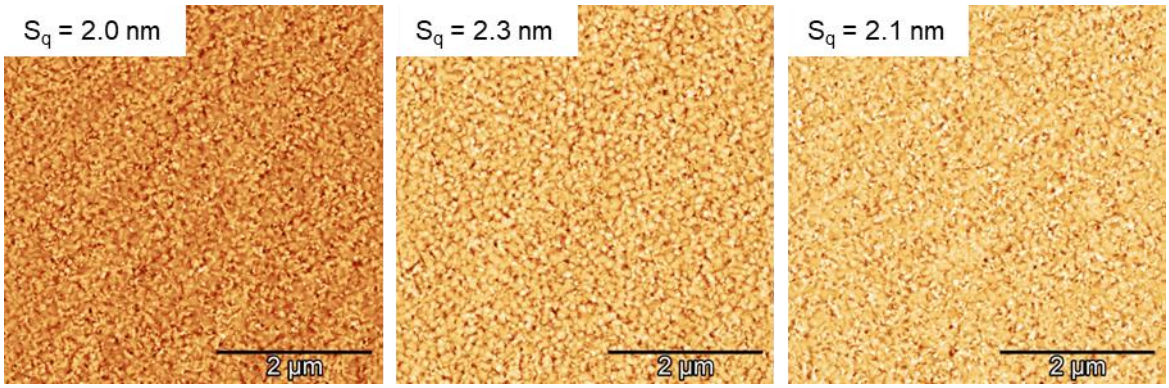

Figure 41: AFM images of the gold electrode surfaces of three QCM-D sensors from different batches. Height scales are 20 nm. The values of the root-mean-square (RMS) surface roughness Sq are given in the images.

T7 Phage Infection of *E. coli* on the QCM-D Sensor Surface

To follow phage infection by QCM-D, T7 phages in medium were injected during the second flushing step after ca. 165 min (see Figure 42a,b). The phages at a concentration of ca. 8 x 10^7 PFU/mL were pumped through the flow cell for 30 min to facilitate their binding to the bacteria. Afterwards, the flow cell was flushed again with phage-free medium to remove unbound phages. As soon as the flow cell is flooded with phages, both Δf and ΔD show a rapid decrease that exceeds that observed for flushing with phage-free medium. For instance, for the third overtone, Δf drops by about -60 Hz when phages are injected, but by less than -5 Hz for flushing with phage-free medium in the bacterial control without phages (see Figure 37a). This indicates the rapid adsorption of phages on the bacteria and the free sensor surface. Bacteria-free control experiments with the sensors exposed to phages only reveal a much larger drop in Δf due to phage adsorption on the free gold surface. This drop in Δf, however, is accompanied by a large *increase* in ΔD, whereas in the presence of bacteria on the sensor surface, ΔD *decreases* upon phage injection (see Figure 42b). In addition, this decrease is about twice as large as the one observed in Figure 37b for flushing with phage-free buffer. This verifies that the behavior observed in Figure 42a,b does not result from simple phage adsorption on the QCM-D sensor but additionally involves specific interactions between phages and bacteria. After flushing with phage-free medium, the Δf and ΔD traces both rapidly saturate before entering an extended regime, in which Δf shows a slight but continuous decrease while ΔD increases correspondingly (see Figure 42a,b). The

sensor response in this regime is very different from that observed in Figure 37a,b and does not show any indication of bacterial growth. Notably, both the absolute ΔD values and the spreading of the individual overtones at the end of this regime are much lower than those observed in Figure 37b, indicating a more rigid adsorbate film.

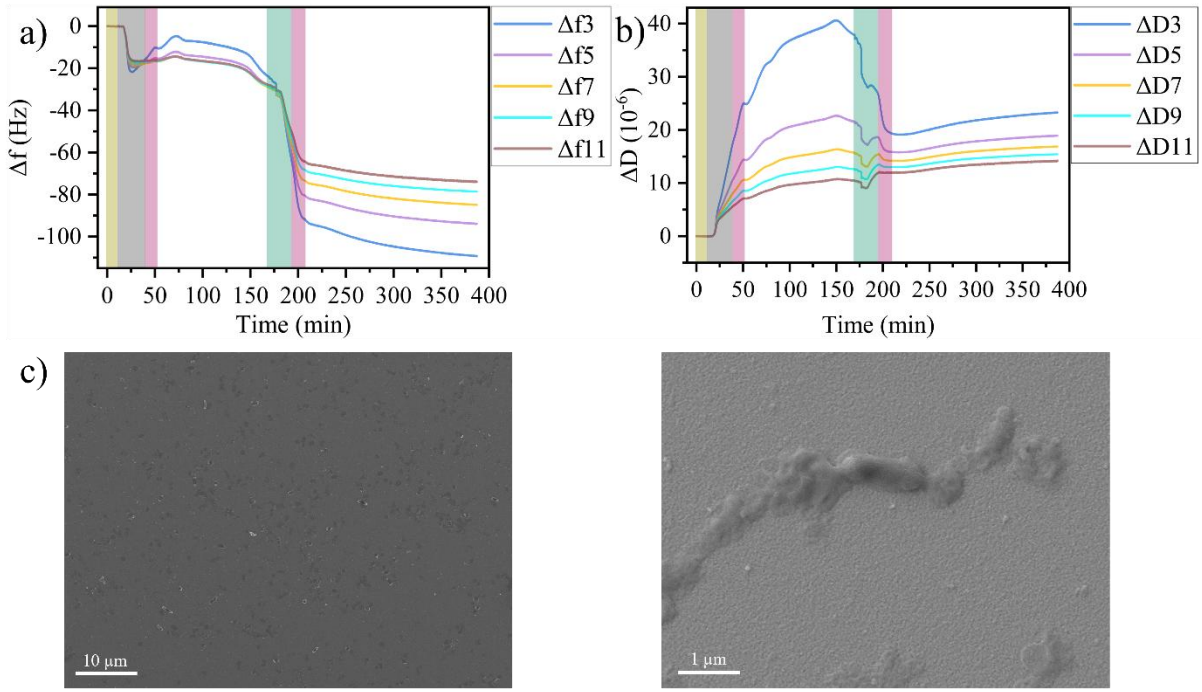

Figure 42: Change in frequency Δf (a) and dissipation ΔD (b) during E. coli adsorption, growth, and T7 infection on the QCM-D sensor surface. Shaded regions indicate the injection of different media: yellow – PBS, grey – bacteria in medium, pink – medium, green – T7 phages in medium (8 x 10^7 PFU/mL). c) SEM images of the sensor surface after the experiment at two different magnifications.

These observations are consistent with the phage-induced lysis of the bacterial cells on the sensor surface. Upon lysis, the cell envelope ruptures, the cytoplasm is released into solution, and the empty envelope collapses onto the surface. This leads to stiffer and thinner adsorbate film, which accounts for the decrease in Δ*D* and the reduced spread of its overtones. While the large decrease in Δ*f* during phage injection can be attributed to phage adsorption, the subsequent spread between overtones is now consistent with the presence of a viscous adsorbate layer that consists mostly of cellular debris. However, the slight, continuous increase in Δ*D* over the following three hours may indicate that also some bacteria survived on the sensor surface and now resume to grow. Indeed, while the SEM images in Figure 42c clearly show that the majority of bacteria on the sensor surface have been lysed, a few intact cells can be identified among the dead ones. Furthermore, we would like to point out that cell lysis produces more reproducible sensor responses than cell growth, which underscores the potential of QCM-D to aid in the screening of phage libraries.

Due to the short lytic cycle of T7 of less than 20 min and the comparably high phage concentration of 8 x 10^7 PFU/mL used in the above experiments, lysis of most bacteria will be completed before the flushing with phage-free medium is finished. In order to assess the robustness of the detection scheme, we next lowered the phage concentration to 2 x 10^6 PFU/mL. This will lead to more bacteria surviving the initial phage exposure, while the subsequent flushing will remove free phages from the flow cell so that the surviving cells have a much smaller chance of getting infected. As can be seen in Figure 43a,b, the overall behavior of the Δ*f* and Δ*D* traces up until the final flushing step after phage injection is very similar to that observed at the higher concentration in Figure 42a,b. Only the dynamics of both traces during phage injection appear somewhat slowed down or even delayed, while the overall magnitudes of the observed decrease in Δ*f* and Δ*D* are rather similar to the previous experiment. This is particularly interesting as phage adsorption on the sensor surface in the absence of bacteria is considerably reduced at the lower concentration. This is a clear indication that the observed changes are indeed related to phage infection and lysis of the adhering bacteria.

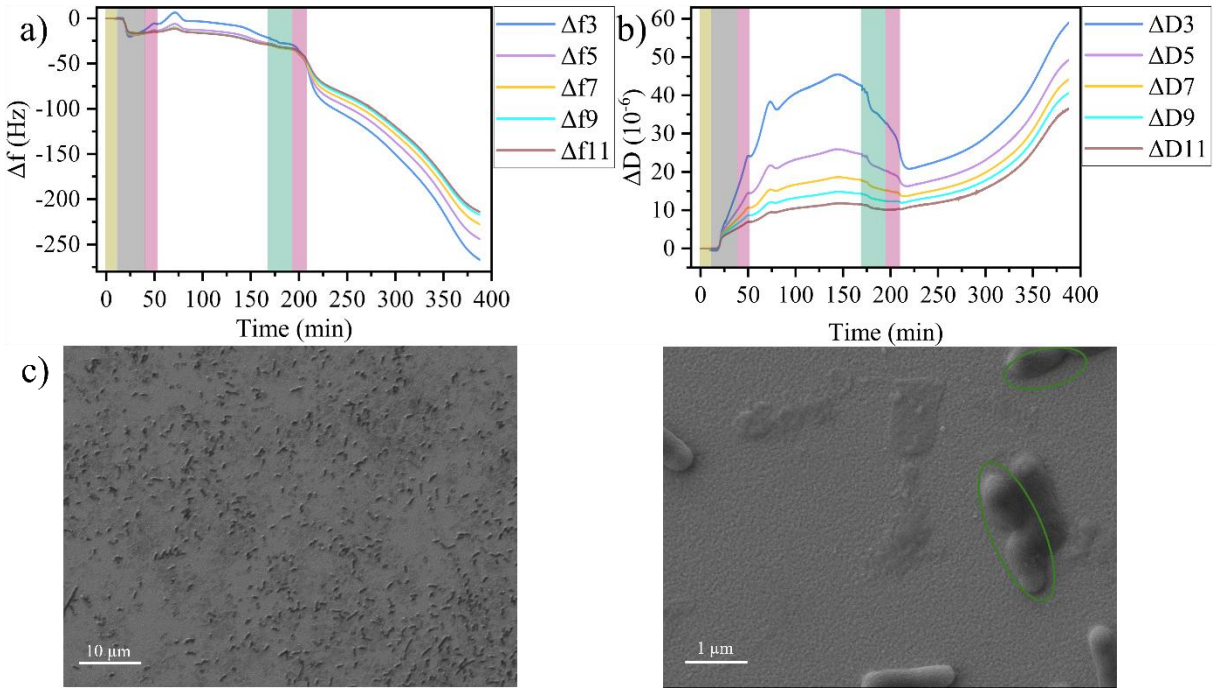

Figure 43: Change in frequency Δf (a) and dissipation ΔD (b) during E. coli adsorption, growth, and T7 infection on the QCM-D sensor surface. Shaded regions indicate the injection of different media: yellow – PBS, grey – bacteria in medium, pink – medium, green – T7 phages in medium (2 x 10^6 PFU/mL). c) SEM images of the sensor surface after the experiment at two different magnifications. Dividing bacteria are highlighted.

The most obvious differences in the Δ*f* and Δ*D* traces of the two concentrations are visible in the final regime after flushing. At the lower phage concentration, Δ*f* and Δ*D* immediately start to decrease and increase, respectively, and continue to do so at a much higher rate as for the higher phage concentration. This indicates that as expected, more bacteria survived the phage exposure at this lower concentration and resumed growth afterwards. The larger number of surviving bacteria is also

supported by the SEM images, which revealed many intact bacteria on the sensor surface (see Figure 43c). Furthermore, dividing bacteria are observed as well (see Figure 43c), supporting our assumption of resumed growth. It should be stressed here that these experiments were conducted under static conditions in ~ 40 µL of medium, *i.e.*, under limited nutrient availability. Lysis of a large number of bacterial cells releases a lot of additional nutrients into the environment, which in the absence of a flow remain available to the surviving cells and can promote their growth.

At an even lower T7 concentration of 4 x 10^5 PFU/mL, a rather similar behavior is observed as at a concentration of 2 x 10^6 PFU/mL. In particular, the ΔD traces in both cases exhibit a slow yet notable increase about 100 min after the second flushing step, indicative of the resumed growth of the surviving bacteria on the sensor surface. This demonstrates that bacterial lysis can be detected reliably also at comparably low phage concentrations.

Exposure to *B. subtilis* Phage Phi29

Finally, we evaluated the QCM-D response to the exposure of the immobilized *E. coli* cells to a non-infecting phage. We chose bacteriophage phi29, which has similar dimensions as T7 but only infects *Bacillus subtilis*.(*294*) Figure 44 shows that injection of phi29 at 2 x 10^8 PFU/mL results in a rapid drop in both Δ*f* and Δ*D*. After flushing with medium, however, both traces quickly recover and increase again until they saturate at about 250 min. The behavior in this regime thus resembles the late-stage growth phase observed in the absence of any phages in Figure 37, Figure 40 and indicates the resumed growth of the bacteria after phi29 injection. This is further verified by SEM (see Figure 44c), which reveals live and dividing bacteria on the sensor surface.

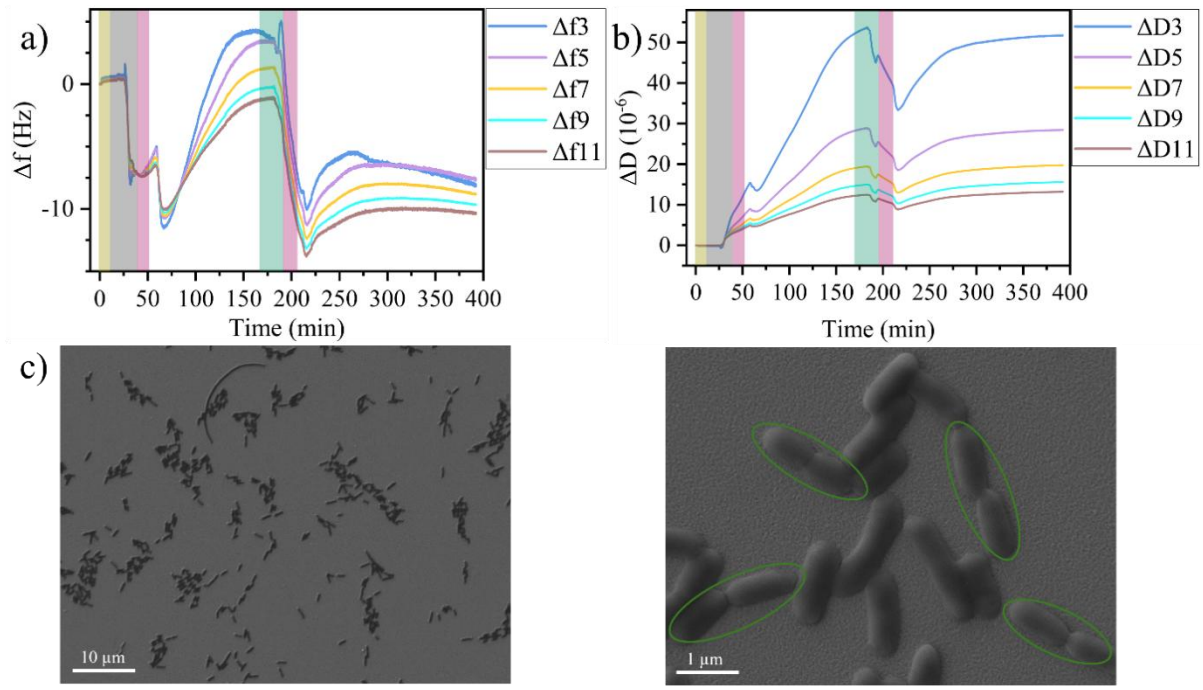

Figure 44: Change in frequency Δf (a) and dissipation ΔD (b) during E. coli adsorption, growth, and phi29 exposure on the QCM-D sensor surface. Shaded regions indicate the injection of different media: yellow – PBS, grey – bacteria in medium, pink – medium, green – phi29 phages in medium (2 x 10^8 PFU/mL). c) SEM images of the sensor surface after the experiment at two different magnifications. Dividing bacteria are highlighted.

Detecting Phage-induced Lysis by a Single Measurement Parameter

Our experiments demonstrate the ability of QCM-D to monitor phage infections of bacteria immobilized on the sensor surface in real time. However, the associated changes in the different overtones of Δ*f* and Δ*D* are rather complex and depend on the individual sensor. This may render the verification of a successful infection and lysis of the target bacterium in a screening campaign with a large phage collection a difficult task. Therefore, we sought to identify a single measurement parameter whose time dependence during the experiments provides a clear and reliable indication whether phage-induced lysis of the target bacterium occurs. Based on the measurements shown in Figures 37, 42, 43 and 44, the spread of the Δ*D* overtones appeared to be the most promising candidate for this purpose. To quantify the total spread, we simply calculated the difference between the absolute values of the third and the eleventh overtone, *i.e.*, δ*D* = Δ*D*3 - Δ*D*11, for the different measurements. To account for the sensor-specific differences in the ΔD traces during the initial growth regime, the δ*D* parameter was then normalized to its maximum value before the second injection. Figure 45 verifies that the time course of normalized δ*D* is similar for all measurements until the second injection at ca. 180 min, showing only minor variations in the time dependence due to the differences observed in initial bacterial adhesion and growth dynamics. Upon injection of phage-free medium (*E. coli* only control), δ*D* drops slightly in all traces but quickly starts to increase again, indicating resumed growth. At longer times, δ*D* saturates when growth is arrested. Here, the

saturation value varies considerably between repeated measurements due to the different numbers of growing bacteria and microcolonies on the sensor surfaces. If the *Bacillus* phage phi29 is present in the injected medium, δD shows a similar behavior with the saturation level within the range of variation observed for the phage-free measurements. In contrast, injection of *E. coli* phage T7 results in a larger drop in δD by about 80%, which remarkably is independent of the T7 concentration (compare red, green, blue, and black curves in Figure 5a). For the high T7 concentration (red curves), δD remains at this low value for the rest of the experiments. For the lower concentrations (green and blue curves), however, it slowly increases again due to the resumed growth of the surviving bacteria. At a selected timepoint of 240 min, this parameter thus yields a significantly smaller value in the presence (+T7) than in the absence (-T7) of infectious phages (Figure 45b). Nevertheless, the addition of phi29 (violet curve) shows a similar behavior as *E. coli* in the absence of any phages (black curves).

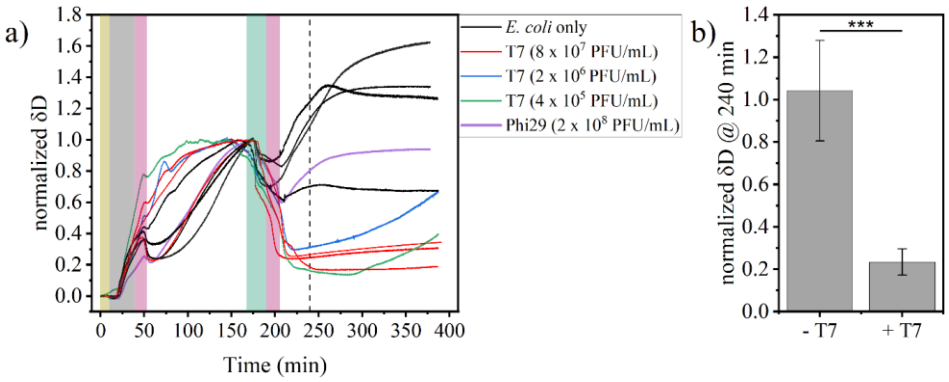

*Figure 45: a) Normalized δD for the experiments shown in Figures 34, 35, 36, 37, 38, and 39, the respective replicates. Shaded regions indicate the injection of different media: yellow – PBS, grey – bacteria in medium, pink – medium, green – phages or medium (E. coli only). b) Comparison of the normalized δD at 240 min (indicated by the broken vertical line in a) averaged over all E. coli only experiments (-T7) and T7 experiments (all concentrations, +T7). Values are given as the mean ± standard deviation. Statistical significance was determined by two-tailed t-test and is indicated as *** ($p < 0.001$).*

To further illustrate and quantify the differences between the normalized δD curves with and without T7 phages, we have calculated the second derivative of each curve for the period after the final flushing with phage-free medium. The resulting derivative curves allow a clear distinction between the two conditions, as the experiments with phages produce curves with mostly positive values, whereas the phage-free curves have mostly negative values (see Figure 46a). Therefore, the values of both the sum and the mean of each derivative curve can be used to discern phage infection and lysis (see Figure 46b,c). As a more direct measure, however, the δD value at a selected timepoint after the final flushing can be utilized as well. At timepoint 240 min, *i.e.*, after the drop in signal due to phage injection has saturated, δD has a significantly smaller value in the presence (+T7) than in the absence (-T7) of infectious phages (Figure 45b).

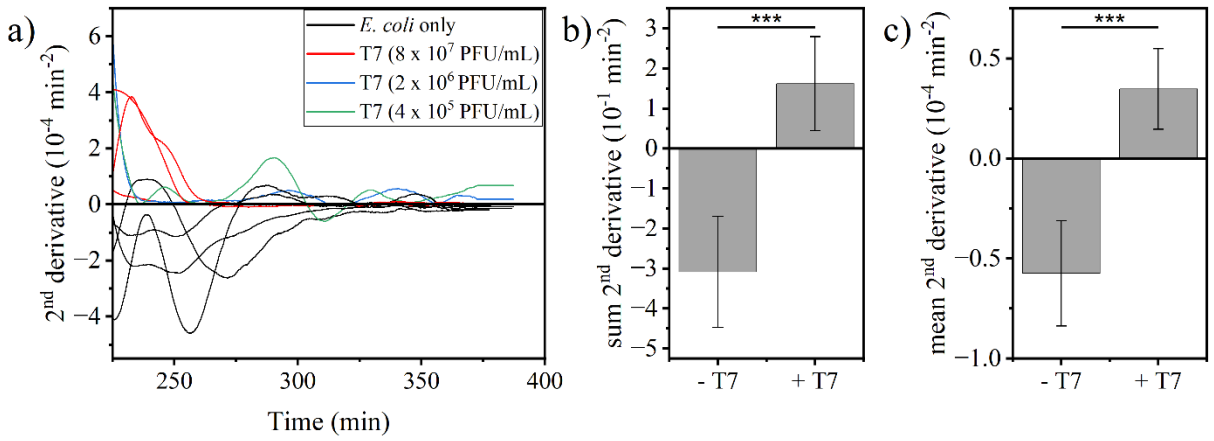

*Figure 46: a) Second derivative of the normalized δD traces shown in Figure 44a after the final flushing with phage-free medium. b,c) Comparison of the sum (b) and the mean values (c) of the curves shown in a) averaged over all E. coli only experiments (-T7) and T7 experiments (all concentrations, +T7). Values are given as the mean ± standard deviation. Statistical significance was determined by two-tailed t-test and is indicated as *** ($p < 0.001$).*

4.1.3 Conclusion

In summary, we have verified the potential of QCM-D to detect bacteriophage infections of surface-adhering bacteria in real-time using T7 infection of *E. coli* as a model system. For ease of use in practical screening campaigns, we have not employed any chemical modifications of the sensors but immobilized the *E. coli* cells directly on the bare gold surface. The absence of any surface modifications also promotes reuse of the sensors in multiple experiments, as organic residues and cell debris can be removed using the standard cleaning procedure described in the Materials and Methods section. Bacterial adsorption, adhesion, and growth at the sensor surface results in complex and overtone-dependent behaviors of the Δ*f* and Δ*D* traces. Various alterations in these behaviors are observed during phage infection and especially upon subsequent lysis of the infected bacterial cells, which are distinctly different from purely non-specific adsorption of non-infectious phages on the exposed sensor surface. This clearly demonstrates the ability of QCM-D to detect and monitor phage infection and lysis of bacterial cells.

By comparing sensor responses to infectious and non-infectious phages, we identified a single measurement parameter, *i.e.*, the difference between the third and the eleventh overtone of the Δ*D* trace, δ*D* = Δ*D*3 - Δ*D*11, which enables a clear distinction between lytic phage infection and non-specific phage adsorption. Most importantly, when normalized to the maximum value observed in the first bacterial growth phase, this parameter appears less sensitive toward sensor-specific differences than the original Δ*D* traces, enabling a more reliable identification of phage-induced bacterial lysis. Using this parameter δ*D*, the complete T7 phage infection process could be followed within four hours, which includes the formation of the *E. coli* films on the sensor surfaces. However, it should be stressed that T7 represents an ideal case with a very short lytic cycle of only 17 min. For other phages with

longer lytic cycles, unambiguous detection of cell lysis will take considerably longer. Future experiments may optimize the experimental conditions and minimize the time to detection for each phage-host combination individually. Nevertheless, the combination of multichannel QCM-D setups with automated liquid-handling systems may nevertheless enable the efficient screening of medium-sized phage collections against target pathogens. Finally, since QCM-D is also able to monitor the removal of biofilms from the sensor surface in real time,(*295, 296*) the presented approach may be further employed to screen phages against bacterial biofilms.

4.1.4 Materials and Methods

Bacteria and Phage Culture

E. coli B (DSM 613) was cultured in LB medium (MP Biomedicals, Germany) at 37°C with constant shaking (222DS, Labnet, USA) overnight. The next day, 3 mL of fresh LB medium was inoculated with 100 µL of the overnight culture of bacteria and was grown till it reached an OD600 value of 0.6-0.7. The bacterial culture at this point was infected with 100 µL of T7 (provided by University of Hohenheim) phage solution and incubated at 37°C with constant shaking. The bacterial cell lysis and subsequent cell death was verified by a drop in the OD value to 0.05 or less. After this, 150 µL of chloroform (Macron Fine Chemicals, USA) was added to the medium and the solution was vortexed briefly for 10 sec, after which it was incubated on ice for 5 min. Then, the supernatant was transferred to a new 15 mL centrifuge tube and centrifuged at 8800 rcf for 5 min. The supernatant containing the phages was transferred to a fresh tube. The phage concentration was quantified using a Water blue double overlay plaque assay as previously described.(*297*) To this end, agar plates were prepared by dissolving 4 g of peptone extract (PanReac AppliChem, Germany), 0.7 g of NaCl (Merck, Germany), and 3 g of agar (PanReac AppliChem, Germany) in 183 mL of molecular biology grade water (VWR, Germany). This mixture was autoclaved at a temperature of 121°C for 15 minutes. After letting the solution cool to 80°C, 12 mL of a 25% glucose (Sigma-Aldrich, Germany) solution was introduced, followed by the addition of 2.7 mL of 0.5 M Na_2HPO_4 and 1.6 mL of aniline blue dye (Thermo Scientific, Germany). Subsequently, the solution was poured into petri dishes and allowed to solidify. In parallel, a 0.7% water agar was prepared and maintained at a temperature of 47°C until further use. The phages were serially diluted 10-fold in phosphate buffer (38.3 mM $Na_2HPO_4 \cdot 2\ H_2O$, 68.4 mM NaCl, 22 mM KH_2PO_4), supplemented with 1 mM $MgSO_4$. A mixture of 300 µL of a bacterial liquid culture of OD ~ 1.0 and 100 µL of phage solution was combined with 4 mL of the water agar and briefly vortexed. The resulting mixture was then poured onto the previously prepared agar plates. The agar was left to solidify, and the plates were incubated at a temperature of 37°C overnight. The following day, the plaques were counted to determine the concentration of the phages.

To test for contaminations in the *E. coli* culture, the bacteria were quadrant streaked on MacConkey (Sigma-Aldrich, Germany) and EMB agar (Oxoid, ThermoFischer Scientific, UK), which are selective media for enteric bacteria. MacConkey agar was prepared by dissolving 5 g of powder in 100 mL of molecular biology grade water. EMB agar was prepared by dissolving 3.75 g powder in 100 mL of molecular biology grade water. Both agars were autoclaved at 121°C for 15 min.

B. subtilis (DSM 5547) was cultivated and grown to exponential phase as described for *E. coli*. For the confirmation of phage solution purity, *B. subtilis* cells were centrifuged for 10 min at 4100 rcf and resuspended in low salt LB (1 % Bacto-Tryptone, 0.5 % yeast extract, 0.5 % NaCl) to an OD of ~10. Subsequently, 40 µL of this culture were transferred to 5 mL tubes and infected with 5 µL of four different phage (Bacillus phage phi29 HER 243-DSM 5546) dilutions (100-fold). To the mixture, 4 mL top agar was added (low salt LB with 0.7% agar food grade, pre-warmed at 50°C), inverted several times and poured onto bottom plates (low salt LB with 1.5% agar, pre-warmed at 37°C). After overnight incubation at 37°C, distinct plaques should be visible with at least one phage dilution. When uniform morphology and purity was confirmed, plaques were used to infect an overnight culture diluted to an OD ~0.2 (1 plaque per 100 ml) and kept for phage propagation at 37°C with shaking overnight. Next day, the culture was centrifuged for 15 min at 4800 rcf to separate the supernatant containing the phages from the bacteria pellet. Additionally, a PES 0.22 µm membrane filter unit (Merck, Germany) was used to remove residual debris and bacterial cells. Finally, the titer was determined via layer plating as described above using a 10-fold phage dilution series. (Produced by Verena Dobretzberger, Molecular Diagnostics, Center for Health and Bioresources, AIT Austrian Institute of Technology GmbH, Vienna, Austria)

Atomic Force Microscopy

Gold-coated QCM-D sensors (5 MHz 14 mm Cr/Au, Quartz Pro, Sweden) from three different batches were rinsed with ethanol (Berkel AHK GmbH & Co. KG, Germany) and HPLC grade water (Roth, Germany) and dried with argon. The cleaned samples were imaged in air using a Bruker Dimension Icon in ScanAsyst Peak-Force tapping mode with ScanAsyst air cantilevers (Bruker, Germany). Images were recorded at 1024 x 1024 pixels with a scan size of 5 µm². Gwyddion(*298*) was used to process the images and calculate the rms surface roughness S_q.

Preparation of QCM-D Flow Cells and Sensors

The flow cells and the inlet pipes of the QCM-D system (E4, Biolin Scientific, Sweden) were incubated in 2 % Hellmanex (Hellma GmbH, Germany) for 2 h. Afterwards, the flow cells were rinsed with 99 % ethanol and HPLC grade water and dried with ultrapure argon. The gold-coated QCM-D sensors were

cleaned in RCA-1 solution (1:1:5 in volume 35% NH_4OH, 25% H_2O_2, H_2O- Stockmeier Chemie, Germany) at 75°C for 1 min. After cleaning, the sensors were rinsed with HPLC grade water and dried with argon.

QCM-D Experiments

All buffers and solutions were autoclaved prior to the experiments. *E. coli B* was cultured overnight in LB medium at 37°C with constant shaking. The next day, 20 mL of fresh LB medium was inoculated with 500 µL of the overnight *E. coli* B culture. The bacteria were grown to an OD600 value of 0.6 (mid log phase culture). The T7 phages were diluted in LB medium to three different concentrations of 8 x 10^7 PFU/mL, 2 x 10^6 PFU/mL, and 4 x 10^5 PFU/mL, respectively. QCM-D measurements were conducted at 37°C, either in static mode or with a constant flow rate of 30 µL/min. For the sample flow cell, PBS was pumped in for 20 min to obtain a constant baseline, after which bacteria in LB medium were pumped in for 30 min to adsorb to the sensor surface. Afterwards, the flow cell was flushed for 15 mins with bacteria-free medium to remove unattached bacteria. Then the flow was stopped, and the bacteria were left to grow under static conditions for 2 h. Phages in LB medium were then pumped in for 20 min, followed by another medium flush for 15 min to remove excess phages not attached to the bacteria. The flow was then stopped again, and the sample incubated for 3 h under static conditions. In order to evaluate the behavior of the adsorbed bacteria in the absence of phages, one control used phage-free LB medium instead of phage-containing medium. To evaluate phage adsorption on the gold surface of the sensor, an additional control used bacteria-free medium instead of bacteria-containing medium.

The QCM-D data was processed using D-find software (Biolin Scientific, Sweden) and plotted using Origin Pro 2021 (OriginLab, USA).

Scanning Electron Microscopy

After the QCM-D experiments, the sensors were incubated in 2.5 % glutaraldehyde in PBS overnight. Subsequently, the sensors were dehydrated by incubating them sequentially in ethanol dilutions of 20 %, 40 %, 60 %, 80 % and 100 % each for 10 min. After the last incubation step, the sensors were dried in air their surfaces sputter-coated (SCD 500, Leica Microsystems, Germany) with a 3 nm thick gold alloy (80 % Au + 20 % Pd). Finally, the sensors were examined using a NEON 40 SEM (Zeiss, Germany) at various magnifications (1k, 3k, 10k, 15k, 25k and 40k) with a 5 kV electron beam.

4.2 Effect of Inactivation Methods on Zika virus Adsorption on Different Model Surfaces

4.2.1 Introduction

In research, biologically inactivating pathogenic viruses is often a necessary and important precursor for being able to work with virus particles in laboratories lacking the appropriate biosafety certification for potentially dangerous organisms.(*299*) Inactivation of viruses can be performed using various chemical and physical methods or a combination of both. The most common methods of inactivation used in the laboratory setting and in vaccine manufacturing include exposure to high temperatures, chemicals or radiation. For vaccine production in particular, heat-based inactivation(*300*) and chemical treatment with either beta-Propiolactone (BPL)(*301*) or formaldehyde(*302*) are the most widely used methods, however newer methods involving hydrogen peroxide (H_2O_2)(*303*) treatment or irradiation with low-energy electrons(*304*) are also seen as emerging technologies with the potential for being less disruptive to the virus structure. For chemical and radiation inactivation methods, the respective treatments are specifically targeted towards the pathogen genome, which are either fragmented or otherwise modified to render it incapable of replicating within the host cell. In the case of BPL, genomic damage is proposed to occur through alkylation of different nucleobases, specifically the purines, with guanine being the most affected at low concentrations of BPL. This alkylation renders the molecules acidic following subsequent hydrolysis. At higher concentration of BPL, cleavage of imidazole rings and pyrimidines also occurs.(*305, 306*) In contrast, in the case of more recently introduced H_2O_2 treatment, the genomic damage is caused due to hydroxyl radicals. These radicals attack the carbon double bonds in the nucleosides, generating carbon radicals. This oxidation process ultimately leads to single or double strands breaks in the genome.(*307*) Similarly, UV-, gamma- and electron irradiation are known to induce crosslinking and/or cleavage of bonds in RNA and DNA, thus interfering with the function of enzymes such as polymerases or reverse transcriptase's, used in the process of genomic replication.(*308–310*) A study conducted on influenza demonstrated that BPL specifically affects amino acids in viral surface and other proteins through acylation or alkylation, resulting in a mass increase of 72 Da or 144 Da for each modified amino acid. Comparatively, proteins undergo more extensive modifications than DNA. However, these modifications are highly dependent on factors such as BPL concentration, the pH of the mixture, and the type of buffer used.(*305*) Notably, at pH 7 and 22°C, methionine, cystine, and histidine react completely with BPL, whereas proline and lysine exhibit significantly lower reactivity with respect to individual amino acids.(*311*)

These inactivation methods can induce structural and physiochemical changes to viral particles as explained above, which may significantly affect their interactions and behavior with cells or inorganic

surfaces. Understanding these alterations is critical for designing effective vaccines and antiviral materials. Surface interactions of viruses are largely governed by the interplay of electrostatic, hydrophobic, van der Waals and hydrogen bonding. The Zika virus (ZIKV), for instance, exhibits predominantly hydrophilic regions and few hydrophobic regions on its surface with a distribution of positive and negative charges.(*312–314*)

In this study, we investigated the impact of two widely used inactivation methods, β-propiolactone (BPL) and hydrogen peroxide (H_2O_2), on the surface properties and adsorption behavior of Zika virus (ZIKV) using QCM-D and AFM. We analyzed how active and inactivated ZIKV particles interact with self-assembled monolayers (SAMs) of varying surface chemistries. While H_2O_2-inactivated ZIKV retained adsorption behavior similar to active virus, suggesting minimal alterations to surface properties, BPL-inactivated ZIKV exhibited significant structural changes, increased aggregation on hydrophilic surfaces, and enhanced interaction with hydrophobic surfaces, indicating reduced colloidal stability.

4.2.2 Results and Discussion

QCM-D and AFM

To analyze the effect of the different inactivating treatments on the surface properties, we quantified the adsorption of ZIKV before and after inactivation at organic self-assembled monolayers (SAMs) with different surface properties. This was done in situ and in real-time using quartz crystal microbalance with dissipation monitoring (QCM-D). Figure 47a shows the time course of adsorption of active ZIKV at four different SAMs. In all four cases, a rapid increase in adsorbed mass is observed upon ZIKV injection, followed by slow saturation until a more or less static plateau is reached. The absolute value of adsorbed mass in this plateau phase differs notably for the four SAMs. The lowest value is observed for the hydrophobic CH_3-terminated SAM, whereas the three hydrophilic SAMs generate larger values. This is not too surprising considering that the ZIKV surface is predominantly hydrophilic. However, there are also differences between the hydrophilic SAMs. Among the three, the negatively charged COO^--terminated SAM shows the lowest value of adsorbed mass, which was to be expected based on the negative zeta potential of ZIKV. Surprisingly, however, ZIKV adsorption at the positively charged NH_3^+-terminated SAM is only marginally stronger than at this negatively charged SAM, even though electrostatic repulsion is now replaced by electrostatic attraction. This can be rationalized by considering two factors. First, the zeta potential only provides net charge but neglects that the ZIKV surface exhibits both negative as well as positive charges, so that there will always be an interplay between electrostatic repulsion and electrostatic attraction. A change in the SAM's charge state will thus result only in small variations in the relative contributions of attractive and repulsive interactions.

Second, electrostatic interactions will be relatively weak under the employed ionic conditions as the Debye length in PBS is only about 0.7 nm(*271*) and thus about 50 times smaller than a ZIKV particle. Nevertheless, electrostatic interactions cannot be neglected completely, as strongest ZIKV adsorption is observed on the uncharged hydrophilic OH-terminated SAM. Here, adsorption is not hindered by electrostatic repulsion at all and purely driven by hydrophilic interactions.

We have complemented the QCM-D experiments with atomic force microscopy (AFM) investigations of the adsorbate structures. For this, template-stripped gold was used as the substrate, as this provides a smoother surface better suited for AFM investigations of adsorbed nanostructures with sizes below 100 nm.(*187*) As can be seen in Figure 47b, adsorption at the three hydrophilic SAMs occurs mostly in the form of aggregates and not of single ZIKV particles. For the hydrophobic CH_3-terminated SAM, however, adsorbate morphology is markedly different and appears more homogeneous, while at the same time displaying some meandering structures reminiscent of phase separation. Since no individual particles can be identified in these adsorbate films, we believe that they are the result of ZIKV disintegration. Strong hydrophobic interactions with the SAM surface may stimulate the E and M proteins to expose their hydrophobic transmembrane domains, which may trigger the complete disassembly of the particle and the release of lipids from the membrane that can then form monolayer patches on the SAM surface.

As can be seen in Figure 47c, ZIKV inactivation with H_2O_2 does not result in strong changes in the interaction with the different SAMs. It is important to note that after virus production and titer estimation, the inactivation procedure was performed, followed by dialysis of the sample (see Materials and Methods). Since the inactivated virus particles are no longer infectious, it is not possible to determine the viral titer. For this reason, the absolute adsorption values in terms of mass can't be compared as the titer of the inactivated samples is unknown in comparison to active viral samples (2 x 10^6 PFU/mL). Strongest and weakest adsorption is still observed for the OH- and the CH_3-terminated SAM, while the charged SAMs show intermediate and very similar performance. Only the AFM images in Figure 47d show some moderate differences in adsorbate morphology compared to the active virus, i.e., more pronounced aggregation on the hydrophilic SAMs and stronger phase separation on the hydrophobic SAM, with the resulting meanders having smaller heights. While the latter might hint at a reduced ZIKV stability, the differences are not pronounced enough to exclude sample-to-sample variation as the ultimate cause.

In contrast, BPL inactivation results in pronounced changes in ZIKV adsorption behavior. The QCM-D data in Figure 47e reveals strongest adsorption at the hydrophobic SAM while weakest adsorption is observed on positively charged NH_3^+-terminated SAM, with the negatively charged COO^--terminated

SAM being second to the hydrophobic SAM. At first glance, the latter observations would indicate an increase in positive surface charges. AFM, on the other hand, reveals the presence of very large aggregates on the three hydrophilic surfaces while the hydrophobic surface again shows a pronounced phase separation. Therefore, we assume that the observed alterations in ZIKV adsorption behavior rather result from BPL-induced differences in the structural and colloidal stability of the ZIKV particles.

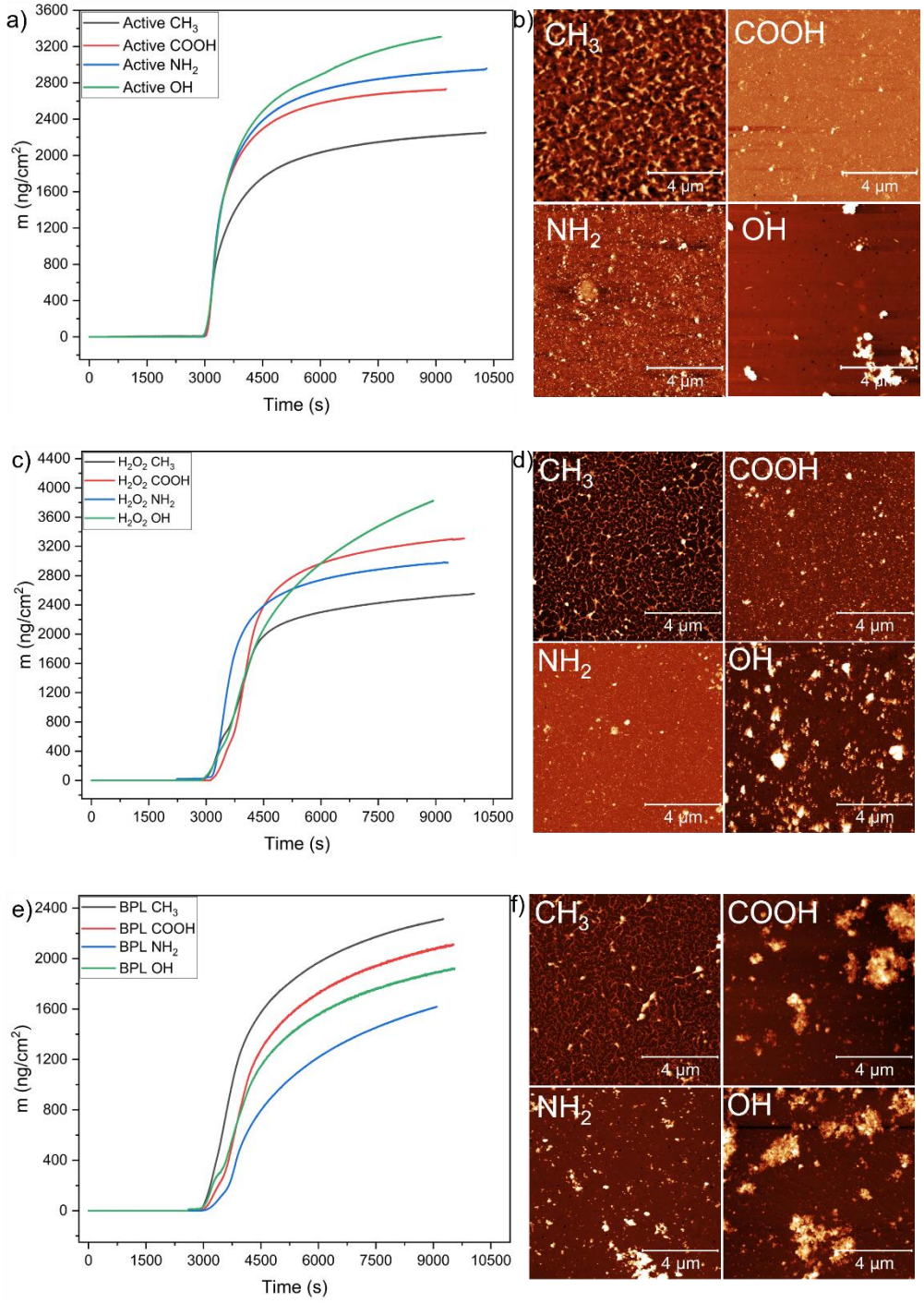

Figure 47: a) Kinetics of mass adsorption as a function of time for surface functionalized with different SAM for active viruses. b) AFM images of the functionalized surface, showing morphological differences in adsorption behavior based on the SAM for active viruses. c) Kinetics of mass adsorption as a function of time for surface functionalized with different SAM for H_2O_2 inactivated viruses. d) AFM images of the functionalized surface,

showing morphological differences in adsorption behavior based on the SAM for H_2O_2 inactivated viruses. e) Kinetics of mass adsorption as a function of time for surface functionalized with different SAM for BPL inactivated viruses. f) AFM images of the functionalized surface, showing morphological differences in adsorption behavior based on the SAM for the BPL inactivated viruses.

4.2.3 Conclusion

In summary, we investigated the effect of two widely used viral inactivation methods, i.e., BPL and H_2O_2 on the adsorption behavior of ZIKV at soli-liquid interfaces. Using QCM-D and AFM, the interaction of active and inactivated ZIKV particles with SAMs featuring different functionalities was analyzed.

It was found that viral inactivation can significantly alter the absorption properties of the ZIKV due to structural and physiochemical changes induced by the inactivation treatments. The H_2O_2 inactivated ZIKV exhibited adsorption behavior similar to that of the active virus, suggesting that the surface properties of the virus remained largely intact after treatment. However, the BPL inactivated ZIKV displayed markedly different adsorption trends, including increased aggregation on hydrophilic surfaces and enhanced interaction with hydrophobic surface, suggesting significant structural alterations and reduced colloidal stability. Furthermore, studying the impact of various inactivation methods at the molecular level is crucial for understanding their mechanisms of action. Our ongoing research focuses on investigating these molecular changes, including alterations in the zeta potential and size (using DLS) of whole viruses following inactivation. Additionally, we aim to examine the unfolding of viral proteins, both at the whole-virus level and for individual surface proteins, such as the E-protein in the case of ZIKV, using nano-Differential Scanning Fluorimetry (nano-DSF). We will further employ infrared (IR) spectroscopy to analyze changes in functional groups that play a key role in virus interactions with target surfaces or cells post-inactivation. These observations underscore the importance of understanding how different inactivation methods impact viral surface properties, particularly in applications involving virus-material interactions such as vaccines, antiviral coatings and biosensors

4.2.4 Materials and Methods

Virus inactivation

To inactivate ZIKV (Performed by research group of PD Dr. Sebastian Ulbert, Fraunhofer IZI, Leipzig, Germany) two different chemicals, in particular beta-propiolactone (BPL) and hydrogen peroxide (H_2O_2), were used. The inactivation of ZIKV (2 x 10^6 PFU/mL) by 0.3% BPL was done at 22°C overnight followed by a hydrolysis for 2 h at 37°C and for the other method overnight incubation with 0.3% H_2O_2 at 37°C was applied to inactivate ZIKV. After inactivation experiments, dialyses against PBS were performed and samples were stored in aliquots at -80°C until use.

Cleaning of Flow cells

QCM-D flow cells were cleaned in 2% Hellmanx (Hellma GmbH, Germany), by incubating for 1 h in the solution. Post incubation the cells were cleaned with ethanol and HPLC grade water (Carl Roth, Germany) and air dried with argon.

SAM assembly

The gold coated QCM sensors - 5MHz 14 mm Cr/Au (Quartzpro, Sweden) were cleaned in RCA-1 solution (1:1:5 in volume 35% NH_4OH/25% H_2O_2/H_2O) at 75 °C for 1 min. Post cleaning the crystal were rinsed with HPLC grade water and air dried with argon. The self-assembled monolayers NH_2, OH, COOH and CH_3 were prepared using 11-amino-1-undecanethiol hydrochloride, 11-mercapto-1-undecanol, 11-mercaptoundecanoic acid and 1- octadecanethiol respectively in ethanol at a concentration of 1 mM. The pre- cleaned crystals were incubated in this solution by immersion for 24 h. Post incubation the crystals were rinsed with HPLC grade water and air dried with argon.(*278*)

Adsorption studies by QCM-D

The inactivated and active virus adsorption was monitored using Q-sense E4 (Biolin scientific, Sweden). The measurements were carried out at room temperature with flow rate of 10 µL/min using a peristaltic pump (IPC4, Ismatech, Germany). Initial baseline was established by flushing PBS for 30 min, following which the virus samples were pumped for 40 min, post which the pump was stopped, and the measurement was conducted in static conditions up to the point where the frequency and dissipation curves were stabilized. The obtained data was processed in D-find software (Biolin Scientific, Sweden) and was modelled using D-find Smart fit model. After modelling, the data points were extracted out of the software and were plotted using Origin Pro 2021.

Atomic Force Microscopy

Template stripped gold substrates were rinsed using ethanol prior to use. The virus sample (2 x 10^6 PFU/mL- provided by Fraunhofer IZI, Leipzig, Germany) were diluted in a ratio of 1:1 with PBS (Sigma Aldrich, Germany). 200 µL of the prepared virus solution was carefully dropped on top of sample and was incubated for 150 min at room temperature. Post incubation the sample was washed with HPLC grade water and dried using ultrapure argon. JPK 2 AFM (Bruker Nano GmbH, Germany) was used to image the substrate using NSC18/Al Bs (MikroMasch, Germany) cantilevers in tapping mode. The images were recorded at 10 μm^2 in 1024 pixels for inactivated samples and 512 pixels for the active samples. The images obtained were processed with Gwyddion for adjusting the respective height scales.

Chapter 5: Conclusion and Outlook

The whole research sets out to explore how biological entities interact with surfaces at the nanoscale, combining the fields of DNA nanotechnology, microbiology, and interface science. By using advanced imaging techniques such as AFM, it was uncovered that DNA structures self-organize based on specific molecular stacking interactions. Additionally, sensing methods like Quartz Crystal Microbalance with Dissipation monitoring (QCM-D) was utilized and it was uncovered that dissipation as a parameter can be used to study bacterial adhesion and the dynamics of subsequent phage infections, and it was also uncovered that viruses exhibit unique adsorption behavior depending on the inactivation procedure and surface chemistry.

One of the key discoveries in this work was the controlled formation of DNA origami lattices on different surfaces, particularly mica and SiO_2. By fine-tuning ionic conditions like cation and monovalent ion concentrations and surface chemistry, it was demonstrated that highly ordered nanostructures could be achieved, revealing the delicate balance between electrostatic forces and molecular mobility. These findings added in the groundwork for utilizing DNA as a fundamental building block for nanoscale patterning and self-assembly into functional devices or molecular scaffolds for precision medicine.

Another major focus was on bacterial adhesion and phage infection dynamics, where QCM-D was used to monitor in real time how phages attack bacteria on surfaces. It was found that dissipation shifts (ΔD), rather than frequency (Δf), provided the most reliable signal for tracking the lysis process of bacteria. This breakthrough has direct applications in phage therapy. The ability to track phage infection dynamics in real-time holds a future in screening most effective phages against resistant bacteria and help in developing personalized antimicrobial treatments.

In the final part of this research, it was examined how the Zika virus interacts with SAMs, uncovering how different inactivation methods impact viral adhesion. Understanding how viruses behave with modifications and its interactions with various surfaces help in vaccine development strategies also with implications in developing future antiviral coatings.

At the very core of this thesis, the research highlights the power of interdisciplinary science. By bringing together various scientific fields, it was established that biological molecules and organisms interact with surfaces in complex and dynamic ways, leading to a deeper understanding of these interactions. Scientific research is often about making small discoveries that, over time, contribute to big changes. This work is one step in a long journey- one that leads to smarter materials, better diagnostics and innovative solutions to pressing biological challenges.

References

1. Soukup, G. A. Nucleic Acids: General Properties. In: *Encyclopedia of Life Sciences*; Wiley, 2005. DOI: 10.1038/npg.els.0001335.
2. WATSON, J. D.; CRICK, F. H. Molecular structure of nucleic acids; a structure for deoxyribose nucleic acid. *Nature* **1953,** *171* (4356), 737–738. DOI: 10.1038/171737a0.
3. Ghosh, A.; Bansal, M. A glossary of DNA structures from A to Z. *Acta Crystallogr D Biol Crystallogr* **2003,** *59* (Pt 4), 620–626. DOI: 10.1107/S0907444903003251.
4. Rich, A. Z-DNA. In: *Brenner's Encyclopedia of Genetics*; Elsevier, 2013, pp 392–395. DOI: 10.1016/B978-0-12-374984-0.01665-X.
5. Roy, R.; Chakraborty, P.; Chatterjee, A.; Sarkar, J. Comparative review on left-handed Z-DNA. *Front Biosci* **2021,** *26* (5), 29–35. DOI: 10.52586/4922.
6. Lodish, H. F. *Molecular cell biology*, 4th ed.; W.H. Freeman, 2000.
7. Neidle, S. Beyond the double helix: DNA structural diversity and the PDB. *J. Biol. Chem.* **2021,** *296*, 100553. DOI: 10.1016/j.jbc.2021.100553.
8. Calladine, C. R. *Understanding DNA*: *The molecule & how it works*, 3rd ed.; Elsevier Academic Press, 2004.
9. Parker, N.; Schneegurt, M.; Tu, A. *Microbiology by OpenStax;* Open Stax Textbooks, 2023.
10. Travers, A.; Muskhelishvili, G. DNA structure and function. *The FEBS journal* **2015,** *282* (12), 2279–2295. DOI: 10.1111/febs.13307.
11. Lehninger, A. L.; Nelson, D. L.; Cox, M. M. *Lehninger principles of biochemistry*, 4th ed.; W.H. Freeman, 2005.
12. Holliday, R. A mechanism for gene conversion in fungi. *Genet. Res.* **1964,** *5* (2), 282–304. DOI: 10.1017/S0016672300001233.
13. Seeman, N. C. Nucleic acid junctions and lattices. *Journal of theoretical biology* **1982,** *99* (2), 237–247. DOI: 10.1016/0022-5193(82)90002-9.
14. Tørring, T.; Gothelf, K. V. DNA nanotechnology: a curiosity or a promising technology? *F1000prime reports* **2013,** *5*, 14. DOI: 10.12703/P5-14.
15. Rothemund, P. W. K. Folding DNA to create nanoscale shapes and patterns. *Nature* **2006,** *440* (7082), 297–302. DOI: 10.1038/nature04586.

16. Castro, C. E.; Kilchherr, F.; Kim, D.-N.; Shiao, E. L.; Wauer, T.; Wortmann, P.; Bathe, M.; Dietz, H. A primer to scaffolded DNA origami. *Nat. Methods.* **2011,** *8* (3), 221–229. DOI: 10.1038/nmeth.1570.

17. Douglas, S. M.; Dietz, H.; Liedl, T.; Högberg, B.; Graf, F.; Shih, W. M. Self-assembly of DNA into nanoscale three-dimensional shapes. *Nature* **2009,** *459* (7245), 414–418. DOI: 10.1038/nature08016.

18. Sobczak, J.-P. J.; Martin, T. G.; Gerling, T.; Dietz, H. Rapid folding of DNA into nanoscale shapes at constant temperature. *Science* **2012,** *338* (6113), 1458–1461. DOI: 10.1126/science.1229919.

19. Shaw, A.; Lundin, V.; Petrova, E.; Fördős, F.; Benson, E.; Al-Amin, A.; Herland, A.; Blokzijl, A.; Högberg, B.; Teixeira, A. I. Spatial control of membrane receptor function using ligand nanocalipers. *Nat. Methods* **2014,** *11* (8), 841–846. DOI: 10.1038/nmeth.3025.

20. Aghebat Rafat, A.; Sagredo, S.; Thalhammer, M.; Simmel, F. C. Barcoded DNA origami structures for multiplexed optimization and enrichment of DNA-based protein-binding cavities. *Nat. Chem.* **2020,** *12* (9), 852–859. DOI: 10.1038/s41557-020-0504-6.

21. Kuzyk, A.; Schreiber, R.; Fan, Z.; Pardatscher, G.; Roller, E.-M.; Högele, A.; Simmel, F. C.; Govorov, A. O.; Liedl, T. DNA-based self-assembly of chiral plasmonic nanostructures with tailored optical response. *Nature* **2012,** *483* (7389), 311–314. DOI: 10.1038/nature10889.

22. Kuzyk, A.; Urban, M. J.; Idili, A.; Ricci, F.; Liu, N. Selective control of reconfigurable chiral plasmonic metamolecules. *Sci. Adv.* **2017,** *3* (4), e1602803. DOI: 10.1126/sciadv.1602803.

23. Diagne, C. T.; Brun, C.; Gasparutto, D.; Baillin, X.; Tiron, R. DNA Origami Mask for Sub-Ten-Nanometer Lithography. *ACS Nano* **2016,** *10* (7), 6458–6463. DOI: 10.1021/acsnano.6b00413.

24. Zhang, Q.; Jiang, Q.; Li, N.; Dai, L.; Liu, Q.; Song, L.; Wang, J.; Li, Y.; Tian, J.; Ding, B.; Du, Y. DNA origami as an in vivo drug delivery vehicle for cancer therapy. *ACS Nano* **2014,** *8* (7), 6633–6643. DOI: 10.1021/nn502058j.

25. Ouyang, X.; Li, J.; Liu, H.; Zhao, B.; Yan, J.; Ma, Y.; Xiao, S.; Song, S.; Huang, Q.; Chao, J.; Fan, C. Rolling circle amplification-based DNA origami nanostructrures for intracellular delivery of immunostimulatory drugs. *Small* **2013,** *9* (18), 3082–3087. DOI: 10.1002/smll.201300458.

26. Langecker, M.; Arnaut, V.; Martin, T. G.; List, J.; Renner, S.; Mayer, M.; Dietz, H.; Simmel, F. C. Synthetic lipid membrane channels formed by designed DNA nanostructures. *Science* **2012,** *338* (6109), 932–936. DOI: 10.1126/science.1225624.

27. Ke, Y.; Meyer, T.; Shih, W. M.; Bellot, G. Regulation at a distance of biomolecular interactions using a DNA origami nanoactuator. *Nat. Commun.* **2016,** *7*, 10935. DOI: 10.1038/ncomms10935.

28. Mao, C.; Sun, W.; Seeman, N. C. Designed Two-Dimensional DNA Holliday Junction Arrays Visualized by Atomic Force Microscopy. *J. Am. Chem. Soc.* **1999,** *121* (23), 5437–5443. DOI: 10.1021/ja9900398.

29. Zheng, J.; Constantinou, P. E.; Micheel, C.; Alivisatos, A. P.; Kiehl, R. A.; Seeman, N. C. Two-dimensional nanoparticle arrays show the organizational power of robust DNA motifs. *Nano Lett.* **2006,** *6* (7), 1502–1504. DOI: 10.1021/nl060994c.

30. Wang, X.; Jun, H.; Bathe, M. Programming 2D Supramolecular Assemblies with Wireframe DNA Origami. *J. Am. Chem. Soc.* **2022,** *144* (10), 4403–4409. DOI: 10.1021/jacs.1c11332.

31. Tikhomirov, G.; Petersen, P.; Qian, L. Fractal assembly of micrometre-scale DNA origami arrays with arbitrary patterns. *Nature* **2017,** *552* (7683), 67–71. DOI: 10.1038/nature24655.

32. Woo, S.; Rothemund, P. W. K. Self-assembly of two-dimensional DNA origami lattices using cation-controlled surface diffusion. *Nat. Commun.* **2014,** *5*, 4889. DOI: 10.1038/ncomms5889.

33. Tapio, K.; Kielar, C.; Parikka, J. M.; Keller, A.; Järvinen, H.; Fahmy, K.; Toppari, J. J. Large-Scale Formation of DNA Origami Lattices on Silicon. *Chem. Mater.* **2023,** *35* (5), 1961–1971. DOI: 10.1021/acs.chemmater.2c03190.

34. Xin, Y.; Martinez Rivadeneira, S.; Grundmeier, G.; Castro, M.; Keller, A. Self-assembly of highly ordered DNA origami lattices at solid-liquid interfaces by controlling cation binding and exchange. *Nano Res.* **2020,** *13* (11), 3142–3150. DOI: 10.1007/s12274-020-2985-4.

35. Sato, Y.; Endo, M.; Morita, M.; Takinoue, M.; Sugiyama, H.; Murata, S.; Nomura, S. M.; Suzuki, Y. Environment-Dependent Self-Assembly of DNA Origami Lattices on Phase-Separated Lipid Membranes. *Adv. Mater. Interfaces* **2018,** *5* (14). DOI: 10.1002/admi.201800437.

36. Suzuki, Y.; Endo, M.; Sugiyama, H. Lipid-bilayer-assisted two-dimensional self-assembly of DNA origami nanostructures. *Nat. Commun.* **2015,** *6*, 8052. DOI: 10.1038/ncomms9052.

37. Yonamine, Y.; Cervantes-Salguero, K.; Minami, K.; Kawamata, I.; Nakanishi, W.; Hill, J. P.; Murata, S.; Ariga, K. Supramolecular 1-D polymerization of DNA origami through a dynamic process at the 2-dimensionally confined air-water interface. *PCCP* **2016,** *18* (18), 12576–12581. DOI: 10.1039/C6CP01586G.

38. Kielar, C.; Ramakrishnan, S.; Fricke, S.; Grundmeier, G.; Keller, A. Dynamics of DNA Origami Lattice Formation at Solid-Liquid Interfaces. *ACS Appl. Mater. Interfaces* **2018,** *10* (51), 44844–44853. DOI: 10.1021/acsami.8b16047.

39. Kocabey, S.; Kempter, S.; List, J.; Xing, Y.; Bae, W.; Schiffels, D.; Shih, W. M.; Simmel, F. C.; Liedl, T. Membrane-assisted growth of DNA origami nanostructure arrays. *ACS Nano* **2015,** *9* (4), 3530–3539. DOI: 10.1021/acsnano.5b00161.

40. Zhang, T.; Hartl, C.; Frank, K.; Heuer-Jungemann, A.; Fischer, S.; Nickels, P. C.; Nickel, B.; Liedl, T. 3D DNA Origami Crystals. *Adv. Mater.* **2018,** *30* (28), e1800273. DOI: 10.1002/adma.201800273.

41. Wang, Y.; Yan, X.; Zhou, Z.; Ma, N.; Tian, Y. pH-Induced Symmetry Conversion of DNA Origami Lattices. *Angew. Chem. Int. Ed. Engl.* **2022,** *61* (40), e202208290. DOI: 10.1002/anie.202208290.

42. Yang, Y.; Endo, M.; Hidaka, K.; Sugiyama, H. Photo-controllable DNA origami nanostructures assembling into predesigned multiorientational patterns. *J. Am. Chem. Soc.* **2012,** *134* (51), 20645–20653. DOI: 10.1021/ja307785r.

43. Julin, S.; Keller, A.; Linko, V. Dynamics of DNA Origami Lattices. *Bioconjugate Chem.* **2023,** *34* (1), 18–29. DOI: 10.1021/acs.bioconjchem.2c00359.

44. Ramakrishnan, S.; Subramaniam, S.; Stewart, A. F.; Grundmeier, G.; Keller, A. Regular Nanoscale Protein Patterns via Directed Adsorption through Self-Assembled DNA Origami Masks. *ACS Appl. Mater. Interfaces* **2016,** *8* (45), 31239–31247. DOI: 10.1021/acsami.6b10535.

45. Julin, S.; Nummelin, S.; Kostiainen, M. A.; Linko, V. DNA nanostructure-directed assembly of metal nanoparticle superlattices. *J. Nanoparticle Res.* **2018,** *20* (5), 119. DOI: 10.1007/s11051-018-4225-3.

46. Julin, S.; Korpi, A.; Nonappa; Shen, B.; Liljeström, V.; Ikkala, O.; Keller, A.; Linko, V.; Kostiainen, M. A. DNA origami directed 3D nanoparticle superlattice via electrostatic assembly. *Nanoscale* **2019,** *11* (10), 4546–4551. DOI: 10.1039/C8NR09844A.

47. Volland, J.-M.; Gonzalez-Rizzo, S.; Gros, O.; Tyml, T.; Ivanova, N.; Schulz, F.; Goudeau, D.; Elisabeth, N. H.; Nath, N.; Udwary, D.; Malmstrom, R. R.; Guidi-Rontani, C.; Bolte-Kluge, S.; Davies, K. M.; Jean, M. R.; Mansot, J.-L.; Mouncey, N. J.; Angert, E. R.; Woyke, T.; Date, S. V. A centimeter-long bacterium with DNA contained in metabolically active, membrane-bound organelles. *Science* **2022,** *376* (6600), 1453–1458. DOI: 10.1126/science.abb3634.

48. Zhuang, X.-Y.; Lo, C.-J. Construction and Loss of Bacterial Flagellar Filaments. *Biomolecules* **2020,** *10* (11). DOI: 10.3390/biom10111528.

49. Simões, M.; Simões, L. C.; Vieira, M. J. A review of current and emergent biofilm control strategies. *LWT - Food Science and Technology* **2010,** *43* (4), 573–583. DOI: 10.1016/j.lwt.2009.12.008.

50. Baron, S., Ed. *Medical Microbiology*, 4th, 1996.

51. Madigan, M. T.; Bender, K. S.; Buckley, D. H.; Sattley, W. M.; Stahl, D. A. *Brock biology of microorganisms*, Sixteenth edition; Pearson Education, 2021.

52. Coico, R. Gram staining. *Curr. Protoc. Microbiol.* **2005,** *Appendix 3*, Appendix 3C. DOI: 10.1002/9780471729259.mca03cs00.

53. Vijayaram, S.; Sun, Y.-Z.; Zuorro, A.; Ghafarifarsani, H.; van Doan, H.; Hoseinifar, S. H. Bioactive immunostimulants as health-promoting feed additives in aquaculture: A review. *Fish & Shellfish Immunol.* **2022,** *130*, 294–308. DOI: 10.1016/j.fsi.2022.09.011.

54. Artasensi, A.; Mazzotta, S.; Fumagalli, L. Back to Basics: Choosing the Appropriate Surface Disinfectant. *Antibiotics* **2021,** *10* (6). DOI: 10.3390/antibiotics10060613.

55. Costerton, J. W.; Ingram, J. M.; Cheng, K. J. Structure and function of the cell envelope of gram-negative bacteria. *Bacteriol. Rev.* **1974,** *38* (1), 87–110. DOI: 10.1128/br.38.1.87-110.1974.

56. Ghuysen, J. M.; Hackenbeck, R. *Bacterial cell wall*; New comprehensive biochemistry; Vol. 27; Elsevier, 1994.

57. Flemming, H.-C.; Wingender, J. The biofilm matrix. *Nat. Rev. Microbiol.* **2010,** *8* (9), 623–633. DOI: 10.1038/nrmicro2415.

58. Mahto, K. U.; Vandana; Priyadarshanee, M.; Samantaray, D. P.; Das, S. Bacterial biofilm and extracellular polymeric substances in the treatment of environmental pollutants: Beyond the protective role in survivability. *J. Clean. Prod.* **2022,** *379*, 134759. DOI: 10.1016/j.jclepro.2022.134759.

59. Costerton, J. W.; Stewart, P. S.; Greenberg, E. P. Bacterial biofilms: a common cause of persistent infections. *Science* **1999,** *284* (5418), 1318–1322. DOI: 10.1126/science.284.5418.1318.

60. Hall-Stoodley, L.; Costerton, J. W.; Stoodley, P. Bacterial biofilms: from the natural environment to infectious diseases. *Nat. Rev. Microbiol.* **2004,** *2* (2), 95–108. DOI: 10.1038/nrmicro821.

61. O'Toole, G.; Kaplan, H. B.; Kolter, R. Biofilm formation as microbial development. *Annu. Rev. Microbiol.* **2000,** *54*, 49–79. DOI: 10.1146/annurev.micro.54.1.49.

62. Rather, M. A.; Gupta, K.; Mandal, M. Microbial biofilm: formation, architecture, antibiotic resistance, and control strategies. *Braz. J. Microbiol.* **2021,** *52* (4), 1701–1718. DOI: 10.1007/s42770-021-00624-x.

63. Sauer, K.; Stoodley, P.; Goeres, D. M.; Hall-Stoodley, L.; Burmølle, M.; Stewart, P. S.; Bjarnsholt, T. The biofilm life cycle: expanding the conceptual model of biofilm formation. *Nat. Rev. Microbiol.* **2022,** *20* (10), 608–620. DOI: 10.1038/s41579-022-00767-0.

64. Zheng, S.; Bawazir, M.; Dhall, A.; Kim, H.-E.; Le He; Heo, J.; Hwang, G. Implication of Surface Properties, Bacterial Motility, and Hydrodynamic Conditions on Bacterial Surface Sensing and Their Initial Adhesion. *Front. Bioeng. Biotechnol* **2021,** *9*, 643722. DOI: 10.3389/fbioe.2021.643722.

65. Shrout, J. D.; Chopp, D. L.; Just, C. L.; Hentzer, M.; Givskov, M.; Parsek, M. R. The impact of quorum sensing and swarming motility on Pseudomonas aeruginosa biofilm formation is nutritionally conditional. *Mol. Microbiol.* **2006,** *62* (5), 1264–1277. DOI: 10.1111/j.1365-2958.2006.05421.x.

66. Davies, D. G.; Parsek, M. R.; Pearson, J. P.; Iglewski, B. H.; Costerton, J. W.; Greenberg, E. P. The involvement of cell-to-cell signals in the development of a bacterial biofilm. *Science* **1998,** *280* (5361), 295–298. DOI: 10.1126/science.280.5361.295.

67. Parsek, M. R.; Greenberg, E. P. Sociomicrobiology: the connections between quorum sensing and biofilms. *Trends Microbiol.* **2005,** *13* (1), 27–33. DOI: 10.1016/j.tim.2004.11.007.

68. Mah, T. F.; O'Toole, G. A. Mechanisms of biofilm resistance to antimicrobial agents. *Trends Microbiol.* **2001,** *9* (1), 34–39. DOI: 10.1016/s0966-842x(00)01913-2.

69. Lecoq, H. Découverte du premier virus, le virus de la mosaïque du tabac: 1892 ou 1898? *C R Acad Sci III* **2001,** *324* (10), 929–933. DOI: 10.1016/s0764-4469(01)01368-3.

70. *Essential Human Virology;* Elsevier, 2016.

71. Louten, J. Virus Structure and Classification. In: *Essential Human Virology*; Elsevier, 2016, pp 19–29. DOI: 10.1016/B978-0-12-800947-5.00002-8.

72. Sevvana, M.; Long, F.; Miller, A. J.; Klose, T.; Buda, G.; Sun, L.; Kuhn, R. J.; Rossmann, M. R. *Structure of Zika virus at a resolution of 3.1 Angstrom*, 2018. DOI: 10.2210/pdb6CO8/pdb.

73. Sirohi, D.; Kuhn, R. J. Zika Virus Structure, Maturation, and Receptors. *J. Infect. Dis.* **2017,** *216* (suppl_10), S935-S944. DOI: 10.1093/infdis/jix515.

74. Sevvana, M.; Long, F.; Miller, A. S.; Klose, T.; Buda, G.; Sun, L.; Kuhn, R. J.; Rossmann, M. G. Refinement and Analysis of the Mature Zika Virus Cryo-EM Structure at 3.1 Å Resolution. *Structure* **2018,** *26* (9), 1169-1177.e3. DOI: 10.1016/j.str.2018.05.006.

75. Musso, D.; Gubler, D. J. Zika Virus. *Clin. Microbiol. Rev.* **2016,** *29* (3), 487–524. DOI: 10.1128/cmr.00072-15.

76. Mlakar, J.; Korva, M.; Tul, N.; Popović, M.; Poljšak-Prijatelj, M.; Mraz, J.; Kolenc, M.; Resman Rus, K.; Vesnaver Vipotnik, T.; Fabjan Vodušek, V.; Vizjak, A.; Pižem, J.; Petrovec, M.; Avšič Županc, T. Zika Virus Associated with Microcephaly. *N. Engl. J. Med.* **2016,** *374* (10), 951–958. DOI: 10.1056/NEJMoa1600651.

77. Clokie, M. R.; Millard, A. D.; Letarov, A. V.; Heaphy, S. Phages in nature. *Bacteriophage* **2011,** *1* (1), 31–45. DOI: 10.4161/bact.1.1.14942.

78. Dion, M. B.; Oechslin, F.; Moineau, S. Phage diversity, genomics and phylogeny. *Nat. Rev. Microbiol.* **2020,** *18* (3), 125–138. DOI: 10.1038/s41579-019-0311-5.

79. Sanz-Gaitero, M.; Seoane-Blanco, M.; van Raaij, M. J. Structure and Function of Bacteriophages. In *Bacteriophages*; Harper, D. R., Abedon, S. T., Burrowes, B. H., McConville, M. L., Eds.; Springer International Publishing, **2021**, pp 19–91. DOI: 10.1007/978-3-319-41986-2_1.

80. E. White, H.; V. Orlova, E. Bacteriophages: Their Structural Organisation and Function. In *Bacteriophages - Perspectives and Future*; Savva, R., Ed.; IntechOpen, **2020**. DOI: 10.5772/intechopen.85484.

81. Love, J. C.; Estroff, L. A.; Kriebel, J. K.; Nuzzo, R. G.; Whitesides, G. M. Self-assembled monolayers of thiolates on metals as a form of nanotechnology. *Chem. Rev.* **2005,** *105* (4), 1103–1169. DOI: 10.1021/cr0300789.

82. Saigusa, Y. Quartz-Based Piezoelectric Materials. In: *Advanced Piezoelectric Materials*; Elsevier, 2017, pp 197–233. DOI: 10.1016/B978-0-08-102135-4.00005-9.

83. Dixon, M. C. Quartz Crystal Microbalance with Dissipation Monitoring: Enabling Real-Time Characterization of Biological Materials and Their Interactions. *JBT* **2008,** *19* (3), 151–158.

84. Sauerbrey, G. Verwendung von Schwingquarzen zur Wgung dnner Schichten und zur Mikrowgung. *Z. Physik* **1959,** *155* (2), 206–222. DOI: 10.1007/BF01337937.

85. Rodahl, M.; Höök, F.; Krozer, A.; Brzezinski, P.; Kasemo, B. Quartz crystal microbalance setup for frequency and Q -factor measurements in gaseous and liquid environments. *Rev. Sci. Instrum.* **1995,** *66* (7), 3924–3930. DOI: 10.1063/1.1145396.

86. Plikusiene, I.; Maciulis, V.; Ramanavicius, A.; Ramanaviciene, A. Spectroscopic Ellipsometry and Quartz Crystal Microbalance with Dissipation for the Assessment of Polymer Layers and for the Application in Biosensing. *Polymers* **2022,** *14* (5). DOI: 10.3390/polym14051056.

87. Strauss, J.; Liu, Y.; Camesano, T. A. Bacterial adhesion to protein-coated surfaces: An AFM and QCM-D study. *JOM* **2009,** *61* (9), 71–74. DOI: 10.1007/s11837-009-0138-z.

88. Engström, J.; Benselfelt, T.; Wågberg, L.; D'Agosto, F.; Lansalot, M.; Carlmark, A.; Malmström, E. Tailoring adhesion of anionic surfaces using cationic PISA-latexes - towards tough nanocellulose materials in the wet state. *Nanoscale* **2019,** *11* (10), 4287–4302. DOI: 10.1039/C8NR08057G.

89. Marcus, I. M.; Herzberg, M.; Walker, S. L.; Freger, V. Pseudomonas aeruginosa attachment on QCM-D sensors: the role of cell and surface hydrophobicities. *Langmuir* **2012,** *28* (15), 6396–6402. DOI: 10.1021/la300333c.

90. Easley, A. D.; Ma, T.; Eneh, C. I.; Yun, J.; Thakur, R. M.; Lutkenhaus, J. L. A practical guide to quartz crystal microbalance with dissipation monitoring of thin polymer films. *J. Polym. Sci.* **2022,** *60* (7), 1090–1107. DOI: 10.1002/pol.20210324.

91. Wittmer, C. R.; Phelps, J. A.; Saltzman, W. M.; van Tassel, P. R. Fibronectin terminated multilayer films: protein adsorption and cell attachment studies. *Biomaterials* **2007,** *28* (5), 851–860. DOI: 10.1016/j.biomaterials.2006.09.037.

92. Welle, A.; Chiumiento, A.; Barbucci, R. Competitive protein adsorption on micro patterned polymeric biomaterials, and viscoelastic properties of tailor made extracellular matrices. *Biomol. Eng.* **2007,** *24* (1), 87–91. DOI: 10.1016/j.bioeng.2006.05.027.

93. Scheideler, L.; Rupp, F.; Wendel, H. P.; Sathe, S.; Geis-Gerstorfer, J. Photocoupling of fibronectin to titanium surfaces influences keratinocyte adhesion, pellicle formation and thrombogenicity. *Dent. Mater.* **2007,** *23* (4), 469–478. DOI: 10.1016/j.dental.2006.03.005.

94. Hampitak, P.; Melendrez, D.; Iliut, M.; Fresquet, M.; Parsons, N.; Spencer, B.; Jowitt, T. A.; Vijayaraghavan, A. Protein interactions and conformations on graphene-based materials mapped using a quartz-crystal microbalance with dissipation monitoring (QCM-D). *Carbon* **2020,** *165*, 317–327. DOI: 10.1016/j.carbon.2020.04.093.

95. Huang, S.; Hou, Q.; Guo, D.; Yang, H.; Chen, T.; Liu, F.; Hu, G.; Zhang, M.; Zhang, J.; Wang, J. Adsorption mechanism of mussel-derived adhesive proteins onto various self-assembled monolayers. *RSC Adv.* **2017,** *7* (63), 39530–39538. DOI: 10.1039/C7RA07425E.

96. Leino, T.; Raulio, M.; Salkinoja-Salonen, M.; Stenius, P.; Laine, J. Adsorption of bacteria and polycations on model surfaces of cellulose, hemicellulose and wood extractives studied by QCM-D. *Colloids Surf. B* **2011,** *86* (1), 131–139. DOI: 10.1016/j.colsurfb.2011.03.031.

97. Voinova, M. V.; Jonson, M.; Kasemo, B. Missing mass effect in biosensor's QCM applications. *Biosens. Bioelectron.* **2002,** *17* (10), 835–841. DOI: 10.1016/S0956-5663(02)00050-7.

98. Keiji Kanazawa, K.; Gordon, J. G. The oscillation frequency of a quartz resonator in contact with liquid. *Anal. Chim. Acta* **1985,** *175*, 99–105. DOI: 10.1016/S0003-2670(00)82721-X.

99. Johannsmann, D. Viscoelastic, mechanical, and dielectric measurements on complex samples with the quartz crystal microbalance. *PCCP* **2008,** *10* (31), 4516–4534. DOI: 10.1039/B803960G.

100. Reviakine, I.; Johannsmann, D.; Richter, R. P. Hearing what you cannot see and visualizing what you hear: interpreting quartz crystal microbalance data from solvated interfaces. *Anal. Chem.* **2011,** *83* (23), 8838–8848. DOI: 10.1021/ac201778h.

101. Rodahl, M.; Höök, F.; Fredriksson, C.; Keller, C. A.; Krozer, A.; Brzezinski, P.; Voinova, M.; Kasemo, B. Simultaneous frequency and dissipation factor QCM measurements of biomolecular adsorption and cell adhesion. *Faraday Discuss* **1997** (107), 229–246. DOI: 10.1039/A703137H.

102. Bian, K.; Gerber, C.; Heinrich, A. J.; Müller, D. J.; Scheuring, S.; Jiang, Y. Scanning probe microscopy. *Nat. Rev. Methods Primers* **2021,** *1* (1). DOI: 10.1038/s43586-021-00033-2.

103. Binnig, G.; Quate, C. F.; Gerber, C. Atomic force microscope. *Phys. Rev. Lett.* **1986,** *56* (9), 930–933. DOI: 10.1103/physrevlett.56.930.

104. Binnig, G.; Rohrer, H. Scanning tunneling microscopy—from birth to adolescence. *Rev. Mod. Phys.* **1987,** *59* (3), 615–625. DOI: 10.1103/RevModPhys.59.615.

105. Rodríguez-Galván, A.; Contreras-Torres, F. F. Scanning Tunneling Microscopy of Biological Structures: An Elusive Goal for Many Years. *Nanomaterials* **2022,** *12* (17). DOI: 10.3390/nano12173013.

106. *Non-Destructive Material Characterization Methods;* Elsevier, 2024.

107. Vahabi, S.; Nazemi Salman, B.; Javanmard, A. Atomic Force Microscopy Application in Biological Research: A Review Study. *Iran. J. Med. Sci.* **2013,** *38* (2), 76–83.

108. Costa, L.; Li-Destri, G.; Pontoni, D.; Konovalov, O.; Thomson, N. H. Liquid–Liquid Interfacial Imaging Using Atomic Force Microscopy. *Adv. Mater. Interfaces* **2017,** *4* (16). DOI: 10.1002/admi.201700203.

109. Peng, J.; Guo, J.; Ma, R.; Jiang, Y. Water-solid interfaces probed by high-resolution atomic force microscopy. *Surf. Sci. Rep.* **2022,** *77* (1), 100549. DOI: 10.1016/j.surfrep.2021.100549.

110. Meyer, G.; Amer, N. M. Simultaneous measurement of lateral and normal forces with an optical-beam-deflection atomic force microscope. *Appl. Phys. Lett.* **1990,** *57* (20), 2089–2091. DOI: 10.1063/1.103950.

111. Kazantsev, D. V.; Kazantzeva, E. A. A four-segment photodiode cantilever-bending sensor for an atomic-force microscope. *Instrum Exp Tech* **2014,** *57* (5), 631–639. DOI: 10.1134/S0020441214040046.

112. Dzedzickis, A.; Rožėnė, J.; Bučinskas, V.; Viržonis, D.; Morkvėnaitė-Vilkončienė, I. Characteristics and Functionality of Cantilevers and Scanners in Atomic Force Microscopy. *Materials* **2023,** *16* (19). DOI: 10.3390/ma16196379.

113. Butt, H.-J.; Cappella, B.; Kappl, M. Force measurements with the atomic force microscope: Technique, interpretation and applications. *Surf. Sci. Rep.* **2005,** *59* (1-6), 1–152. DOI: 10.1016/j.surfrep.2005.08.003.

114. Giessibl, F. J. Advances in atomic force microscopy. *Rev. Mod. Phys.* **2003,** *75* (3), 949–983. DOI: 10.1103/RevModPhys.75.949.

115. Sanders, W. C. *Atomic Force Microscopy;* CRC Press, 2019. DOI: 10.1201/9780429266553.

116. Yuan, S.; Liu, L.; Wang, Z.; Xi, N. *AFM-Based Observation and Robotic Nano-manipulation;* Springer Singapore, 2020. DOI: 10.1007/978-981-15-0508-9.

117. Deng, X.; Xiong, F.; Li, X.; Xiang, B.; Li, Z.; Wu, X.; Guo, C.; Li, X.; Li, Y.; Li, G.; Xiong, W.; Zeng, Z. Application of atomic force microscopy in cancer research. *J. Nanobiotechnology* **2018,** *16* (1), 102. DOI: 10.1186/s12951-018-0428-0.

118. Zhong, Q.; Inniss, D.; Kjoller, K.; Elings, V. B. Fractured polymer/silica fiber surface studied by tapping mode atomic force microscopy. *Surf. Sci.* **1993,** *290* (1-2), L688-L692. DOI: 10.1016/0039-6028(93)90582-5.

119. García, R. Dynamic atomic force microscopy methods. *Surf. Sci. Rep.* **2002,** *47* (6-8), 197–301. DOI: 10.1016/S0167-5729(02)00077-8.

120. Liu, H.; Li, Y.; Zhang, Y.; Chen, Y.; Song, Z.; Wang, Z.; Zhang, S.; Qian, J. Intelligent tuning method of PID parameters based on iterative learning control for atomic force microscopy. *Micron* **2018,** *104*, 26–36. DOI: 10.1016/j.micron.2017.09.009.

121. Ando, T. High-speed atomic force microscopy. *Microscopy* **2013,** *62* (1), 81–93. DOI: 10.1093/jmicro/dfs093.

122. Fukuda, S.; Ando, T. Faster high-speed atomic force microscopy for imaging of biomolecular processes. *Rev. Sci. Instrum.* **2021,** *92* (3), 33705. DOI: 10.1063/5.0032948.

123. Ando, T.; Kodera, N.; Takai, E.; Maruyama, D.; Saito, K.; Toda, A. A high-speed atomic force microscope for studying biological macromolecules. *Proc. Natl. Acad. Sci. U.S.A.* **2001,** *98* (22), 12468–12472. DOI: 10.1073/pnas.211400898.

124. Roberts, G. C. K., Ed. *Encyclopedia of Biophysics;* Springer Berlin Heidelberg, 2013. DOI: 10.1007/978-3-642-16712-6.

125. Ando, T. *High-Speed Atomic Force Microscopy in Biology;* Springer Berlin Heidelberg, 2022. DOI: 10.1007/978-3-662-64785-1.

126. Casuso, I.; Kodera, N.; Le Grimellec, C.; Ando, T.; Scheuring, S. Contact-mode high-resolution high-speed atomic force microscopy movies of the purple membrane. *Biophys. J.* **2009,** *97* (5), 1354–1361. DOI: 10.1016/j.bpj.2009.06.019.

127. Elemans, J. A. A. W.; Lei, S.; Feyter, S. de. Molecular and supramolecular networks on surfaces: from two-dimensional crystal engineering to reactivity. *Angew. Chem. Int. Ed. Engl.* **2009,** *48* (40), 7298–7332. DOI: 10.1002/anie.200806339.

128. Kudernac, T.; Lei, S.; Elemans, J. A. A. W.; Feyter, S. de. Two-dimensional supramolecular self-assembly: nanoporous networks on surfaces. *Chem. Soc. Rev.* **2009,** *38* (2), 402–421. DOI: 10.1039/B708902N.

129. Peng, X.; Zhao, F.; Peng, Y.; Li, J.; Zeng, Q. Dynamic surface-assisted assembly behaviours mediated by external stimuli. *Soft Matter* **2020,** *16* (1), 54–63. DOI: 10.1039/C9SM01847F.

130. Verstraete, L.; Feyter, S. de. 2D Self-assembled molecular networks and on-surface reactivity under nanoscale lateral confinement. *Chem. Soc. Rev.* **2021,** *50* (10), 5884–5897. DOI: 10.1039/D0CS01338B.

131. Vigier-Carrière, C.; Boulmedais, F.; Schaaf, P.; Jierry, L. Surface-Assisted Self-Assembly Strategies Leading to Supramolecular Hydrogels. *Angew. Chem. Int. Ed. Engl.* **2018,** *57* (6), 1448–1456. DOI: 10.1002/anie.201708629.

132. Yang, B.; Adams, D. J.; Marlow, M.; Zelzer, M. Surface-Mediated Supramolecular Self-Assembly of Protein, Peptide, and Nucleoside Derivatives: From Surface Design to the Underlying Mechanism and Tailored Functions. *Langmuir* **2018,** *34* (50), 15109–15125. DOI: 10.1021/acs.langmuir.8b01165.

133. Kundu, B.; Eltohamy, M.; Yadavalli, V. K.; Kundu, S. C.; Kim, H.-W. Biomimetic Designing of Functional Silk Nanotopography Using Self-assembly. *ACS Appl. Mater. Interfaces* **2016,** *8* (42), 28458–28467. DOI: 10.1021/acsami.6b07872.

134. Xu, T.; Liang, C.; Ji, S.; Ding, D.; Kong, D.; Wang, L.; Yang, Z. Surface-Induced Hydrogelation for Fluorescence and Naked-Eye Detections of Enzyme Activity in Blood. *Anal. Chem.* **2016,** *88* (14), 7318–7323. DOI: 10.1021/acs.analchem.6b01660.

135. Li, J.; Liu, C.; Han, X.; Tian, M.; Jiang, B.; Li, W.; Ou, C.; Dou, N.; Han, Z.; Ji, T.; Cao, X.; Zhong, X.; Zhang, L. Supramolecular Electronics: Monolayer Assembly of Nonamphiphilic Molecules via

Water Surface-Assisted Molecular Deposition. *ACS Appl. Mater. Interfaces* **2024,** *16* (36), 48438–48447. DOI: 10.1021/acsami.4c05552.

136. Hu, T.; Minoia, A.; Velpula, G.; Ryskulova, K.; van Hecke, K.; Lazzaroni, R.; Mali, K. S.; Hoogenboom, R.; Feyter, S. de. From One-Dimensional Disordered Racemate to Ordered Racemic Conglomerates through Metal-Coordination-Driven Self-Assembly at the Liquid-Solid Interface. *Chem. Eur. J.* **2024,** *30* (2), e202302545. DOI: 10.1002/chem.202302545.

137. Abb, S.; Harnau, L.; Gutzler, R.; Rauschenbach, S.; Kern, K. Two-dimensional honeycomb network through sequence-controlled self-assembly of oligopeptides. *Nat. Commun.* **2016,** *7*, 10335. DOI: 10.1038/ncomms10335.

138. Pyles, H.; Zhang, S.; Yoreo, J. J. de; Baker, D. Controlling protein assembly on inorganic crystals through designed protein interfaces. *Nature* **2019,** *571* (7764), 251–256. DOI: 10.1038/s41586-019-1361-6.

139. Sun, X.; Hyeon Ko, S.; Zhang, C.; Ribbe, A. E.; Mao, C. Surface-mediated DNA self-assembly. *J. Am. Chem. Soc.* **2009,** *131* (37), 13248–13249. DOI: 10.1021/ja906475w.

140. Li, X.; Wang, J.; Baptist, A. V.; Wu, W.; Heuer-Jungemann, A.; Zhang, T. Crystalline Assemblies of DNA Nanostructures and their Functional Properties. *Angew. Chem. Int. Ed. Engl.* **2024**, e202416948. DOI: 10.1002/anie.202416948.

141. Parikka, J. M.; Sokołowska, K.; Markešević, N.; Toppari, J. J. Constructing Large 2D Lattices Out of DNA-Tiles. *Molecules* **2021,** *26* (6), 1502. DOI: 10.3390/molecules26061502.

142. Tekin, C.; Caroprese, V.; Bastings, M. M. C. Dynamic Surface Interactions Enable the Self-Assembly of Perfect Supramolecular Crystals. *ACS Appl. Mater. Interfaces* **2024. DOI:** 10.1021/acsami.4c11813.

143. Aghebat Rafat, A.; Pirzer, T.; Scheible, M. B.; Kostina, A.; Simmel, F. C. Surface-Assisted Large-Scale Ordering of DNA Origami Tiles. *Angew. Chem. Int. Ed. Engl.* **2014,** *53* (29), 7665–7668. DOI: 10.1002/anie.201403965.

144. Liu, L.; Mao, D.; Li, Z.; Zheng, M.; He, K.; Mao, C. Surface-assisted self-assembly of 2D, DNA binary crystals. *Nanoscale* **2023,** *15* (23), 9941–9945. DOI: 10.1039/D3NR01187A.

145. Hamada, S.; Murata, S. Substrate-assisted assembly of interconnected single-duplex DNA nanostructures. *Angew. Chem. Int. Ed. Engl.* **2009,** *48* (37), 6820–6823. DOI: 10.1002/anie.200902662.

146. Xin, Y.; Shen, B.; Kostiainen, M. A.; Grundmeier, G.; Castro, M.; Linko, V.; Keller, A. Scaling Up DNA Origami Lattice Assembly. *Chem. Eur. J.* **2021,** *27* (33), 8564–8571. DOI: 10.1002/chem.202100784.

147. Xin, Y.; Ji, X.; Grundmeier, G.; Keller, A. Dynamics of lattice defects in mixed DNA origami monolayers. *Nanoscale* **2020,** *12* (17), 9733–9743. DOI: 10.1039/d0nr01252a.

148. Liu, L.; Li, Y.; Wang, Y.; Zheng, J.; Mao, C. Regulating DNA Self-assembly by DNA-Surface Interactions. *ChemBioChem* **2017,** *18* (24), 2404–2407. DOI: 10.1002/cbic.201700545 (accessed 2018-07-01).

149. Nievergelt, A. P.; Kammer, C.; Brillard, C.; Kurisinkal, E.; Bastings, M. M. C.; Karimi, A.; Fantner, G. E. Large-Range HS-AFM Imaging of DNA Self-Assembly through In Situ Data-Driven Control. *Small Meth.* **2019,** *3* (7), 1900031. DOI: 10.1002/smtd.201900031.

150. Julin, S.; Linko, V.; Kostiainen, M. A. Reconfigurable pH-Responsive DNA Origami Lattices. *ACS Nano* **2023,** *17* (11), 11014–11022. DOI: 10.1021/acsnano.3c03438.

151. Kempter, S.; Khmelinskaia, A.; Strauss, M. T.; Schwille, P.; Jungmann, R.; Liedl, T.; Bae, W. Single Particle Tracking and Super-Resolution Imaging of Membrane-Assisted Stop-and-Go Diffusion and Lattice Assembly of DNA Origami. *ACS Nano* **2019,** *13* (2), 996–1002. DOI: 10.1021/acsnano.8b04631.

152. Suzuki, Y.; Sugiyama, H.; Endo, M. Complexing DNA Origami Frameworks through Sequential Self-Assembly Based on Directed Docking. *Angew. Chem. Int. Ed. Engl.* **2018,** *57* (24), 7061–7065. DOI: 10.1002/anie.201801983.

153. Sato, Y.; Endo, M.; Morita, M.; Takinoue, M.; Sugiyama, H.; Murata, S.; Nomura, S. M.; Suzuki, Y. Environment-Dependent Self-Assembly of DNA Origami Lattices on Phase-Separated Lipid Membranes. *Adv. Mater. Interfaces* **2018,** *17*, 1800437. DOI: 10.1002/admi.201800437.

154. Avakyan, N.; Conway, J. W.; Sleiman, H. F. Long-Range Ordering of Blunt-Ended DNA Tiles on Supported Lipid Bilayers. *J. Am. Chem. Soc.* **2017,** *139* (34), 12027–12034. DOI: 10.1021/jacs.7b06572.

155. Gavrilović, S.; Brüggenthies, G. A.; Weck, J. M.; Heuer-Jungemann, A.; Schwille, P. Protein-Assisted Large-Scale Assembly and Differential Patterning of DNA Origami Lattices. *Small* **2024,** *20* (24), e2309680. DOI: 10.1002/smll.202309680.

156. Pothineni, B. K.; Grundmeier, G.; Keller, A. Cation-dependent assembly of hexagonal DNA origami lattices on SiO2 surfaces. *Nanoscale* **2023,** *15* (31), 12894–12906. DOI: 10.1039/D3NR02926C.

157. Mao, D.; Liu, L.; Zhang, C.; Liu, H.; Mao, C. Molecular Lithography on Silicon Wafers Guided by Porous, Extended Arrays of Small DNA Tiles. *Langmuir* **2023,** *39* (33), 11782–11787. DOI: 10.1021/acs.langmuir.3c01422.

158. Yan, H.; Park, S. H.; Finkelstein, G.; Reif, J. H.; LaBean, T. H. DNA-templated self-assembly of protein arrays and highly conductive nanowires. *Science* **2003,** *301* (5641), 1882–1884. DOI: 10.1126/science.1089389.

159. Liu, W.; Zhong, H.; Wang, R.; Seeman, N. C. Crystalline two-dimensional DNA-origami arrays. *Angew. Chem. Int. Ed. Engl.* **2011,** *50* (1), 264–267. DOI: 10.1002/anie.201005911.

160. Liu, L.; Zheng, M.; Li, Z.; Li, Q.; Mao, C. Patterning Nanoparticles with DNA Molds. *ACS Appl. Mater. Interfaces* **2019,** *11* (15), 13853–13858. DOI: 10.1021/acsami.8b22691.

161. Yang, S.; Liu, W.; Zhang, Y.; Wang, R. Bottom-Up Fabrication of Large-Scale Gold Nanorod Arrays by Surface Diffusion-Mediated DNA Origami Assembly. *ACS Appl. Mater. Interfaces* **2021,** *13* (42), 50516–50523. DOI: 10.1021/acsami.1c13173.

162. Kielar, C.; Zhu, S.; Grundmeier, G.; Keller, A. Quantitative Assessment of Tip Effects in Single-Molecule High-Speed Atomic Force Microscopy Using DNA Origami Substrates. *Angew. Chem. Int. Ed. Engl.* **2020,** *59* (34), 14336–14341. DOI: 10.1002/anie.202005884.

163. Nievergelt, A. P.; Banterle, N.; Andany, S. H.; Gönczy, P.; Fantner, G. E. High-speed photothermal off-resonance atomic force microscopy reveals assembly routes of centriolar scaffold protein SAS-6. *Nat. Nanotechnol.* **2018,** *13* (8), 696–701. DOI: 10.1038/s41565-018-0149-4.

164. Nečas, D.; Klapetek, P. Gwyddion: An open-source software for SPM data analysis. *Open Phys.* **2012,** *10* (1), 99. DOI: 10.2478/s11534-011-0096-2.

165. Revellame, E. D.; Fortela, D.; Sharp, W.; Hernandez, R.; Zappi, M. E. Adsorption kinetic modeling using pseudo-first order and pseudo-second order rate laws: A review. *Clean. Engin. Technol.* **2020,** *1*, 100032. DOI: 10.1016/j.clet.2020.100032.

166. Nummelin, S.; Kommeri, J.; Kostiainen, M. A.; Linko, V. Evolution of Structural DNA Nanotechnology. *Adv. Mater.* **2018,** *30* (24), 1703721. DOI: 10.1002/adma.201703721.

167. Tapio, K.; Bald, I. The potential of DNA origami to build multifunctional materials. *Multifunct. Mater.* **2020,** *3* (3), 32001. DOI: 10.1088/2399-7532/ab80d5.

168. Endo, M.; Yang, Y.; Sugiyama, H. DNA origami technology for biomaterials applications. *Biomater. Sci.* **2013,** *1* (4), 347–360. DOI: 10.1039/c2bm00154c.

169. Dunn, K. E.; Dannenberg, F.; Ouldridge, T. E.; Kwiatkowska, M.; Turberfield, A. J.; Bath, J. Guiding the folding pathway of DNA origami. *Nature* **2015,** *525* (7567), 82–86. DOI: 10.1038/nature14860.

170. Ji, J.; Karna, D.; Mao, H. DNA origami nano-mechanics. *Chem. Soc. Rev.* **2021,** *50* (21), 11966–11978. DOI: 10.1039/d1cs00250c.

171. Ramakrishnan, S.; Ijäs, H.; Linko, V.; Keller, A. Structural stability of DNA origami nanostructures under application-specific conditions. *Comput. Struct. Biotechnol. J.* **2018,** *16*, 342–349. DOI: 10.1016/j.csbj.2018.09.002.

172. Linko, V.; Keller, A. Stability of DNA Origami Nanostructures in Physiological Media: The Role of Molecular Interactions. *Small* **2023**, 2301935. DOI: 10.1002/smll.202301935.

173. Keller, A.; Linko, V. Challenges and Perspectives of DNA Nanostructures in Biomedicine. *Angew. Chem. Int. Ed. Engl.* **2020,** *59* (37), 15818–15833. DOI: 10.1002/anie.201916390.

174. Dass, M.; Gür, F. N.; Kołątaj, K.; Urban, M. J.; Liedl, T. DNA Origami-Enabled Plasmonic Sensing. *J. Phys. Chem. C* **2021,** *125* (11), 5969–5981. DOI: 10.1021/acs.jpcc.0c11238.

175. Pang, C.; Aryal, B. R.; Ranasinghe, D. R.; Westover, T. R.; Ehlert, A. E. F.; Harb, J. N.; Davis, R. C.; Woolley, A. T. Bottom-Up Fabrication of DNA-Templated Electronic Nanomaterials and Their Characterization. *Nanomaterials* **2021,** *11* (7), 1655. DOI: 10.3390/nano11071655.

176. Jiang, W.; Li, J.; Lin, Z.; Guo, J.; Ma, J.; Wang, Z.; Zhang, M.; Wu, Y. Recent Advances of DNA Origami Technology and Its Application in Nanomaterial Preparation. *Small Struct.* **2023**, 2200376. DOI: 10.1002/sstr.202200376.

177. Heuer-Jungemann, A.; Linko, V. Engineering Inorganic Materials with DNA Nanostructures. *ACS Cent. Sci.* **2021,** *7* (12), 1969–1979. DOI: 10.1021/acscentsci.1c01272.

178. Shen, B.; Linko, V.; Tapio, K.; Pikker, S.; Lemma, T.; Gopinath, A.; Gothelf, K. V.; Kostiainen, M. A.; Toppari, J. J. Plasmonic nanostructures through DNA-assisted lithography. *Sci. Adv.* **2018,** *4* (2), eaap8978. DOI: 10.1126/sciadv.aap8978.

179. Piskunen, P.; Shen, B.; Keller, A.; Toppari, J. J.; Kostiainen, M. A.; Linko, V. Biotemplated Lithography of Inorganic Nanostructures (BLIN) for Versatile Patterning of Functional Materials. *ACS Appl. Nano Mater.* **2021,** *4* (1), 529–538. DOI: 10.1021/acsanm.0c02849.

180. Hanke, M.; Grundmeier, G.; Keller, A. Direct visualization of the drug loading of single DNA origami nanostructures by AFM-IR nanospectroscopy. *Nanoscale* **2022,** *14* (32), 11552–11560. DOI: 10.1039/d2nr02701a.

181. Kershner, R. J.; Bozano, L. D.; Micheel, C. M.; Hung, A. M.; Fornof, A. R.; Cha, J. N.; Rettner, C. T.; Bersani, M.; Frommer, J.; Rothemund, P. W. K.; Wallraff, G. M. Placement and orientation of individual DNA shapes on lithographically patterned surfaces. *Nat. Nanotechnol.* **2009,** *4* (9), 557–561. DOI: 10.1038/nnano.2009.220.

182. Kabiri, Y.; Ananth, A. N.; van der Torre, J.; Katan, A.; Hong, J.-Y.; Malladi, S.; Kong, J.; Zandbergen, H.; Dekker, C. Distortion of DNA Origami on Graphene Imaged with Advanced TEM Techniques. *Small* **2017,** *13* (31). DOI: 10.1002/smll.201700876.

183. Surwade, S. P.; Zhao, S.; Liu, H. Molecular lithography through DNA-mediated etching and masking of SiO2. *J. Am. Chem. Soc.* **2011,** *133* (31), 11868–11871. DOI: 10.1021/ja2038886.

184. Surwade, S. P.; Zhou, F.; Wei, B.; Sun, W.; Powell, A.; O'Donnell, C.; Yin, P.; Liu, H. Nanoscale growth and patterning of inorganic oxides using DNA nanostructure templates. *J. Am. Chem. Soc.* **2013,** *135* (18), 6778–6781. DOI: 10.1021/ja401785h.

185. Gopinath, A.; Rothemund, P. W. K. Optimized assembly and covalent coupling of single-molecule DNA origami nanoarrays. *ACS Nano* **2014,** *8* (12), 12030–12040. DOI: 10.1021/nn506014s.

186. Gopinath, A.; Miyazono, E.; Faraon, A.; Rothemund, P. W. K. Engineering and mapping nanocavity emission via precision placement of DNA origami. *Nature* **2016,** *535* (7612), 401–405. DOI: 10.1038/nature18287.

187. Brassat, K.; Ramakrishnan, S.; Bürger, J.; Hanke, M.; Doostdar, M.; Lindner, J. K. N.; Grundmeier, G.; Keller, A. On the Adsorption of DNA Origami Nanostructures in Nanohole Arrays. *Langmuir* **2018,** *34* (49), 14757–14765. DOI: 10.1021/acs.langmuir.8b00793.

188. Shetty, R. M.; Brady, S. R.; Rothemund, P. W. K.; Hariadi, R. F.; Gopinath, A. Bench-Top Fabrication of Single-Molecule Nanoarrays by DNA Origami Placement. *ACS Nano* **2021,** *15* (7), 11441–11450. DOI: 10.1021/acsnano.1c01150.

189. Teshome, B.; Facsko, S.; Keller, A. Topography-controlled alignment of DNA origami nanotubes on nanopatterned surfaces. *Nanoscale* **2014,** *6* (3), 1790–1796. DOI: 10.1039/c3nr04627c.

190. Aghebat Rafat, A.; Pirzer, T.; Scheible, M. B.; Kostina, A.; Simmel, F. C. Surface-assisted large-scale ordering of DNA origami tiles. *Angew. Chem. Int. Ed. Engl.* **2014,** *53* (29), 7665–7668. DOI: 10.1002/anie.201403965.

191. Xin, Y.; Ji, X.; Grundmeier, G.; Keller, A. Dynamics of lattice defects in mixed DNA origami monolayers. *Nanoscale* **2020,** *12* (17), 9733–9743. DOI: 10.1039/d0nr01252a.

192. Xin, Y.; Shen, B.; Kostiainen, M. A.; Grundmeier, G.; Castro, M.; Linko, V.; Keller, A. Scaling Up DNA Origami Lattice Assembly. *Chem. Eur. J.* **2021,** *27* (33), 8564–8571. DOI: 10.1002/chem.202100784.

193. Sides, P. J.; Faruqui, D.; Gellman, A. J. Dynamics of charging of muscovite mica: measurement and modeling. *Langmuir* **2009,** *25* (3), 1475–1481. DOI: 10.1021/la802752g.

194. Bousse, L.; Mostarshed, S.; van der Shoot, B.; Rooij, N. de; Gimmel, P.; Göpel, W. Zeta potential measurements of Ta2O5 and SiO2 thin films. *J. Colloid Interface Sci.* **1991,** *147* (1), 22–32. DOI: 10.1016/0021-9797(91)90130-Z.

195. Keller, A.; Fritzsche, M.; Ogaki, R.; Bald, I.; Facsko, S.; Dong, M.; Kingshott, P.; Besenbacher, F. Tuning the hydrophobicity of mica surfaces by hyperthermal Ar ion irradiation. *J. Chem. Phys.* **2011,** *134* (10), 104705. DOI: 10.1063/1.3561292].

196. Yang, Y.; Yu, M.; Böke, F.; Qin, Q.; Hübner, R.; Knust, S.; Schwiderek, S.; Grundmeier, G.; Fischer, H.; Keller, A. Effect of nanoscale surface topography on the adsorption of globular proteins. *Appl. Surf. Sci.* **2021,** *535*, 147671. DOI: 10.1016/j.apsusc.2020.147671.

197. Tapio, K.; Kielar, C.; Parikka, J. M.; Keller, A.; Järvinen, H.; Fahmy, K.; Toppari, J. J. Large-Scale Formation of DNA Origami Lattices on Silicon. *Chem. Mater.* **2023,** *35* (5), 1961–1971. DOI: 10.1021/acs.chemmater.2c03190#.

198. Yoo, J.; Aksimentiev, A. Competitive binding of cations to duplex DNA revealed through molecular dynamics simulations. *J. Phys. Chem. B* **2012,** *116* (43), 12946–12954. DOI: 10.1021/jp306598y.

199. Li, W.; Nordenskiöld, L.; Mu, Y. Sequence-specific Mg2+-DNA interactions: a molecular dynamics simulation study. *J. Phys. Chem. B* **2011,** *115* (49), 14713–14720. DOI: 10.1021/jp2052568.

200. Kolev, S. K.; Petkov, P. S.; Rangelov, M. A.; Trifonov, D. V.; Milenov, T. I.; Vayssilov, G. N. Interaction of Na+, K+, Mg2+ and Ca2+ counter cations with RNA. *Metallomics* **2018,** *10* (5), 659–678. DOI: 10.1039/c8mt00043c.

201. Cruz-León, S.; Schwierz, N. Hofmeister Series for Metal-Cation-RNA Interactions: The Interplay of Binding Affinity and Exchange Kinetics. *Langmuir* **2020,** *36* (21), 5979–5989. DOI: 10.1021/acs.langmuir.0c00851.

202. Petrov, A. S.; Bowman, J. C.; Harvey, S. C.; Williams, L. D. Bidentate RNA-magnesium clamps: on the origin of the special role of magnesium in RNA folding. *RNA* **2011,** *17* (2), 291–297. DOI: 10.1261/rna.2390311.

203. Zhao, Y.; Wang, G.; Lu, T. *Characterization of Amorphous and Crystalline Rough Surface*: *Principles and Applications*; Experimental methods in the physical sciences; Vol. 37; Academic Press, 2001.

204. Shen, B.; Linko, V.; Tapio, K.; Kostiainen, M. A.; Toppari, J. J. Custom-shaped metal nanostructures based on DNA origami silhouettes. *Nanoscale* **2015,** *7* (26), 11267–11272. DOI: 10.1039/C5NR02300A.

205. Kollmann, F.; Ramakrishnan, S.; Shen, B.; Grundmeier, G.; Kostiainen, M. A.; Linko, V.; Keller, A. Superstructure-Dependent Loading of DNA Origami Nanostructures with a Groove-Binding Drug. *ACS Omega* **2018,** *3* (8), 9441–9448. DOI: 10.1021/acsomega.8b00934.

206. Takabayashi, S.; Kotani, S.; Flores-Estrada, J.; Spears, E.; Padilla, J. E.; Godwin, L. C.; Graugnard, E.; Kuang, W.; Sills, S.; Hughes, W. L. Boron-Implanted Silicon Substrates for Physical Adsorption of DNA Origami. *Int. J. Mol. Sci.* **2018,** *19* (9), 2513. DOI: 10.3390/ijms19092513.

207. Keller, A.; Facsko, S.; Möller, W. The morphology of amorphous SiO(2) surfaces during low energy ion sputtering. *J. Phys. Condens. Matter* **2009,** *21* (49), 495305. DOI: 10.1088/0953-8984/21/49/495305.

208. Rupich, S. M.; Chabal, Y. J. Surface Chemical Composition and Morphology. In: *Handbook of Silicon Wafer Cleaning Technology*; Elsevier, 2018, pp 505–577. DOI: 10.1016/B978-0-323-51084-4.00009-5.

209. Ovchinnikov, A.; Mudring, A.-V. Flux Growth, Crystal Structures, and Electronic Properties of the Ternary Intermetallic Compounds Ca3Pd4Bi8 and Ca3Pt4Bi8. *Inorg. Chem.* **2022,** *61* (25), 9756–9766. DOI: 10.1021/acs.inorgchem.2c01248.

210. Singh, B.; Bdikin, I.; Kaushal, A.; Kumar, B. Flux growth and effect of cobalt doping on dielectric, conductivity and relaxation behaviour of 0.91Pb[Zn 1/3 Nb 2/3]O 3 –0.09PbTiO 3 crystals. *CrystEngComm* **2014,** *16* (38), 9135–9142. DOI: 10.1039/C4CE01105H.

211. Nečas, D.; Klapetek, P. Gwyddion: an open-source software for SPM data analysis. *Open Phys.* **2012,** *10* (1), 181–188. DOI: 10.2478/s11534-011-0096-2.

212. Parikka, J. M.; Sokołowska, K.; Markešević, N.; Toppari, J. J. Constructing Large 2D Lattices Out of DNA-Tiles. *Molecules* **2021,** *26* (6). DOI: 10.3390/molecules26061502.

213. Gavrilović, S.; Brüggenthies, G. A.; Weck, J. M.; Heuer-Jungemann, A.; Schwille, P. Protein-Assisted Large-Scale Assembly and Differential Patterning of DNA Origami Lattices. *Small* **2024,** *20* (24), e2309680. DOI: 10.1002/smll.202309680.

214. Franquelim, H. G.; Khmelinskaia, A.; Sobczak, J.-P.; Dietz, H.; Schwille, P. Membrane sculpting by curved DNA origami scaffolds. *Nat. Commun.* **2018,** *9* (1), 811. DOI: 10.1038/s41467-018-03198-9.

215. Yang, J.; Jahnke, K.; Xin, L.; Jing, X.; Zhan, P.; Peil, A.; Griffo, A.; Škugor, M.; Yang, D.; Fan, S.; Göpfrich, K.; Yan, H.; Wang, P.; Liu, N. Modulating Lipid Membrane Morphology by Dynamic DNA Origami Networks. *Nano Lett.* **2023,** *23* (14), 6330–6336. DOI: 10.1021/acs.nanolett.3c00750.

216. Journot, C. M. A.; Ramakrishna, V.; Wallace, M. I.; Turberfield, A. J. Modifying Membrane Morphology and Interactions with DNA Origami Clathrin-Mimic Networks. *ACS Nano* **2019,** *13* (9), 9973–9979. DOI: 10.1021/acsnano.8b07734.

217. Julin, S.; Linko, V.; Kostiainen, M. A. Reconfigurable pH-Responsive DNA Origami Lattices. *ACS Nano* **2023,** *17* (11), 11014–11022. DOI: 10.1021/acsnano.3c03438.

218. Liu, L.; Zheng, M.; Li, Z.; Li, Q.; Mao, C. Patterning Nanoparticles with DNA Molds. *ACS Appl. Mater. Interfaces* **2019,** *11* (15), 13853–13858. DOI: 10.1021/acsami.8b22691.

219. Kulikowski, J.; Wang, S.; Aitken, Z.; Grimm, J.; Gao, B.; Wang, M. M.; Doan, D.; Lee, A. C.; Shen, L.; Huang, W.; Devaraj, A.; Zhang, Y.-W.; Ke, Y.; Gu, X. W. DNA-silica nanolattices as mechanical metamaterials. *Matter* **2024,** *7* (6), 2144–2160. DOI: 10.1016/j.matt.2024.03.020.

220. Yang, S.; Liu, W.; Zhang, Y.; Wang, R. Bottom-Up Fabrication of Large-Scale Gold Nanorod Arrays by Surface Diffusion-Mediated DNA Origami Assembly. *ACS Appl. Mater. Interfaces* **2021,** *13* (42), 50516–50523. DOI: 10.1021/acsami.1c13173.

221. Liu, H.; Matthies, M.; Russo, J.; Rovigatti, L.; Narayanan, R. P.; Diep, T.; McKeen, D.; Gang, O.; Stephanopoulos, N.; Sciortino, F.; Yan, H.; Romano, F.; Šulc, P. Inverse design of a pyrochlore lattice of DNA origami through model-driven experiments. *Science* **2024,** *384* (6697), 776–781. DOI: 10.1126/science.adl5549.

222. Posnjak, G.; Yin, X.; Butler, P.; Bienek, O.; Dass, M.; Lee, S.; Sharp, I. D.; Liedl, T. Diamond-lattice photonic crystals assembled from DNA origami. *Science* **2024,** *384* (6697), 781–785. DOI: 10.1126/science.adl2733.

223. Michelson, A.; Subramanian, A.; Kisslinger, K.; Tiwale, N.; Xiang, S.; Shen, E.; Kahn, J. S.; Nykypanchuk, D.; Yan, H.; Nam, C.-Y.; Gang, O. Three-dimensional nanoscale metal, metal oxide, and semiconductor frameworks through DNA-programmable assembly and templating. *Sci. Adv.* **2024,** *10* (2), eadl0604. DOI: 10.1126/sciadv.adl0604.

224. Shen, B.; Linko, V.; Tapio, K.; Kostiainen, M. A.; Toppari, J. J. Custom-Shaped Metal Nanostructures Based on DNA Origami Silhouettes. *Nanoscale* **2015,** *7* (26), 11267–11272. DOI: 10.1039/c5nr02300a.

225. Shen, B.; Linko, V.; Tapio, K.; Pikker, S.; Lemma, T.; Gopinath, A.; Gothelf, K. V.; Kostiainen, M. A.; Toppari, J. J. Plasmonic nanostructures through DNA-assisted lithography. *Sci. Adv.* **2018,** *4* (2), eaap8978. DOI: 10.1126/sciadv.aap8978 (accessed 2018-07-01).

226. Piskunen, P.; Shen, B.; Keller, A.; Toppari, J. J.; Kostiainen, M. A.; Linko, V. Biotemplated Lithography of Inorganic Nanostructures (BLIN) for Versatile Patterning of Functional Materials. *ACS Appl. Nano Mater.* **2021,** *4* (1), 529–538. DOI: 10.1021/acsanm.0c02849.

227. Kabusure, K. M.; Piskunen, P.; Yang, J.; Kataja, M.; Chacha, M.; Ojasalo, S.; Shen, B.; Hakala, T. K.; Linko, V. Optical characterization of DNA origami-shaped silver nanoparticles created through biotemplated lithography. *Nanoscale* **2022,** *14* (27), 9648–9654. DOI: 10.1039/D1NR06256E.

228. Kabusure, K. M.; Piskunen, P.; Yang, J.; Linko, V.; Hakala, T. K. Raman enhancement in bowtie-shaped aperture-particle hybrid nanostructures fabricated with DNA-assisted lithography. *Nanoscale* **2023,** *15* (19), 8589–8596. DOI: 10.1039/D3NR00616F.

229. Xin, Y.; Shen, B.; Kostiainen, M. A.; Grundmeier, G.; Castro, M.; Linko, V.; Keller, A. Scaling Up DNA Origami Lattice Assembly. *Chem. Eur. J.* **2021,** *27* (33), 8564–8571. DOI: 10.1002/chem.202100784.

230. Sides, P. J.; Faruqui, D.; Gellman, A. J. Dynamics of charging of muscovite mica: measurement and modeling. *Langmuir* **2009,** *25* (3), 1475–1481. DOI: 10.1021/la802752g.

231. Bousse, L.; Mostarshed, S.; van der Shoot, B.; Rooij, N. de; Gimmel, P.; Göpel, W. Zeta potential measurements of Ta2O5 and SiO2 thin films. *J. Colloid Interface Sci.* **1991,** *147* (1), 22–32. DOI: 10.1016/0021-9797(91)90130-Z.

232. Keller, A.; Fritzsche, M.; Ogaki, R.; Bald, I.; Facsko, S.; Dong, M.; Kingshott, P.; Besenbacher, F. Tuning the hydrophobicity of mica surfaces by hyperthermal Ar ion irradiation. *J. Chem. Phys.* **2011,** *134* (10), 104705. DOI: 10.1063/1.3561292.

233. Yang, Y.; Yu, M.; Böke, F.; Qin, Q.; Hübner, R.; Knust, S.; Schwiderek, S.; Grundmeier, G.; Fischer, H.; Keller, A. Effect of nanoscale surface topography on the adsorption of globular proteins. *Appl. Surf. Sci.* **2021,** *535*, 147671. DOI: 10.1016/j.apsusc.2020.147671.

234. Mayer, T. M.; Chason, E.; Howard, A. J. Roughening instability and ion-induced viscous relaxation of SiO2 surfaces. *J. Appl. Phys.* **1994,** *76* (3), 1633–1643. DOI: 10.1063/1.357748.

235. Brunauer, S.; Kantro, D. L.; Weise, C. H. THE SURFACE ENERGIES OF AMORPHOUS SILICA AND HYDROUS AMORPHOUS SILICA. *Can. J. Chem.* **1956,** *34* (10), 1483–1496. DOI: 10.1139/v56-190.

236. Mizele, J.; Dandurand, J. L.; Schott, J. Determination of the surface energy of amorphous silica from solubility measurements in micropores. *Surf. Sci.* **1985,** *162* (1), 830–837. DOI: 10.1016/0039-6028(85)90986-0.

237. Shchipalov, Y. K. Surface Energy of Crystalline and Vitreous Silica. *Glass Ceram.* **2000,** *57* (11), 374–377. DOI: 10.1023/A:1010900903019.

238. Keller, A.; Facsko, S.; Möller, W. Evolution of ion-induced ripple patterns on SiO2 surfaces. *Nucl. Instrum. Methods Phys. Res., Sect. B* **2009,** *267* (4), 656–659. DOI: 10.1016/j.nimb.2008.11.044.

239. Keller, A.; Facsko, S.; Möller, W. The morphology of amorphous SiO(2) surfaces during low energy ion sputtering. *J. Phys. Condens. Matter* **2009,** *21* (49), 495305. DOI: 10.1088/0953-8984/21/49/495305.

240. Teschome, B.; Facsko, S.; Gothelf, K. V.; Keller, A. Alignment of Gold Nanoparticle-Decorated DNA Origami Nanotubes: Substrate Prepatterning versus Molecular Combing. *Langmuir* **2015,** *31* (46), 12823–12829. DOI: 10.1021/acs.langmuir.5b02569.

241. Prinz, J.; Heck, C.; Ellerik, L.; Merk, V.; Bald, I. DNA origami based Au-Ag-core-shell nanoparticle dimers with single-molecule SERS sensitivity. *Nanoscale* **2016,** *8* (10), 5612–5620. DOI: 10.1039/C5NR08674D.

242. Rackwitz, J.; Kopyra, J.; Dąbkowska, I.; Ebel, K.; Ranković, M. L.; Milosavljević, A. R.; Bald, I. Sensitizing DNA Towards Low-Energy Electrons with 2-Fluoroadenine. *Angew. Chem. Int. Ed. Engl.* **2016,** *55* (35), 10248–10252. DOI: 10.1002/anie.201603464.

243. Aryal, B. R.; Westover, T. R.; Ranasinghe, D. R.; Calvopiña, D. G.; Uprety, B.; Harb, J. N.; Davis, R. C.; Woolley, A. T. Four-Point Probe Electrical Measurements on Templated Gold Nanowires Formed on Single DNA Origami Tiles. *Langmuir* **2018,** *34* (49), 15069–15077. DOI: 10.1021/acs.langmuir.8b02225.

244. Uprety, B.; Gates, E. P.; Geng, Y.; Woolley, A. T.; Harb, J. N. Site-specific metallization of multiple metals on a single DNA origami template. *Langmuir* **2014,** *30* (4), 1134–1141. DOI: 10.1021/la403617r (accessed 2020-02-27).

245. Surwade, S. P.; Zhou, F.; Li, Z.; Powell, A.; O'Donnell, C.; Liu, H. Nanoscale Patterning of Self-Assembled Monolayers using DNA Nanostructure Templates. *Chem. Commun.* **2016,** *52* (8), 1677–1680. DOI: 10.1039/c5cc08183a.

246. Surwade, S. P.; Zhao, S.; Liu, H. Molecular Lithography Through DNA-Mediated Etching and Masking of SiO2. *J. Am. Chem. Soc.* **2011,** *133* (31), 11868–11871.

247. Yang, Y.; Knust, S.; Schwiderek, S.; Qin, Q.; Yun, Q.; Grundmeier, G.; Keller, A. Protein Adsorption at Nanorough Titanium Oxide Surfaces: The Importance of Surface Statistical Parameters beyond Surface Roughness. *Nanomaterials* **2021,** *11* (2), 357. DOI: 10.3390/nano11020357.

248. Himpsel, F. J.; McFeely, F. R.; Taleb-Ibrahimi, A.; Yarmoff, J. A.; Hollinger, G. Microscopic structure of the SiO2/Si interface. *Phys. Rev. B* **1988,** *38* (9), 6084–6096. DOI: 10.1103/PhysRevB.38.6084.

249. Moulder, J. F., Chastain, J., Eds. *Handbook of X-ray photoelectron spectroscopy*: *A reference book of standard spectra for identification and interpretation of XPS data*, Update; Perkin-Elmer Corporation, 1992.

250. Takabayashi, S.; Kotani, S.; Flores-Estrada, J.; Spears, E.; Padilla, J. E.; Godwin, L. C.; Graugnard, E.; Kuang, W.; Sills, S.; Hughes, W. L. Boron-Implanted Silicon Substrates for Physical Adsorption of DNA Origami. *Int. J. Mol. Sci.* **2018,** *19* (9), 2513. DOI: 10.3390/ijms19092513.

251. McCafferty, E.; Wightman, J. P. Determination of the concentration of surface hydroxyl groups on metal oxide films by a quantitative XPS method. *Surf. Interface Anal.* **1998,** *26* (8), 549–564. DOI: 10.1002/(SICI)1096-9918(199807)26:8<549:AID-SIA396>3.0.CO;2-Q.

252. Choi, W. K.; Choo, C. K.; Han, K. K.; Chen, J. H.; Loh, F. C.; Tan, K. L. Densification of radio frequency sputtered silicon oxide films by rapid thermal annealing. *J. Appl. Phys.* **1998,** *83* (4), 2308–2314. DOI: 10.1063/1.366974.

253. Seo, T.; Park, H.; Jeon, G.; Yun, J.; Park, S.; Seong, S.; Chung, Y. Low-Temperature Fabrication (≤150 °C) of High-Quality Sputtered Silicon Oxide Thin Film with Hydrogen Plasma Treatment. *ACS Appl. Electron. Mater.* **2020,** *2* (10), 3320–3326. DOI: 10.1021/acsaelm.0c00631.

254. Nečas, D.; Klapetek, P. Gwyddion: an open-source software for SPM data analysis. *Open Phys.* **2012,** *10* (1), 181–188. DOI: 10.2478/s11534-011-0096-2.

255. Gerovac, M.; Chihara, K.; Wicke, L.; Böttcher, B.; Lavigne, R.; Vogel, J. Phage proteins target and co-opt host ribosomes immediately upon infection. *Nat. Microbiol.* **2024,** *9* (3), 787–800. DOI: 10.1038/s41564-024-01616-x.

256. Nechaev, S.; Severinov, K. The elusive object of desire--interactions of bacteriophages and their hosts. *Curr. Opin. Microbiol.* **2008,** *11* (2), 186–193. DOI: 10.1016/j.mib.2008.02.009.

257. Su, Y.; Zhang, W.; Liang, Y.; Wang, H.; Liu, Y.; Zheng, K.; Liu, Z.; Yu, H.; Ren, L.; Shao, H.; Sung, Y. Y.; Mok, W. J.; Wong, L. L.; Zhang, Y.-Z.; McMinn, A.; Wang, M. Identification and genomic analysis

of temperate Halomonas bacteriophage vB_HmeY_H4907 from the surface sediment of the Mariana Trench at a depth of 8,900 m. *Microbiol. Spectr.* **2023,** *11* (5), e0191223. DOI: 10.1128/spectrum.01912-23.

258. Hu, M.; Xing, B.; Yang, M.; Han, R.; Pan, H.; Guo, H.; Liu, Z.; Huang, T.; Du, K.; Jiang, S.; Zhang, Q.; Lu, W.; Huang, X.; Zhou, C.; Li, J.; Song, W.; Deng, Z.; Xiao, M. Characterization of a novel genus of jumbo phages and their application in wastewater treatment. *iScience* **2023,** *26* (6), 106947. DOI: 10.1016/j.isci.2023.106947.

259. Penadés, J. R.; Chen, J.; Quiles-Puchalt, N.; Carpena, N.; Novick, R. P. Bacteriophage-mediated spread of bacterial virulence genes. *Curr. Opin. Microbiol.* **2015,** *23*, 171–178. DOI: 10.1016/j.mib.2014.11.019.

260. Muniesa, M.; Colomer-Lluch, M.; Jofre, J. Potential impact of environmental bacteriophages in spreading antibiotic resistance genes. *Future Microbiol.* **2013,** *8* (6), 739–751. DOI: 10.2217/fmb.13.32.

261. Hatfull, G. F.; Dedrick, R. M.; Schooley, R. T. Phage Therapy for Antibiotic-Resistant Bacterial Infections. *Annu. Rev. Med.* **2022,** *73*, 197–211. DOI: 10.1146/annurev-med-080219-122208.

262. Pires, D. P.; Costa, A. R.; Pinto, G.; Meneses, L.; Azeredo, J. Current challenges and future opportunities of phage therapy. *FEMS Microbiol. Rev.* **2020,** *44* (6), 684–700. DOI: 10.1093/femsre/fuaa017.

263. Leptihn, S.; Loh, B. Complexity, challenges and costs of implementing phage therapy. *Future Microbiol.* **2022,** *17*, 643–646. DOI: 10.2217/fmb-2022-0054.

264. Khan Mirzaei, M.; Nilsson, A. S. Isolation of phages for phage therapy: a comparison of spot tests and efficiency of plating analyses for determination of host range and efficacy. *PLoS One* **2015,** *10* (3), e0118557. DOI: 10.1371/journal.pone.0118557.

265. Parcey, M.; Gayder, S.; Castle, A. J.; Svircev, A. M. Molecular Profile of Phage Infection: A Novel Approach for the Characterization of Erwinia Phages through qPCR. *Int. J. Mol. Sci.* **2020,** *21* (2). DOI: 10.3390/ijms21020553.

266. O'Connell, L.; Mandula, O.; Leroy, L.; Aubert, A.; Marcoux, P. R.; Roupioz, Y. Ultrafast and Multiplexed Bacteriophage Susceptibility Testing by Surface Plasmon Resonance and Phase Imaging of Immobilized Phage Microarrays. *Chemosensors* **2022,** *10* (5), 192. DOI: 10.3390/chemosensors10050192.

267. Obořilová, R.; Šimečková, H.; Pastucha, M.; Klimovič, Š.; Víšová, I.; Přibyl, J.; Vaisocherová-Lísalová, H.; Pantůček, R.; Skládal, P.; Mašlaňová, I.; Farka, Z. Atomic force microscopy and surface

plasmon resonance for real-time single-cell monitoring of bacteriophage-mediated lysis of bacteria. *Nanoscale* **2021,** *13* (31), 13538–13549. DOI: 10.1039/D1NR02921E.

268. Melo, L. D. R.; Monteiro, R.; Pires, D. P.; Azeredo, J. Phage-Host Interaction Analysis by Flow Cytometry Allows for Rapid and Efficient Screening of Phages. *Antibiotics* **2022,** *11* (2). DOI: 10.3390/antibiotics11020164.

269. Egido, J. E.; Toner-Bartelds, C.; Costa, A. R.; Brouns, S. J. J.; Rooijakkers, S. H. M.; Bardoel, B. W.; Haas, P.-J. Monitoring phage-induced lysis of gram-negatives in real time using a fluorescent DNA dye. *Sci. Rep.* **2023,** *13* (1), 856. DOI: 10.1038/s41598-023-27734-w.

270. Pires, D. P.; Meneses, L.; Brandão, A. C.; Azeredo, J. An overview of the current state of phage therapy for the treatment of biofilm-related infections. *Curr. Opin. Virol.* **2022,** *53*, 101209. DOI: 10.1016/j.coviro.2022.101209.

271. Yang, Y.; Schwiderek, S.; Grundmeier, G.; Keller, A. Strain-Dependent Adsorption of Pseudomonas aeruginosa-Derived Adhesin-Like Peptides at Abiotic Surfaces. *Micro* **2021,** *1* (1), 129–139. DOI: 10.3390/micro1010010.

272. Fung, S. L.; Cohen, J. P.; Pashuck, E. T.; Miles, C. E.; Freeman, J. W.; Kohn, J. Rational design of poly(peptide-ester) block copolymers for enzyme-specific surface resorption. *J. Mater. Chem. B* **2023,** *11* (28), 6621–6633. DOI: 10.1039/D3TB00265A.

273. Zhang, S.; Bai, H.; Pi, J.; Yang, P.; Cai, J. Label-free quartz crystal microbalance with dissipation monitoring of resveratrol effect on mechanical changes and folate receptor expression levels of living MCF-7 cells: a model for screening of drugs. *Anal. Chem.* **2015,** *87* (9), 4797–4805. DOI: 10.1021/acs.analchem.5b00083.

274. Lin, W.; Reddavide, F. V.; Uzunova, V.; Gür, F. N.; Zhang, Y. Characterization of DNA-conjugated compounds using a regenerable chip. *Anal. Chem.* **2015,** *87* (2), 864–868. DOI: 10.1021/ac503960z.

275. Deligöz, H.; Tieke, B. QCM-D study of layer-by-layer assembly of polyelectrolyte blend films and their drug loading-release behavior. *Colloids Surf., A* **2014,** *441*, 725–736. DOI: 10.1016/j.colsurfa.2013.10.033.

276. Karlsson, J.; Atefyekta, S.; Andersson, M. Controlling drug delivery kinetics from mesoporous titania thin films by pore size and surface energy. *Int. J. Nanomedicine* **2015,** *10*, 4425–4436. DOI: 10.2147/IJN.S83005.

277. Hajiraissi, R.; Hanke, M.; Gonzalez Orive, A.; Duderija, B.; Hofmann, U.; Zhang, Y.; Grundmeier, G.; Keller, A. Effect of Terminal Modifications on the Adsorption and Assembly of hIAPP(20-29). *ACS Omega* **2019,** *4* (2), 2649–2660. DOI: 10.1021/acsomega.8b03028.

278. Hajiraissi, R.; Hanke, M.; Yang, Y.; Duderija, B.; Gonzalez Orive, A.; Grundmeier, G.; Keller, A. Adsorption and Fibrillization of Islet Amyloid Polypeptide at Self-Assembled Monolayers Studied by QCM-D, AFM, and PM-IRRAS. *Langmuir* **2018,** *34* (11), 3517–3524. DOI: 10.1021/acs.langmuir.7b03626.

279. Alexander, T. E.; Lozeau, L. D.; Camesano, T. A. QCM-D characterization of time-dependence of bacterial adhesion. *Cell Surf.* **2019,** *5*, 100024. DOI: 10.1016/j.tcsw.2019.100024.

280. Wang, Y.; Narain, R.; Liu, Y. Study of bacterial adhesion on different glycopolymer surfaces by quartz crystal microbalance with dissipation. *Langmuir* **2014,** *30* (25), 7377–7387. DOI: 10.1021/la5016115.

281. Olsson, A. L. J.; Mitzel, M. R.; Tufenkji, N. QCM-D for non-destructive real-time assessment of Pseudomonas aeruginosa biofilm attachment to the substratum during biofilm growth. *Colloids Surf. B* **2015,** *136*, 928–934. DOI: 10.1016/j.colsurfb.2015.10.032.

282. García-Bonillo, C.; Texidó, R.; Reyes-Carmenaty, G.; Gilabert-Porres, J.; Borrós, S. Study of the Human Albumin Role in the Formation of a Bacterial Biofilm on Urinary Devices Using QCM-D. *ACS Appl. Bio Mater.* **2020,** *3* (5), 3354–3364. DOI: 10.1021/acsabm.0c00286.

283. Yue, H.; Li, Y.; Yang, M.; Mao, C. T7 Phage as an Emerging Nanobiomaterial with Genetically Tunable Target Specificity. *Adv. Sci.* **2022,** *9* (4), e2103645. DOI: 10.1002/advs.202103645.

284. Reshes, G.; Vanounou, S.; Fishov, I.; Feingold, M. Cell shape dynamics in Escherichia coli. *Biophys. J.* **2008,** *94* (1), 251–264. DOI: 10.1529/biophysj.107.104398.

285. Olsson, A. L. J.; van der Mei, H. C.; Busscher, H. J.; Sharma, P. K. Acoustic sensing of the bacterium-substratum interface using QCM-D and the influence of extracellular polymeric substances. *J. Colloid Interface Sci.* **2011,** *357* (1), 135–138. DOI: 10.1016/j.jcis.2011.01.035.

286. Olsson, A. L. J.; van der Mei, H. C.; Johannsmann, D.; Busscher, H. J.; Sharma, P. K. Probing Colloid–Substratum Contact Stiffness by Acoustic Sensing in a Liquid Phase. *Anal. Chem.* **2012,** *84* (10), 4504–4512. DOI: 10.1021/ac300366s.

287. Olsson, A. L. J.; van der Mei, H. C.; Busscher, H. J.; Sharma, P. K. Influence of cell surface appendages on the bacterium-substratum interface measured real-time using QCM-D. *Langmuir* **2009,** *25* (3), 1627–1632. DOI: 10.1021/la803301q.

288. Poitras, C.; Tufenkji, N. A QCM-D-based biosensor for E. coli O157:H7 highlighting the relevance of the dissipation slope as a transduction signal. *Biosens. Bioelectron.* **2009,** *24* (7), 2137–2142. DOI: 10.1016/j.bios.2008.11.016.

289. Olsson, A. L. J.; van der Mei, H. C.; Busscher, H. J.; Sharma, P. K. Novel analysis of bacterium-substratum bond maturation measured using a quartz crystal microbalance. *Langmuir* **2010,** *26* (13), 11113–11117. DOI: 10.1021/la100896a.

290. Karasz, D. C.; Weaver, A. I.; Buckley, D. H.; Wilhelm, R. C. Conditional filamentation as an adaptive trait of bacteria and its ecological significance in soils. *Environ. Microbiol.* **2022,** *24* (1), 1–17. DOI: 10.1111/1462-2920.15871.

291. Cushnie, T. P. T.; O'Driscoll, N. H.; Lamb, A. J. Morphological and ultrastructural changes in bacterial cells as an indicator of antibacterial mechanism of action. *Cell. Mol. Life Sci.* **2016,** *73* (23), 4471–4492. DOI: 10.1007/s00018-016-2302-2.

292. Wehrens, M.; Ershov, D.; Rozendaal, R.; Walker, N.; Schultz, D.; Kishony, R.; Levin, P. A.; Tans, S. J. Size Laws and Division Ring Dynamics in Filamentous Escherichia coli cells. *Curr. Biol.* **2018,** *28* (6), 972-979.e5. DOI: 10.1016/j.cub.2018.02.006.

293. Klein, K.; Palarasah, Y.; Kolmos, H. J.; Møller-Jensen, J.; Andersen, T. E. Quantification of filamentation by uropathogenic Escherichia coli during experimental bladder cell infection by using semi-automated image analysis. *J. Microbiol. Methods* **2015,** *109*, 110–116. DOI: 10.1016/j.mimet.2014.12.017.

294. Meijer, W. J.; Horcajadas, J. A.; Salas, M. Phi29 family of phages. *Microbiol. Mol. Biol. Rev.* **2001,** *65* (2), 261-87. DOI: 10.1128/mmbr.65.2.261-287.2001.

295. Levy, I. K.; Salustro, D.; Battaglini, F.; Lizarraga, L.; Murgida, D. H.; Agusti, R.; D'Accorso, N.; Raventos Segura, D.; González Palmén, L.; Negri, R. M. Quantification of Enzymatic Biofilm Removal Using the Sauerbrey Equation: Application to the Case of Pseudomonas protegens. *ACS Omega* **2024,** *9* (9), 10445–10458. DOI: 10.1021/acsomega.3c08475.

296. Kaga, H.; Nakamura, A.; Orita, M.; Endo, K.; Akamatsu, M.; Sakai, K.; Sakai, H. Removal of a Model Biofilm by Sophorolipid Solutions: A QCM-D Study. *J. Oleo Sci.* **2022,** *71* (5), 663–670. DOI: 10.5650/jos.ess21360.

297. Hausmann, R.; Messerschmid, M. Inhibition of gene expression of T7-related phages by prophage P1. *Mol. Gen. Genet.* **1988,** *212* (3), 543–547. DOI: 10.1007/bf00330862.

298. Nečas, D.; Klapetek, P. Gwyddion: An open-source software for SPM data analysis. *Open Phys.* **2012,** *10* (1), 99. DOI: 10.2478/s11534-011-0096-2.

299. Patterson, E. I.; Prince, T.; Anderson, E. R.; Casas-Sanchez, A.; Smith, S. L.; Cansado-Utrilla, C.; Solomon, T.; Griffiths, M. J.; Acosta-Serrano, Á.; Turtle, L.; Hughes, G. L. Methods of Inactivation of SARS-CoV-2 for Downstream Biological Assays. *J. Infect. Dis.* **2020,** *222* (9), 1462–1467. DOI: 10.1093/infdis/jiaa507.

300. Nims, R. W.; Plavsic, M. Polyomavirus inactivation - a review. *Biologicals* **2013,** *41* (2), 63–70. DOI: 10.1016/j.biologicals.2012.09.011.

301. Pilchová, V.; Prajeeth, C. K.; Jendrny, P.; Twele, F.; Meller, S.; Pink, I.; Fathi, A.; Addo, M. M.; Volk, H. A.; Osterhaus, A.; Köckritz-Blickwede, M. von; Schulz, C. β-Propiolactone (BPL)-inactivation of SARS-Co-V-2: In vitro validation with focus on saliva from COVID-19 patients for scent dog training. *J. Virol. Methods* **2023,** *317*, 114733. DOI: 10.1016/j.jviromet.2023.114733.

302. Wilton, T.; Dunn, G.; Eastwood, D.; Minor, P. D.; Martin, J. Effect of formaldehyde inactivation on poliovirus. *J. Virol.* **2014,** *88* (20), 11955–11964. DOI: 10.1128/JVI.01809-14.

303. Dembinski, J. L.; Hungnes, O.; Hauge, A. G.; Kristoffersen, A.-C.; Haneberg, B.; Mjaaland, S. Hydrogen peroxide inactivation of influenza virus preserves antigenic structure and immunogenicity. *J. Virol. Methods* **2014,** *207*, 232–237. DOI: 10.1016/j.jviromet.2014.07.003.

304. Finkensieper, J.; Issmail, L.; Fertey, J.; Rockstroh, A.; Schopf, S.; Standfest, B.; Thoma, M.; Grunwald, T.; Ulbert, S. Low-Energy Electron Irradiation of Tick-Borne Encephalitis Virus Provides a Protective Inactivated Vaccine. *Front. Immunol.* **2022,** *13*, 825702. DOI: 10.3389/fimmu.2022.825702.

305. Uittenbogaard, J. P.; Zomer, B.; Hoogerhout, P.; Metz, B. Reactions of beta-propiolactone with nucleobase analogues, nucleosides, and peptides: implications for the inactivation of viruses. *J. Biol. Chem.* **2011,** *286* (42), 36198–36214. DOI: 10.1074/jbc.m111.279232.

306. Perrin, P.; Morgeaux, S. Inactivation of DNA by beta-propiolactone. *Biologicals* **1995,** *23* (3), 207–211. DOI: 10.1006/biol.1995.0034.

307. Amanna, I. J.; Raué, H.-P.; Slifka, M. K. Development of a new hydrogen peroxide–based vaccine platform. *Nat. Med.* **2012,** *18* (6), 974–979. DOI: 10.1038/nm.2763.

308. Sadraeian, M.; Le Zhang; Aavani, F.; Biazar, E.; Jin, D. Viral inactivation by light. *Elight* **2022,** *2* (1). DOI: 10.1186/s43593-022-00029-9.

309. Fertey, J.; Thoma, M.; Beckmann, J.; Bayer, L.; Finkensieper, J.; Reißhauer, S.; Berneck, B. S.; Issmail, L.; Schönfelder, J.; Casado, J. P.; Poremba, A.; Rögner, F.-H.; Standfest, B.; Makert, G. R.; Walcher, L.; Kistenmacher, A.-K.; Fricke, S.; Grunwald, T.; Ulbert, S. Automated application of low energy electron irradiation enables inactivation of pathogen- and cell-containing liquids in

biomedical research and production facilities. *Sci. Rep.* **2020,** *10* (1), 12786. DOI: 10.1038/s41598-020-69347-7.

310. Shahi, S.; Khorvash, R.; Goli, M.; Ranjbaran, S. M.; Najarian, A.; Mohammadi Nafchi, A. Review of proposed different irradiation methods to inactivate food-processing viruses and microorganisms. *Food Sci. Nutr.* **2021,** *9* (10), 5883–5896. DOI: 10.1002/fsn3.2539.

311. Taubman, M. A.; Atassi, M. Z. Reaction of beta-propiolactone with amino acids and its specificity for methionine. *Biochem. J.* **1968,** *106* (4), 829–834. DOI: 10.1042/bj1060829.

312. Zheng, J.; Yue, R.; Yang, R.; Wu, Q.; Wu, Y.; Huang, M.; Chen, X.; Lin, W.; Huang, J.; Chen, X.; Jiang, Y.; Yang, B.; Liao, Y. Visualization of Zika Virus Infection via a Light-Initiated Bio-Orthogonal Cycloaddition Labeling Strategy. *Front. Bioeng. Biotechnol* **2022,** *10*, 940511. DOI: 10.3389/fbioe.2022.940511.

313. Xu, X.; Song, H.; Qi, J.; Liu, Y.; Wang, H.; Su, C.; Shi, Y.; Gao, G. F. Contribution of intertwined loop to membrane association revealed by Zika virus full-length NS1 structure. *The EMBO journal* **2016,** *35* (20), 2170–2178. DOI: 10.15252/embj.201695290.

314. Brown, W. C.; Akey, D. L.; Konwerski, J. R.; Tarrasch, J. T.; Skiniotis, G.; Kuhn, R. J.; Smith, J. L. Extended surface for membrane association in Zika virus NS1 structure. *Nat. Struct. Mol. Biol.* **2016,** *23* (9), 865–867. DOI: 10.1038/nsmb.3268.